

**NUMERICAL MODELLING OF THE ELECTRIC VEHICLE CABIN
COOLING**

FABIAN JONG CHIN PENG

**A project report submitted in partial fulfilment of the
requirements for the award of Bachelor of Engineering
(Honours.) Mechanical Engineering**

**Lee Kong Chian Faculty of Engineering and Science
Universiti Tunku Abdul Rahman**

April 2019

DECLARATION

I hereby declare that this project report is based on my original work except for citations and quotations, which have been duly acknowledged. I also declare that it has not been previously and concurrently submitted for any other degree or award at UTAR or other institutions.

Signature : _____

Name : Fabian Jong Chin Peng

ID No. : 15UEB02719

Date : 6th May 2019

APPROVAL FOR SUBMISSION

I certify that this project report entitled “**NUMERICAL MODELLING OF THE ELECTRIC VEHICLE CABIN COOLING**” was prepared by **FABIAN JONG CHIN PENG** has met the required standard for submission in partial fulfilment of the requirements for the award of Bachelor of Engineering (Honours.) Mechanical Engineering at Universiti Tunku Abdul Rahman.

Approved by,

Signature : _____

Supervisor : Dr. Bernard Saw Lip Huat

Date : 6th May 2019

The copyright of this report belongs to the author under the terms of the copyright Act 1987 as qualified by Intellectual Property Policy of Universiti Tunku Abdul Rahman. Due acknowledgement shall always be made of the use of any material contained in, or derived from, this report.

© 2019, Fabian Jong Chin Peng. All right reserved.

ACKNOWLEDGEMENTS

First and foremost, I would like to extend my appreciation to my academic mentor and project supervisor, Dr. Bernard Saw Lip Huat for his continuous support throughout my entire duration of study, who has been a source of continuous technical and academic knowledge.

I would also like to express my deepest appreciation to my family members, as without them, I would not be granted the opportunity to be here studying today. They have been my bedrock for inspiration, drive, as well as moral support for my entire life, and someone who I can turn to in times of difficulties.

To my closest confidant, Tan Jaw Tzuu and Adrian Lim Jern Ee, who are always here during times of solitude, and made this journey an easier path to travel, with all the late night adventures and “mamak” sessions.

Lastly, I thank all those who have participated directly and indirectly towards this project. All their efforts and advices are deeply appreciated and hereby recognised.

ABSTRACT

The study of the cabin cooling system in an Electric Vehicle is vital to understand its energy consumption behaviour, where such information can be acted upon to better optimise and improve the overall energy consumption of the vehicle, thus translating into a longer driving range.

Factors that contribute to the total thermal load in a cabin space are modelled, where in Edinburgh has a value of 1880.14 W and 3136.14 W for Kuala Lumpur. Expansion is performed in the construction of the solar thermal load model, which has the capability of calculating solar irradiance based on various inputs, which after validation produces a relative error of 7.17 %. The thermal load model is integrated into a refrigeration model at the cabin space subsystem in order to allow the study of the effects of thermal loads on the performance of the refrigeration circuit using a single model. The model is validated for accuracy and it is found to have an average relative error of 15.11 %.

The thermal load model is also incorporated into a cabin temperature-predicting algorithm expansion. The refrigeration circuit model is also expanded to study the effects of battery heat generated from different driving cycles on the performance of the refrigeration circuit, which requires maximum instantaneous power consumption of 140 W, 130 W and 138 W for UDDS, HWFET and US06 driving cycles. The model is also able to maintain the cabin temperature close to the targeted temperature, where the maximum deviation between the cabin temperatures to the targeted is only 1.09 %. Lastly, a study on the effects of the supporting infrastructure is done, where it is concluded that the most optimal configuration is the one with triple glazing windows and extractor fans that is capable of reducing the combined thermal load and cabin temperature after 3600 seconds by 24.1 % and 20.5 % in Edinburgh and 42.68 % and 23.55 % in Kuala Lumpur.

TABLE OF CONTENTS

DECLARATION	ii
APPROVAL FOR SUBMISSION	iii
ACKNOWLEDGEMENTS	v
ABSTRACT	vi
TABLE OF CONTENTS	vii
LIST OF TABLES	xi
LIST OF FIGURES	xii
LIST OF SYMBOLS / ABBREVIATIONS	xvii
LIST OF APPENDICES	xxi

CHAPTER

INTRODUCTION	1
1.1 General Introduction	1
1.2 Importance of the Study	5
1.3 Problem Statement	6
1.4 Aims and Objectives	6
1.5 Scope and Limitation of the Study	7
1.6 Contribution of The Study	8
1.7 Outline of The Report	8
LITERATURE REVIEW	10
2.1 Introduction	10
2.2 Literature Review	10
2.2.1 Cooling System in Vehicle	10
2.2.2 Thermal Load Calculation	13
2.2.3 Occupant's Thermal Comfort	18
2.2.4 Energy Consumption	21
2.3 Summary	24

METHODOLOGY AND WORK PLAN	26
3.1 Introduction	26
3.2 Governing Theories and Formula	28
3.2.1 Thermal Load Calculation	28
3.2.2 Thermal Comfort Indication	39
3.2.3 Cabin Temperature Predicting Calculation	39
3.2.4 Cooling Capacity of Supporting Infrastructure	39
3.3 Simulation	40
3.3.1 Phase 1: Thermal Load Modelling	42
3.3.2 Phase 2: Construction of EV Refrigeration Model	49
3.3.3 Phase 3: Integration between Thermal Load and Refrigeration Model	55
3.3.4 Phase 4: Construction of Experimental Model	56
3.4 Validation with Experimental Result	58
3.5 Expansion on Simulation Model	59
3.5.1 Expansion on Refrigeration Circuit Model	59
3.5.2 Expansion on Thermal Load Model	59
3.5.3 Supporting Infrastructure for Cabin Cooling	60
3.6 Summary	61
RESULTS AND DISCUSSION	63
4.1 Introduction	63
4.2 Thermal Load Modelling	63
4.2.1 Metabolic Thermal Load	63
4.2.2 Ambient Thermal Load	64
4.2.3 Ventilation Thermal Load	65
4.2.4 Battery Thermal Load	67
4.2.5 Solar Thermal Load for Edinburgh, Scotland	67
4.2.6 Solar Thermal Load for Kuala Lumpur, Malaysia	69
4.2.7 Combined Thermal Load	71
4.3 Refrigeration Model Response	72
4.3.1 Human Metabolic Thermal Load	73
4.3.2 Ambient Thermal Load	77

4.3.3	Ventilation Thermal Load	80
4.3.4	Battery Thermal Load	84
4.3.5	Solar Thermal Load	88
4.4	Comparison of Simulated and Actual Refrigeration Circuit Response	93
4.5	Expansion Work on Different Driving Cycles	99
4.5.1	Response of Refrigeration Circuit on UDDS Driving Cycle	99
4.5.2	Response of Refrigeration Circuit on HWFET Driving Cycle	103
4.5.3	Response of Refrigeration Circuit on US06 Driving Cycle	107
4.6	Expansion Work on Cabin Temperature-Predicting Algorithm	111
4.6.1	Cabin Temperature Predicting in Edinburgh, Scotland	111
4.6.2	Cabin Temperature Predicting in Kuala Lumpur, Malaysia	112
4.7	Supporting Infrastructure on Cabin Cooling	113
4.7.1	Passive Supporting Infrastructure on Cabin Cooling	114
4.7.2	Active Supporting Infrastructure on Cabin Cooling	117
4.7.3	Combination of Passive and Active Supporting Infrastructure	119
4.8	Summary	120

CONCLUSIONS AND RECOMMENDATIONS **122**

5.1	Conclusions	122
5.1.1	Thermal Load Modelling	122
5.1.2	Refrigeration Circuit Modelling	123
5.1.3	Validation Experiment	124
5.1.4	Expansion Work on Different Driving Cycles	125

5.1.5	Cabin Temperature-Predicting Model	125
5.1.6	Supporting Infrastructure on Cabin Cooling	125
5.2	Recommendations	127
REFERENCES		128
APPENDICES		132

LIST OF TABLES

Table 3.1:	Area (in m ²) and Thickness (in mm) of Window Surface for Renault Zoe EV (Doyle, 2017)	29
Table 3.2:	ASP (in °) and TLT (in °) of Window Surfaces for Renault Zoe EV (Doyle, 2017)	31
Table 3.3:	Reflectivity Coefficient of Surface Types (Thevenard & Haddad, 2006)	32
Table 3.4:	Conditions and Relevant Values of $2b\pi^3 + 2b-1$ (Muneer et.al., 2000)	33
Table 3.5:	Thermal Conductivity (in W/m ² K) of Vehicle Materials (Muneer et al., 2000; Khayyam et al., 2011)	35
Table 3.6:	Indoor Cabin Dimensions (in m ²) and Their <i>SU</i> Values in (W/K) (Doyle, 2017)	35
Table 3.7:	Parameters for Refrigeration Circuit of Air Conditioning Unit in an EV	50
Table 3.8:	Parameters for Condenser Pipe	52
Table 3.9:	Parameters Adjustment for G.U.N.T Hamburg ET400 Refrigeration Circuit	57
Table 4.1:	Metabolic Thermal Load of Occupants (in W)	63
Table 4.2:	Input to Solar Thermal Load Model for Edinburgh, Scotland	67
Table 4.3:	Input to Solar Thermal Load Model for Kuala Lumpur, Malaysia	70
Table 4.4:	Combined Thermal Load Model for Edinburgh, Scotland	72
Table 4.5:	Combined Thermal Load Model for Kuala Lumpur, Malaysia	72

LIST OF FIGURES

Figure 1.1:	Total US Greenhouse Gas Emission by Economic Sector 2016 (EPA, 2018)	2
Figure 1.2:	Years of Fossil Fuel Left (BP, 2016)	3
Figure 3.1:	Research Flow Chart	26
Figure 3.2:	Expansion of Model Implementation	27
Figure 3.3:	Driver Metabolic Thermal Load Model	42
Figure 3.4:	Passenger Metabolic Thermal Load Model	43
Figure 3.5:	Variation of Passenger with Time	43
Figure 3.6:	Ambient Thermal Load Model	44
Figure 3.7:	Ventilation Thermal Load Model	45
Figure 3.8:	Base Level of Solar Thermal Load Model	45
Figure 3.9:	Level Two of Solar Thermal Load Model	46
Figure 3.10:	Level Three of Solar Thermal Load Model	47
Figure 3.11:	Solar Geometry Subsystem as Expanded from Level Three	47
Figure 3.12:	Slope Irradiance Subsystem	48
Figure 3.13:	Two Phase Fluid Refrigeration Model	49
Figure 3.14:	Compressor Subsystem	51
Figure 3.15:	Condenser Subsystem	52
Figure 3.16:	Environment Subsystem	53
Figure 3.17:	Expansion Valve Subsystem	53
Figure 3.18:	Valve Control Subsystem	54
Figure 3.19:	Evaporator Subsystem	55
Figure 3.20:	Cabin Space Subsystem	55

Figure 3.21:	Thermal Load Input to Experimental Model	57
Figure 3.22:	G.U.N.T Hamburg ET 400 Refrigeration Circuit	58
Figure 3.23:	Cabin Temperature Predicting Algorithm Model	60
Figure 3.24:	Extractor Fan Cooling Model	61
Figure 3.25:	Modified Cabin Temperature Predicting Model	61
Figure 4.1:	Metabolic Thermal Load	64
Figure 4.2:	Ambient Thermal Load	65
Figure 4.3:	Ventilation Thermal Load	66
Figure 4.4:	Solar Thermal Load in Time Domain in Edinburgh, Scotland	68
Figure 4.5:	Solar Thermal Load in Time Domain in Edinburgh, Scotland	70
Figure 4.6:	Metabolic Load Compressor Pressures	73
Figure 4.7:	Metabolic Load Compressor Pressure Ratio	74
Figure 4.8:	Compartment Load Heat Extracted	74
Figure 4.9:	Metabolic Load Compressor Power	75
Figure 4.10:	Cabin Temperature Profile for Metabolic Thermal Load	76
Figure 4.11:	Ambient Load Compressor Pressures	77
Figure 4.12:	Ambient Load Compressor Pressure Ratio	78
Figure 4.13:	Ambient Load Compressor Pressure Ratio	78
Figure 4.14:	Ambient Load Compressor Power	78
Figure 4.15:	Cabin Temperature Profile for Ambient Thermal Load	80
Figure 4.16:	Ventilation Load Compressor Pressures	81
Figure 4.17:	Ventilation Load Compressor Pressure Ratio	81
Figure 4.18:	Ventilation Load Heat Extracted	82

Figure 4.19: Ventilation Load Compressor Power	82
Figure 4.20: Cabin Temperature Profile for Ventilation Thermal Load	83
Figure 4.21: Battery Load Compressor Pressures	85
Figure 4.22: Battery Load Compressor Pressure Ratio	85
Figure 4.23: Battery Load Heat Extracted	85
Figure 4.24: Battery Compressor Power	86
Figure 4.25: Cabin Temperature Profile for Battery Thermal Load	87
Figure 4.26: Solar Load Compressor Pressures, Edinburgh	88
Figure 4.27: Solar Load Compressor Pressure Ratio, Edinburgh	89
Figure 4.28: Solar Load Heat Extracted, Edinburgh	89
Figure 4.29: Solar Load Compressor Power, Edinburgh	89
Figure 4.30: Solar Load Compressor Pressures, Kuala Lumpur	90
Figure 4.31: Solar Load Compressor Pressure Ratio, Kuala Lumpur	90
Figure 4.32: Solar Load Heat Extracted, Kuala Lumpur	90
Figure 4.33: Solar Load Compressor Power, Kuala Lumpur	91
Figure 4.34: Cabin Temperature Profile for Solar Thermal Load in Edinburgh	92
Figure 4.35: Cabin Temperature Profile for Solar Thermal Load in Kuala Lumpur	93
Figure 4.36: Simulated and Experimental Compressor Inlet Temperatures	94
Figure 4.37: Simulated and Experimental Compressor Outlet Temperatures	95
Figure 4.38: Simulated and Experimental Compressor Inlet Pressures	96
Figure 4.39: Simulated and Experimental Compressor Outlet Pressures	97

Figure 4.40:	Simulated and Experimental Compressor Powers	98
Figure 4.41:	UDDS Heat Generation Profile	99
Figure 4.42:	Compressor Cycle for UDDS Driving Cycle	100
Figure 4.43:	Compressor Pressure Ratio for UDDS Driving Cycle	100
Figure 4.44:	Heat Extracted for UDDS Driving Cycle	101
Figure 4.45:	Compressor Power for UDDS Driving Cycle	101
Figure 4.46:	Battery Compartment Temperature Profile for UDDS Driving Cycle	102
Figure 4.47:	HWFET Heat Generation Profile	103
Figure 4.48:	Compressor Cycle for HWFET Driving Cycle	104
Figure 4.49:	Compressor Pressure Ratio for HWFET Driving Cycle	104
Figure 4.50:	Heat Extracted for HWFET Driving Cycle	105
Figure 4.51:	Compressor Power for HWFET Driving Cycle	105
Figure 4.52:	Battery Compartment Temperature Profile for HWFET Driving Cycle	106
Figure 4.53:	US06 Heat Generation Profile	107
Figure 4.54:	Compressor Pressures for US06 Driving Cycle	108
Figure 4.55:	Compressor Pressure Ratio for US06 Driving Cycle	108
Figure 4.56:	Heat Extracted for US06 Driving Cycle	109
Figure 4.57:	Compressor Power for US06 Driving Cycle	109
Figure 4.58:	Battery Compartment Temperature Profile for US06 Driving Cycle	110
Figure 4.59:	Predicted Cabin Temperature in Edinburgh, Scotland	112
Figure 4.60:	Predicted Cabin Temperature in Kuala Lumpur, Malaysia	113

Figure 4.61: Comparison of Solar Thermal Load for Single and Triple Glazing Windows in Edinburgh	115
Figure 4.62: Comparison of Solar Thermal Load for Single and Triple Glazing Windows in Kuala Lumpur	116
Figure 4.63: Comparison of Cabin Temperature of Single Glazed and Triple Glazed Windows in Edinburgh	116
Figure 4.64: Comparison of Cabin Temperature of Single Glazed and Triple Glazed Windows in KL	117
Figure 4.65: Cabin Temperature With and Without Extractor Fan, Edinburgh	118
Figure 4.66: Cabin Temperature With and Without Extractor Fan, Kuala Lumpur	119
Figure 4.67: Cabin Temperatures for Combination of Infrastructures, Edinburgh	119
Figure 4.68: Cabin Temperatures for Combination of Infrastructures, Kuala Lumpur	120

LIST OF SYMBOLS / ABBREVIATIONS

A	area, m ²
A_{DU}	DuBois area, m ²
ASP	aspect of the vehicle
COP_R	coefficient of performance of refrigerator
DEC	angle between sun-earth vector and equatorial plane
c_a	specific heat of cabin air, J/K
d	day
e_i	cabin air enthalpy, J
e_o	exterior air enthalpy, J
H	height, m
h	hour
$h_i,$	cabin convection coefficient, W/m ² K
$h_o,$	outdoor convection coefficient, W/m ² K
\dot{I}_{Dif}	diffuse radiation heat gain per unit area, J/m ²
\dot{I}_{Dir}	direct radiation heat gain per unit area, J/m ²
\dot{I}_{Ref}	reflected radiation heat gain per unit area, J/m ²
$I_{B,TLT}$	beam slope irradiance
$I_{D,TLT}$	directed slope irradiance
I_G	global horizontal irradiation
I_{ERAD}	extra-terrestrial irradiation
$I_{G,TLT}$	reflected slope irradiance
k	thermal conductivity, W/mK
k_t	clearness index
LAT	latitude coordinate
M	human metabolic heat rate, W/m ²
m	month
min	minute
m_a	mass of cabin air, kg
\dot{m}_{Ven}	fresh air mass flow rate, kg/s
\dot{m}_{ext}	extractor fans air mass flow rate, kg/s

P	air pressure, kPa
$P_s,$	water saturation pressure at temperature T , kPa
Q	heat gain, J
\dot{Q}_{Amb}	ambient load, W
\dot{Q}_{AC}	air conditioning cycle load, W
\dot{Q}_{Batt}	battery load, W
\dot{Q}_{Dif}	diffuse radiation load, W
\dot{Q}_{Dir}	direct radiation load, W
\dot{Q}_{Eng}	engine load, W
\dot{Q}_{Exh}	exhaust load, W
\dot{Q}_{Ext}	cooling capacity of extractor fans, W
\dot{Q}_{Met}	metabolic load, W
\dot{Q}_{Ref}	reflected radiation load, W
\dot{Q}_{TOT}	overall thermal load, W
\dot{Q}_{Vent}	ventilation load, W
q_L	heat absorbed from refrigerated space, J
R	mass flow rate ratio
S	surface area of interest, m ²
sec	seconds
SHA	solar hour angle
$SOLALT$	solar altitude
$SOLAZM$	solar azimuth
T	temperature, °C
TLT	tile angle of window
t_c	pull down constant
t_c	pull down time, s
$T_{Comf},$	thermal comfort temperature, K
$T_i,$	indoor temperature, K

T_o ,	outdoor temperature, K
T_s ,	surface temperature, K
U	overall heat transfer coefficient, W/m ² K
W	weight, kg
$w_{net,in}$	net input work, J
X	humidity ratio
y	<i>year</i>
ΔT	change in temperature, °C
τ	surface transmissivity
τ_B	beam transmittance
τ_D	diffused transmittance
τ_G	ground reflected transmittance
τ_n	ground reflected transmittance
θ	angle between surface normal and position of the sun, °
β	altitude angle, °
Σ	tilt angle between the surface and the horizontal surface, °
ρ_g	coefficient of ground reflectivity
λ	surface thickness, m
ω	compressible flow parameter
ϕ	relative humidity, %
ASHRAE	American Society of Heating, Refrigeration, and Air Conditioning Engineer
CAD	Computer Aided Design
CFD	Computational Fluid Dynamics
CLTD	Cooling Load Temperature Differential
COP	Coefficient of Performance
DTM	Deep Thermal Masses
DTS	Dynamic Thermal Sensation
EMS	Energy Management System
EPA	United States Environmental Protection Agency
EV	Electric Vehicle

GATCI	General Absolute Thermal Comfort Index
GTCI	Global Thermal Comfort Index
HBM	Heat Balance Method
ICE	Internal Combustion Engine
ICEV	Internal Combustion Engine Vehicles
MCE	Magnetocaloric Effect
OEM	Original Equipment Manufacturer
OS	Overall Thermal Sensation Index
PCM	Phase Change Material
PMV	Predicted Mean Votes
PPD	Percentage of People's Dissatisfaction
SOC	State of Charge
WFM	Weighting Factor Method

LIST OF APPENDICES

Appendix 1: Expansion of Ventilation Thermal Load Model Subsystems	132
---	-----

CHAPTER 1

INTRODUCTION

1.1 General Introduction

Vehicle is an integral part of the human life when it comes to transportation and it has been so since the mass production of Ford Model T in 1908, which made automobile transportation affordable to the masses (History.com, 2010). According to the Malaysia's Ministry of Transport, the released statistic shows that at the end of 2014, there were approximately 25.1 million vehicles registered in Malaysia. This statistic further emphasizes the strong presence and importance of automobile transportation in the lives of every Malaysian.

Conventionally, automotive vehicle has relied heavily on the capitalisation of energy stored in fossil fuel as its source of propulsion, through the internal combustion engine technology. This type of technology has been proven through time to be effective, robust and more importantly reliable. On the downside, the technology has heavily contributed to various detrimental environmental impacts, such as emission of greenhouse gases, noise pollution (during the operation of ICE (Internal Combustion Engine)) and oil spills (due to accidents during mining of crude oil). According to the United States Environmental Protection Agency (EPA), the transportation sector made up an approximate 28 % of the total greenhouse gas emission in 2016 as illustrated in Figure 1.1 that segments the total greenhouse emission by economic activity. Causation of such emission is traced to vehicles and 90 % of such emission is due to the combustion of petroleum products such as petrol and diesel fuel (EPA, April 2018).

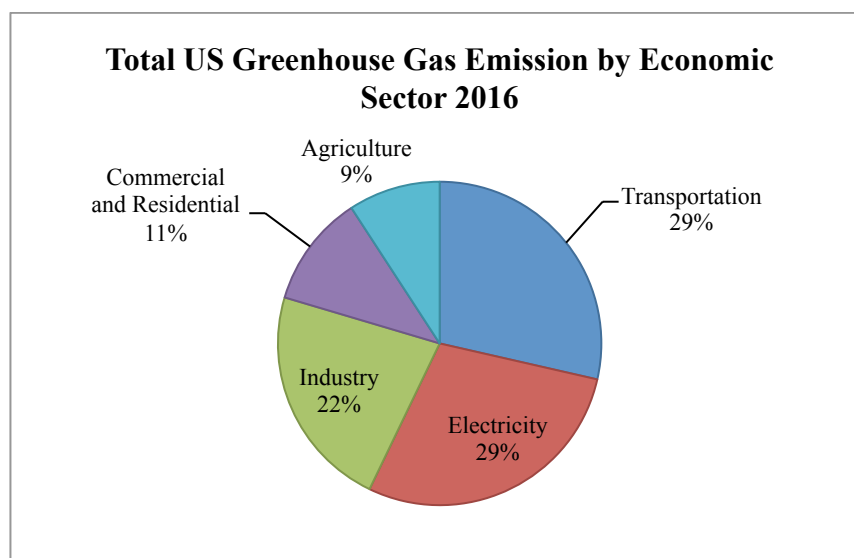


Figure 1.1: Total US Greenhouse Gas Emission by Economic Sector 2016 (EPA, 2018)

The environmental impacts that spurred from the use of ICE vehicles (ICEV) have caused challenges and predicament to producers, regulatory bodies as well as governments. In recent decades, the public sentiment has been swayed towards environmental protection and conservation, where the public now cares more about the wellbeing of environment that half a century ago. In a research conducted by Pew Research Centre conducted in March 2016, it shows that around 74 % of the US adult opined that the government should commit itself in means necessary to protect the environment and the rest felt the nation had overcommitted itself in environmental protection. This survey shows positive public sentiment in environmental protection.

Additionally, it is estimated that the world reserve of oil will be completely depleted in 2062 with regards to known oil reserve and production rate as of 2015 (BP, 2016). The estimation of fossil fuels reserve in terms of years left was approximated using BP's reserves to product ratio data of year 2015 (Ritchie, 2016). Figure 1.2 illustrates the years of global fossil fuel reserves left based on the known available reserve and current harvest rate in 2015. These researches are evidence of the hurdles that need to be overcome in order to ensure a healthy growth and sustainability in the transportation sector.

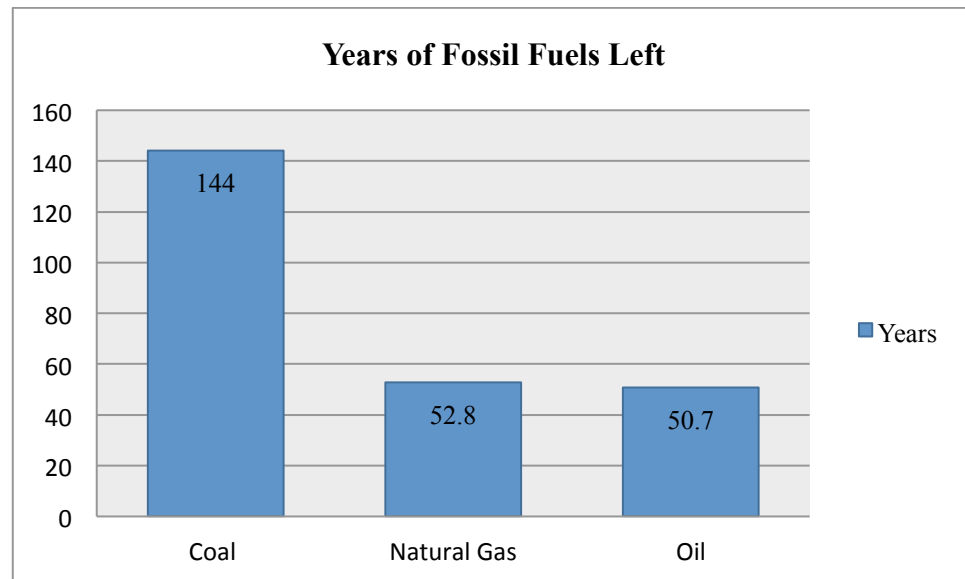


Figure 1.2: Years of Fossil Fuel Left (BP, 2016)

Due to the environmental impact and future challenges faced by ICEV, alternate solutions to a cleaner and more sustainable propulsion technology have to be considered. One of the most popular alternatives to the ICEV is the electric vehicle (EV). EV is a type of vehicle that utilised electricity as a source of energy and electric motors as its propulsion. Although serving the same function as a conventional ICEV, there are numerous advantages and disadvantages that EV possesses as compared to its conventional counterpart.

An EV is cleaner in operation, where it does not emit greenhouse gases that are harmful, besides being quieter during operation. However, the most common problem faced by EV is the limited capacity of the charge stored in its battery pack that directly limits the range reachable by the vehicle. Furthermore, the time taken to charge the vehicle is also significantly longer than the time required to replenish an ICEV fuel tank. The manufacturing technique of battery cells to be used as energy source is loosely policed, such that environmentally detrimental and unsustainable methods may still exist in some stages of the production, but governmental and regulatory policies have recently been introduced to minimise such practices. Despite the disadvantages, EV still poses as a strong contender to be the vehicle of the future, primarily based on the merits of its low environmental impact during operation.

One of the most important features that a consumer utilises and experiences in a vehicle is vehicle comfort. This is one of the most imperative and decisive

aspects to consider during the acquisition of vehicles by consumers. The cabin cooling system plays a paramount role in vehicle comfort, where its primary function is cabin climate control that regulates the temperature in the vehicle cabin. The temperature of the vehicle is closely related to the thermal comfort of the occupants. Thermal comfort is regarded as the mental state of a person that expresses satisfaction with the surrounding thermal environment (American Society of Heating, Refrigeration, and Air-Conditioning Engineers (ASHRAE), 1966). The cabin temperature must be regulated within the range of thermal comfort of its users in order to avoid various physical health and psychological ailments. If the cabin temperature is not properly regulated, its users might suffer heat stroke in presence of extreme heat or hypothermia in the presence of extreme cold. Besides that, psychological issues such as irritation and anxiety may be elevated due to improper regulation of cabin temperature. Phan observed that hospital admission for specific psychiatric symptoms is on the rise in the occurrences of global heat wave phenomenon. Additionally, those aged 65 and above showed a higher tendency to be admitted for psychiatric reasons due to this phenomenon (Phan, 2017). Thus, this finding implies that extreme temperature may lead to mental disorder; hence temperature control and thermal comfort is vital in an enclosed space, such as a vehicle's cabin.

In a consumer centric market, vehicle cabin cooling has undergone a significant evolution, from the most basic manual control form to a complex automatic control cooling system. Decades ago, cabin cooling control took the form of mechanical levers and valves, where the consumer had to manually control the air temperature, distribution and air intake level of the cabin. As technology in automation evolved, the desired cabin temperature was automatically regulated to user's selection, however air intake level and distribution still had to be manually controlled. Upon further development, all three of the parameters were controlled automatically with little intervention from the users. The information for cabin cooling in this system was centred on the driver, where the temperature of the cabin was measured within the driver's vicinity, thus providing optimal thermal comfort with respect to the driver only. According to research conducted on the New Trends in the Field of Automobile Air Conditioning, the latest iteration of cabin cooling has the capability of achieving microclimate that can provide optimal thermal comfort to each unique zone in the cabin (E. Janotkova and M. Pavelek, 1994). The latest

technology in cabin cooling today is able to independently control the climate of up to four different zones with the virtue of information fed from sensors in these zones. Equipped with these information, the on board computer is able to make adjustment to control the desired air temperature, distribution and intake level of each individual zone. These designated zones are where passengers are normally seated. Moreover, microclimate is achievable by independent control of air parameters at the top and bottom portion of the passenger. This technology can be properly harnessed for energy saving, in which air cooling requirement may be minimised or eliminated in zones where passengers are absent, hence reducing the overall cabin cooling power consumption. Thus, a multi climate and microclimate cabin cooling is possible with modern on board computer, software and independent air conditioning facilities for the comfort of passengers and energy conservation.

It can be summarised that EV is one of the best transportation solutions in our detachment from overdependence on petroleum products as energy source, and may one day completely replace ICEV. In the design phase of such a vehicle, an important consideration is the cabin cooling system, as it is one of the most critical constituents of an EV where it directly affects the comfort and wellbeing of its users.

1.2 Importance of the Study

The primary function of a cabin cooling system is to provide thermal comfort to its consumers. The thermal comfort level experienced correlates to the health and psychological state of a human being, and it acts in an adverse manner if thermal comfort is not fulfilled. Moreover, the air provided in cabin cooling is useful in defogging of the vehicle windows that ensures continual clarity of the windows and a clear view out of the vehicle.

As a cabin cooling system is one of the most noticeable supplementary features of a vehicle, it is paramount to carefully study and model its behaviour. The study of cabin cooling is especially important in an EV because of the limited energy storage system in the form of a battery pack and would adversely affect the driving range of the EV. Additionally, the energy storage cannot be replenished as quickly as an ICE vehicle could. For an EV to be marketed globally, it necessitates the EV to be able to operate in different regions around the world, thereby subjecting the vehicle to different operating climate that poses different thermal load on the cabin cooling system. Hence it is vital that the energy consumption of the cabin cooling system is

properly and efficiently managed. Equipped with the mastery and refinement of an efficient cabin cooling system, manufacturers are able to increase the EV's driving range and at the same time maximises thermal comfort of passengers in the vehicle, which in turn would reflect on the marketability and sales figure of the vehicle. On these accounts, cabin cooling is not only used to service the comfort of the users but also maintains a safe operation, as well as boosting the marketability of the vehicle.

This project is purposed to numerically model the EV cabin cooling, where the result may serve as a basis of operation for the cabin cooling system with regards to different loads applied to the system.

1.3 Problem Statement

Energy used for cabin cooling is derived from the battery pack of the EV and the energy supply has a few limitations. The battery pack used in the EV typically has a limited capacity and the charging stations are not as frequently available as compared to fuel station. Furthermore, the duration to fully charge the battery pack is also longer compared to the refuelling of a conventional ICE vehicle. A heavy load on cabin cooling directly compromises the energy available for propulsion; hence, affecting the range of the EV.

A numerical modelling may be implemented on the EV cabin cooling in order to theoretically predict the behaviour of the cabin cooling and the load imposed on the battery pack. The modelling of cabin cooling also takes into consideration of the energy usage for different climate that imposes dissimilar thermal loads on the cooling system.

1.4 Aims and Objectives

The aim of this project is to develop numerical model for EV's cabin cooling. Based on this aim, specific objectives are outlined as follows:

1. To develop a numerical model for electric vehicle cabin cooling with consideration of external climate effect using MathLab® Simulink®.
2. To validate the numerical model by comparison with experimental data.
3. To optimise the control of electric vehicle's cabin cooling.

1.5 Scope and Limitation of the Study

In a numerical modelling, assumptions and limitations have to be imposed in order to preserve the simplicity along with rationale of the modelling where critical or influential data has to be preserved and information with little to negligible effect on modelling result to be omitted.

First and foremost, the vehicle model selected for study is the Renault Zoe Electric Vehicle, manufactured by Groupe Renault that has a cabin length of 1678 mm, 1364 mm in width and 1442 mm in height. It is worth noting that the dimensions are simplified average dimension of an irregular contour of the vehicle cabin. As per the manufacturer specification sheet, the EV is powered by a Lithium-Ion battery, which has a capacity of 22 kWh.

Assumption has to be made to the properties of the air in the cabin for simplification of study. The flow of air and temperature in the cabin is assumed to be homogeneous. The temperature on the surface area of the vehicle seats and dashboard is regarded to be the temperature of the cabin space. The density and specific heat capacity of the air in the cabin are considered unchanged throughout the space of study. The humidity in the cabin space is not considered in this study.

From the thermal aspect of passengers, the latent heat from the passengers that contributes to phase change of air in the cabin without temperature rise and sensible that contributed to temperature rise of air without phase change are neglected in this study.

Furthermore, the limitation and assumptions are set upon the properties of the interior and exterior of the vehicle in study. The colour and texture of the inner and outer region of the vehicle is assumed to have negligible effect on the interior cabin temperature. The glazing and thickness on the vehicle is assumed to be uniform, thereby indicating a constant coefficient of transmissivity.

Since the climate control system in the cabin is fundamentally a refrigeration cycle, the coefficient of performance (COP) of the system is assumed to be unchanged over the range of operating temperature in the study, albeit influenced by the surrounding temperature of the system during operation.

In the calculation of overall thermal load, the heat loading from exhaust is excluded due to the nature of the studied EV. This type of thermal load is important in ICE and hybrid vehicle, but deemed insignificant in EV.

Moreover, during thermal modelling, the dynamic characteristic associated to a moving vehicle is neglected, and the vehicle is assumed to be stationary in this study.

1.6 Contribution of The Study

This project is aimed to fill in the knowledge gaps in the numerical modelling of an EV's air conditioning system.

A large majority of the journal addresses the thermal loads that contribute to the overall heating of the vehicle, however the effect of solar geometry on the thermal load of the vehicle has yet to be integrated into a single model. This study aims to incorporate the solar geometry and solar irradiance modelling into a refrigeration circuit model in order to ease the study of the effect of external climate environment on the air conditioning system of a vehicle.

This study also aims to understand the behaviour of the energy consumption of the refrigeration circuit and cabin temperature when subjected to different types of thermal load that varies in intensity and frequency. Comprehension of the energy consumption of the refrigeration system forms the fundamental in optimisation of the air conditioning system and overall energy consumption, which translates into a longer driving range for an EV.

This dissertation also looks into the effects of using supporting infrastructure in order to optimise the cabin cooling. This allows a better understanding of how supporting infrastructure is able to help reduce the thermal load as well the cabin temperature.

1.7 Outline of The Report

This report consists of a general introduction that gives reader context on the importance of the study. The literature review provides information on researches that has been conducted so far that is relevant to the study. The methodology is separated into a number of different sections, namely governing theories and formula, simulation, model validation and expansion work. The first section discusses on the thermal load formula, thermal comfort indication and cabin temperature prediction algorithm, and supporting infrastructure. The simulation section elaborates on the thermal load modelling, construction of refrigeration circuit model, integration between the two models and construction of experimental model, along with the

expansion work and supporting infrastructure. The results and discussion section is categorised according to the chronology of the work performed. The thermal load modelling will be discussed along with its validation method, followed by simulation response of the refrigeration circuit model along with its validation method. The last part in the results and discussion explored the expansion work that is possible with the thermal load modelling, which is the cabin temperature-predicting algorithm as well as the expansion work possible with the refrigeration circuit modelling, which includes the analysis of refrigeration circuit performance due to battery heat load from different driving cycles. The study of supporting infrastructure is also conducted, which utilises the refrigeration circuit model and cabin temperature-predicting model. Finally, the study is concluded and recommendations established in order to allow future expansion work on this study to achieve a higher level of accuracy and precision.

CHAPTER 2

LITERATURE REVIEW

2.1 Introduction

The current chapter concentrates on the researches undergone on the cabin cooling system on an EV, with particular focus on existing scientific journals and research papers previously published. This research is done in order to provide better understanding of this research topic.

2.2 Literature Review

This literature review covers the cooling system in vehicle, thermal load approximation approach and software, along with occupant's thermal comfort, and energy consumption of cabin cooling in an EV.

2.2.1 Cooling System in Vehicle

In order to understand the cabin cooling system used in the EV, it is critical to first comprehend the mechanism used to cool the cabin. A brief description of the mechanism is explained in this subchapter.

The cooling system in a vehicle works to either dispel or introduce heat into the vehicle cabin from its ambient environment, based on the desire of the user, in order to achieve thermal comfort. In a hot climate environment, the user may wish to have a cooler climate in the car; therefore the air conditioning system may be manipulated to dispel heat from the cabin, and vice versa in a cold outside climate. The mechanism used to achieve this objective is the refrigeration cycle, along with its four fundamental constituent, namely compressor, condenser, expansion valve and evaporator. One of the most commonly used refrigeration cycles is the vapour-compression refrigeration cycle, where the working fluid experiences compression and vaporisation in an alternate manner (Cengel and Boles, 2015). The four mentioned components are connected by tubes, in which the working fluid, also known as refrigerant travels in. Conventionally, R-12 refrigerant, also known by its trade name, Freon is used in most vehicle, but this is phased out due to its negative environmental impact, and subsequently replaced with R-134a. In this refrigeration cycle, a low-pressure vapour enters the compressor, where it is compressed to the

condenser's working pressure. Due to compression, the temperature of the vapour increases in the process. The high pressure and temperature vapour then flows into the condenser, where the hotter vapour interfaces with the cooler surrounding via a heat exchanger situated outside the vehicle cabin. Heat is rejected from the refrigerant to the surrounding environment either by natural or forced convection. Forced convection is achieved by moving air due to the vehicle movement or induced by a radiator fan. Upon exiting the condenser, the high-pressure working fluid is condensed into a liquid state. The high-pressure and relatively high temperature liquid refrigerant is passed through an expansion valve, where the liquid is throttled to a temperature below the vehicle cabin temperature with a lower pressure. The low-pressure and temperature liquid is passed through the evaporator, which is fundamentally a heat exchanger located in the cabin environment. During the refrigerant's passage through the evaporator, the liquid absorbs the heat in the cabin and vaporizes into vapour form. Variable fan and flaps provide manipulation for the amount of cool air entering the cabin. The refrigerant then re-enters the compressor, thus completing the cycle. This simple refrigeration cycle is applied to the vehicle's cooling system due to its simplicity and robustness in design.

Similar to the discussed refrigeration cycle, the air conditioning system in an EV utilises the same principle and components associated with the refrigeration cycle discussed above. The evaporator and condenser are fundamentally heat exchangers that allow effective heat transfer between the refrigerant and the surrounding air. The expansion valve is a throttling device that is used to decrease the refrigerant's temperature via a reduction of its pressure, as well as providing metering in order to restrict the refrigerant's flow rate. Lin noted one interesting aspect of the compressor in the EV is the use of an electrically driven compressor powered by electric motor. The rationale behind DC brushless motor's implementation in the design is due to its ability to vary its rotational speed, which can effectively vary the energy consumption of the air conditioning system. This system is contrary to the conventional engine driven compressor that relies on the rotational speed of the engine itself. As for the compressor type, a scroll compressor is used due to the justification made to its compactness and reliability (Lin, 2010). Additionally, Bentriac et al. also noted that the scroll compressor possesses the attribute of being quieter during operation and possessing the capability of achieving maximum volumetric efficiency, as well as suggesting that it is one of the most promising

designs. Song et al. also emphasised the importance of air conditioning design due to its heavy reliance on the energy from the electric storage unit, as the lack of heat rejected from engine for cabin heating necessitates the need to draw heating power from the battery pack. The lack of compressor coupling to an engine like in an ICE, also necessitates the rotational energy be drawn from the main battery pack (Song et al., 2015).

The performance of the refrigeration cycle can be gauged by a term known as Coefficient of Performance (COP). Cengel and Boles defined the COP of the refrigeration cycle as the ratio of heat removed from the refrigerated space over the work done in doing so, denoted as the formula below:

$$COP_R = \frac{q_L}{w_{net,in}} \quad (2.1)$$

Where,

COP_R = Coefficient of Performance of Refrigerator

q_L = Heat absorbed from refrigerated space

$w_{net,in}$ = Net Input Work

It is worth mentioning the current development of the air conditioning system that has great potential to be used in the next generation EV. One of the recent innovations is the use of Phase Change Material (PCM) in the air conditioning of future generation vehicles. Xia et al. proposed the combined use of a PCM heat exchanger with heat pump technology for EV, where the PCM possesses a single acting characteristic that operates between the cooling and heating thermal comfort temperatures. This technology was purported to fulfil the driving range extension function. The compressor, which is powered by mains during charging, operates to charge the PCM by either introducing or removing heat from it. During operation of the EV on battery, the PCM may then serve as either a heat source or heat sink, therefore offering cooling or heating capability, which reduces the air conditioning load on the battery. This effectively increases the driving range of the EV.

Moreover, the magnetocaloric air conditioner is also under current development, which can be deployed in an EV in the future. Paya et al. reported that this technology works through the principle of magnetocaloric reversible heat pump,

where it is established on the principle of magnetocaloric effect (MCE). As the magnetic moments in a magnetic material are aligned through magnetisation, the exothermic process causes heat to be introduced to the environment. The contrary effect applies when the magnetic moments are misaligned through de-magnetisation. These effects coupled with the use of heat transfer medium serve as the basis of this innovation. This system is expected to have higher efficiency than the conventional refrigeration cycle as well as environmental friendly due to lack of detrimental refrigerant (Paya, et al., 2016). The limitation to this technology is the requirement of a strong magnetism to produce a highly efficient operation. This technology has been under rigorous research and currently being put under prototype testing on an IVECO-ALTRA Daily minibus.

The cabin cooling system in an EV works on the basic refrigeration cycle based upon the vapour-compression refrigeration cycle, where this technology has been proven through time to be robust and reliable. Although it is worth acknowledging the current technologies and modification innovated to improve the efficiency of the system, this research paper will only focus on the basic form of the refrigeration cycle that utilises an electrically driven compressor. Technologies associated with the use of PCM and MCE are currently in development and prototype, therefore they will not be implemented in this research. Notwithstanding the fact that COSP provides a more comprehensive and complete indication of the system's refrigeration performance, COP will be used in this research paper, as it is a more common benchmark for refrigeration cycle performance indicator.

2.2.2 Thermal Load Calculation

According to Spitler, the quantity of heat that is removed from a definite space in order to maintain a fixed temperature is categorised as the cooling load, while the amount that is introduced is regarded as the heating load (Spitler, 2009). The cooling and heating load are otherwise known as thermal load. In order to proceed, it is required that the heat transmitted into and out of the space via conduction, convection and radiation be pre determined. The three modes of heat transfer considers the space within a boundary envelope and between the envelope with its surrounding. Although Spitler applied these principles to buildings, its concept can also be applied to EV, where the envelope is the physical boundaries enclosing the

EV, such as the vehicle's body and windows. The ambient environment in the case of the building may refer to the climate outside the vehicle's cabin.

Numerous methodologies and software have been developed over time in order to analyse and model the thermal load. Each distinctive methods and softwares encompasses their own complexity and inherent accuracy of the obtained estimation.

Iman et al. suggested that the cooling and heating load applicable to a passenger bus could be done by accumulation of heat flux from loads such as solid walls, glass, passengers, engine, ventilation and evaporator fan motor (Iman et al., 2013). The thermal loads were calculated based on the vehicle's dimensions and thermal properties as well as occupancy information and outside weather conditions.

In light of the lack of development in the accurate modelling of vehicle heat load, Zheng Y. et al. has developed a simplified procedure to estimate the vehicle heat load. The calculation considered the interior and overall vehicle geometrics such as windshield, glazing surface, roof angle and orientation of the vehicle. The solar radiation through the windshield and skylight glass is also considered in terms of directness and diffusion incidence (Zheng Y. et al., 2011). Calculation of the heat transfer between the interior and exterior of the vehicle is achieved by the U value method. Additionally, the calculation considered the introduction of heat due to infiltration, occupants and blower motors for the cabin cooling. The modelling is verified using experimental testing and it was found that there was little deviation between the modelling and experimental methods. Heat transfer through the skylight glass and wall is calculated using Cooling Load Temperature Differential (CLTD). The governing equation is presented in Equation 2.2. Heat absorbed via conduction through the glass is calculated using Equation 2.3.

$$Q = U \cdot A \cdot CLTD \quad (2.2)$$

where,

U = Overall Heat Transfer Coefficient

A = Area

$CLTD$ = Cooling Load Temperature Differential

$$Q = U \cdot A \cdot \Delta T \quad (2.3)$$

Where,

U = Overall Heat Transfer Coefficient

A = Area

ΔT = Change in temperature between interior and exterior of cabin

In order to quantify and calculate thermal load, two fundamental methods are applicable, namely the Heat Balance Method (HBM) and Weighting Factor Method (WFM) (ASHRAE, 2009). The methodology that takes into account greater details and less assumption is the HBM, where thermal calculation incorporates several fundamental models. On the contrary, it is easier to utilise WFM in calculating thermal load in a vehicle, albeit being less accurate than HBM. Hence, HBM is recommended if a greater amount of detail is provided for modelling, such as information on the vehicle properties and thermal loads (Kamar et al., 2012).

For the purpose of cooling loads calculation, Pedersen et al. developed a complete heat balance procedure. His procedure is summarised into four different steps, namely the exterior surface heat balance, wall heat balance, interior surface heat balance and air heat balance. It is worth noting the depth of information provided in the model should correspond with the purpose of study (Pedersen et al., 1997). Therefore, the details we input into the model should be based upon the output and accuracy we wish to obtain from the modelling. Excessive amount of information without significant effect to the output is generally undesirable in order to conserve computing power and time.

Furthermore, another HBM to approximate the overall thermal load is by considering the heat loads that act on the vehicle cabin, which can be categorised into nine distinctive types. The aggregate of all these types is considered the overall cabin heat load (Vinofer and Rajakumar, 2016). Equation 2.4 provides the relationship of these factors. Each element of the thermal load has its distinctive formulation and respective parameters.

$$\begin{aligned} \dot{Q}_{Tot} = & \dot{Q}_{Met} + \dot{Q}_{Dir} + \dot{Q}_{Dif} + \dot{Q}_{Ref} + \dot{Q}_{Amb} \\ & + \dot{Q}_{Exh} + \dot{Q}_{Eng} + \dot{Q}_{Ven} + \dot{Q}_{AC} \end{aligned} \quad (2.4)$$

Where,

\dot{Q}_{Met} = Metabolic load

\dot{Q}_{Dir} = Direct radiation load

\dot{Q}_{Dif} = Diffuse radiation load

\dot{Q}_{Ref} = Reflected radiation load

\dot{Q}_{Amb} = Ambient load

\dot{Q}_{Exh} = Exhaust load

\dot{Q}_{Eng} = Engine load

\dot{Q}_{Ven} = Ventilation load

\dot{Q}_{AC} = Air Conditioning Cycle load

In view of a research published by Fayazbakhsh and Bahrami, they used the above HBM to approximate the heating and cooling load in a vehicle passenger's compartment, where they proposed such modelling should be used as a completely standalone model. Among the inputs they have included are the vehicle passenger's compartment geometry and material properties. They implemented their modelling in a software code and applied two different driving and ambient condition to their model. They summarised that a predictive model can be developed in accordance to the driving conditions, vehicle velocity, placement and geographical position, where it is able to predict near future changes in passenger's comfort level in real time. This is useful in automatic manipulation of the cabin cooling in order to minimise energy consumed by the cabin cooling system, whilst at the same time preserving the consumer's thermal comfort (Fayazbakhsh and Bahrami, 2013).

Additionally, Abdulsalam et al. performed a research on a vehicle's instantaneous response to real world usage, specifically on the cooling load of the cabin. In their research, they focused on the cooling calculation using HBM that considered the nine distinctive heat loads that takes into the occupant's metabolism, direct, diffused and directed solar irradiation, as well as ambient, exhaust, engine, ventilation and air conditioning loads at three distinctive time with their own specific conditions. They performed modelling through the simulation tool provided by

MATLAB/GUI®, using vehicle parameters of a Honda Freed, which is a type of ICEV. In their study, based on the respective conditions and climate, it was found that a negative cabin load was necessary to decrease the cabin temperature to the occupant's comfort level (Abdulsalam et al., 2015).

In a research undergone by Alexandrov et al., they studied the flow pattern and heat transfer in a generic vehicle cabin by using two and three-dimensional Computational Fluid Dynamics (CFD) in order to examine the function of the air conditioning configuration and design (Alexandrov et al., 2001). The parameters studied include temperature and velocities of the inlet air, size, quantity and location of the air inlets and outlets. The research was also inclusive of exterior ambient temperature and vehicle velocity effect on the vehicle cabin climate condition. Through CFD techniques, they found that these parameters hold important functions in ascertaining the cabin cooling's efficiency.

Moreover, Arici et al. developed a software package that possesses the capability to study and simulate the operation of a vehicle's climate control system, where the instantaneous cabin compartment temperature and relative humidity can be predicted (Arici et al., 1999). These were achieved by performing detailed analysis through simulation of every constituent member of the air conditioning system, with the aim to develop software in order to mitigate the cost and time incurred during the construction and testing of an actual air conditioning prototype.

Besides that, Breque and Nemer developed a model that was purposed to study the detailed transient and single zone model with the aim to predict the thermal requirements of a vehicle cabin. They developed the model using DYMOLA environment and more specifically through the MODELICA language. The research considered the three modes of heat transfer, air conditioning and water vapour effects. At the end of the research, an instantaneous thermal model was developed where it was less sensitive to numerous non-trivial modelling factors. On the contrary, in some cases, the result was inaccurate when inner radiation and internal thermal nodes were ignored. Based on the research, it was implied that thermal needs significantly affects the EV driving range, especially when the cabin climate control was used in the heating mode (Breque and Nemer, 2017).

Kiss and Chaney performed a research to investigate the use of a new simulation tool called MATLAB®/SIMULINK® in modelling a vehicle's cabin cooling system. They suggested that vehicle simulation models, typically used by the

Original Equipment Manufacturer (OEM) lacked accuracy as these models worked with less amount of information. The modelling performed constituted a comprehensive cooling circuit model and a simple cabin model. In their modelling, which was performed on MATLAB®/SIMULINK® and verified using measured data, they found that both results were close to each other both on system and component level. It was also concluded that the model developed was able to respond to fast transients that occurred in a vehicle cabin cooling system. The model was also optimal to be used for simulation with other vehicle system analysis software, where this can be capitalized for the development of cabin air conditioning system in order to achieve a more optimum overall system performance (Kiss and Chaney, 2013).

Different researchers have previously utilised different method and approach in estimating the thermal load of a vehicle. The same HBM employed by Vinofer and Rajakumar, Fayazbakhsh and Bahrami, as well as Abdulsalam et.al, is common and popular due to its simple and accurate estimation, which was formulated specially for vehicles. The nine different types of thermal load that cumulatively contribute to an overall thermal load of the vehicle are governed by their respective formula and can be easily found by inserting their parametric values. Therefore, this fast, straightforward and effective approach will be implemented in this research paper, coupled with MATLAB®/SIMULINK© that provides a user-friendly software interface, which is simple in operation, as well as providing accurate results on both system and component level.

2.2.3 Occupant's Thermal Comfort

As previously explained, thermal comfort plays an important part in the marketability of a vehicle and also affects the health and psychological wellbeing of the consumer. As thermal comfort is subjective, there have been numerous efforts aimed to quantify this subject in order to facilitate more objective and meaningful analysis.

The Fanger's comfort equation is one of the most accepted methods to quantify thermal comfort, where it takes into account of quantified environmental and individual factors (Ekici, 2013). The environmental factors comprise of air temperature, mean radiant temperature, relative air speed and relative humidity, while the individual variables include human activity level and clothing insulation

(Hensen, 1990). According to Ekici, the result from Fanger's comfort equation, known, as Predicted Mean Vote (PMV) is an avenue for indication of an occupant's thermal comfort level in a certain climate. Therefore, the Percentage of People's Dissatisfaction (PPD) may be derived from the PMV. This method is currently accepted globally as a model to indicate the mean thermal comfort level of humans in an enclosed space.

Variables in Fanger's model affect the human thermal comfort index in varying way depending on the size and type on the indoor environment. Simion et al. conducted a study to analyse the variables affecting thermal comfort in a vehicle cabin, where in their research, they categorised the factors into measurable and personal. The former included air temperature, velocity and relative humidity, as well as radiant temperature, whilst the latter constituted the type of clothing and human activity level. They managed to quantify all the variables involved in this research and found that the factors are independent of each another but its aggregate contributed to the thermal comfort index. They theorised that alteration had to be made to other variables if one variable changes in order to preserve thermal comfort. They noted that the vehicular environment was inherently different from the building environment, where air temperature was found to have a closer relationship with relative humidity. The physical human was also established to possess greater sensitivity to air flow velocity in vehicular environment that it does in a building environment. The solar radiation was also a more influencing factor for thermal comfort in a vehicle cabin than an indoor environment for a building (Simion et al., 2015).

Additionally, Musat and Helerea conducted a research analysis that investigated the thermal comfort of occupants in a vehicle cabin, so as to improve measurement techniques and to substantiate the optimum thermal comfort for the occupants in the vehicle cabin. Maintaining a vehicle cabin at temperatures between 20 °C to 25 °C through manipulation of cabin air temperature, delimitation of areas, humidity and air velocity with regards to the individual variable, as well as preventing occupants from contacting surfaces with extreme temperatures helped to achieve occupants thermal comfort (Musat and Helerea, 2009). The estimation of thermal comfort in this study was performed based on mathematical and physical model, which consisted of the Fanger's model and thermal manikin model (Berkeley's Model) respectively. A thermal manikin has the capability of giving

measurement and assessment of thermal condition without actual human specimen that provides an avenue to determine the most optimal solution to thermal control. The thermal comfort level of occupants was obtainable through the environmental and individual variables, where it was determined that the two most crucial factors were cabin's air temperature and relative humidity. On the contrary, humidity fluctuation holds a lesser role in thermal comfort level if it is within the range of 30 % to 70 %.

In order to target the accuracy gap from previously available thermal comfort model, Neacsu et al. initiated a research on the global and absolute thermal comfort level in a vehicle cabin in order to determine the thermal comfort index with greater accuracy of the whole vehicle instead of individual occupants like the ones obtainable from standard methods. This was done using numerical simulation method, by initially creating a Computer Aided Design (CAD) geometry, which underwent a shell finite element modelling, and realisation of the Theseus-FE calculus. The individual occupant's thermal comfort was indicated from the PMV, PPD and Dynamic Thermal Sensation (DTS). In this study, a further step was taken to calculate the Global Thermal Comfort Index (GTCI) and General Absolute Thermal Comfort Index (GATCI) that indicated the thermal comfort level of the whole car (Neacsu et al., 2017). Therefore, this method allows the comprehension of not only the thermal comfort index of each occupant, but also the overall vehicle thermal comfort level, thereby giving a better representation for analysis.

Alahmer and Omar made a comparison study between the Fanger's and Berkeley's model. The Berkeley's model uses virtual thermal manikin simulation to estimate the thermal comfort in a vehicle occupant compartment under distinct environmental conditions, and it is quoted in the Overall Thermal Sensation index (OS). On the contrary, Fanger's model uses the PMV index to indicate thermal comfort of the occupants (Alahmer and Omar, 2014). At the end of the study, they concluded that the Berkeley's model produced thermal comfort windows that were more robust to deviation in environmental factors and personal variables as compared to the Fanger's model. Additionally, the Berkeley's model had a better capability in obtaining local sensation than its counterpart.

The focus of this research paper is on the numerical modelling of the EV's cabin cooling system along with its energy consumption; therefore less emphasis is placed upon the accuracy of the thermal comfort. From the above methods, the most

suitable approach to indicate thermal comfort of occupants in this research is the one extracted from research by Musat and Helerea, where they concluded that the cabin temperature and relative humidity played important roles in thermal comfort. The approach in this research is to focus on the pivotal cabin temperature used by Musat and Helerea. This approach gauges the thermal comfort through observation of the cabin air temperature, where thermal comfort is deemed to exist in an EV's cabin environment with temperatures between 20 °C to 25 °C.

2.2.4 Energy Consumption

The air conditioning system in a vehicle is one of the primary consumer of energy in an operating vehicle, despite itself being an auxiliary system. Therefore it is worth exploring the impact of the system to the overall energy consumption of the vehicle, especially that of EV, along with innovations to reduce the energy drawn by this system.

Mebarki et al. conducted a simulation research to study the effects of the cabin cooling system on the overall energy consumption of an EV that was fitted with a Lithium-Ion battery. The cabin cooling system consumed more power than other auxiliary car system, which depleted a significant amount of power in the battery that resulted in a reduction of range reachable by the EV (Mebarki et al., 2013). The simulation of the cabin cooling system was constructed on a MATLAB®/SIMULINK® platform, where the result was subsequently analysed. They implied that the outside climate temperature affected the energy consumption of the vehicle, where if the temperature exceeds the thermal comfort temperature of 24 °C, the energy consumption would be raised in order to compensate for the rising outside temperature with the aim of preserving the thermal comfort of the occupants. The exterior ambient temperature was a significant factor that relates to the peak-cooling load of the air conditioning system.

Li et al., where they initially reviewed all the variables influencing the power usage of an EV during operation, and subsequently constructed an empirical study on the factors, conducted a study in the energy consumption of an EV. The empirical approach was based on the testing of a 2011 Nissan Leaf in Sydney. At the end of the research, it was found that the two main variables that significantly affected the energy consumption of the EV was the operating topology and the air conditioning system, which was validated through a derived binary model (Li et al., 2014). The

combined effects of these variables varied the driving range of the EV between 100 km to 222 km.

Furthermore, Evtimov et al. conducted an analysis on the power demand of accessory system in an EV, where the energy consumption for all the systems were broken down and analysed. In a particular breakdown on the climate control system, it was stated that the typical cabin temperature was kept in the range of 20 °C to 23 °C, and the power consumed in maintaining the range was dependent upon the difference of temperature between the interior and exterior environment (Evtimov et al., 2017). Thus, it was obvious that variation of the external climate greatly affected the power demand of the EV. This was primarily attributed to the heating and cooling of the air conditioning system, as well as the battery efficiency in different climate. They theorised that in order to attain a minimal energy demand from the air conditioning system, the external climate should ideally be at 20 °C.

Broglia et al. took a system simulation approach in order to analyse the power usage and cabin temperature of an EV, where the effect of external climate temperature on the EV power usage was approximated. The cabin cool down and heat up accounted for a significant portion of the power demand from the EV battery, in which driving range would be detrimentally affected due to low ambient temperature as a result of high power demand from the heat up process (Broglia et al., 2012). Excessively high ambient temperature also affected the driving range in a negative manner as a result of more work done by the electrically driven compressor. The simulation resulted in data for cabin temperature changes, state of charge (SOC) of battery pack and effect on the driving range. The numerical modelling in this research successfully predicted the energy usage of the EV, and it can be further applied to different conditions, provided changes to the parameter are properly manipulated.

A study conducted by Farrington et al., investigated the impact of cabin cooling load on the energy consumption of EV and hybrid electric vehicle. As mandated by recently implemented policies, where the manufacturers were motivated to reduce the vehicle air conditioning size, Farrington et al. theorized that this could be achieved by minimising the cabin soak temperature without sacrificing occupant's thermal comfort (Farrington et al., 1999). They concluded that a vehicle operating on a typical air conditioning unit could negatively affect the EV reachable range by 40 %, where this value was dependent upon the air conditioning size and

driving pattern. Thus, in order to reduce the cabin soak temperature, they recommended and validated the use of advanced vehicle glazing and cabin compartment ventilation as effective methods to achieve that.

In light of development in reducing the energy consumption from the air conditioning system, Kondo et al. devised a system to reduce the power consumption in EV and hybrid electric vehicle due to cabin heating. Conventionally, electric water heater system was used to provide heat to cabin, but the energy consumption of such system was heavy on the vehicle, thus Kondo et al. suggested the use of heat pump technology that obtains heat from the outside ambient environment to provide heating to the cabin interior (Kondo et al., 2011). They validated their method through physical experimentation and found that the energy consumption was effectively reduced using this method, whilst maintaining occupant's thermal comfort in the cabin. If implemented on EV and hybrid electric vehicle, it was estimated that the heat pump technology would be able to decrease the power demand of total air conditioning by 20 % to 60 % on comparison with conventional technology.

Another method to reduce the energy consumption from the air conditioning system was analysed by Khayyam et al., where they studied the impact of energy consumption of vehicle with and without the implementation of Energy Management System (EMS). The function of the EMS was to instantaneously manipulate the fan speed and opening of the vents with response to different heat and loads conditions, with the objective of adjusting the mass flow rate of air (Khayyam et al., 2009). Through simulation of the EMS, they found that the vehicle employing EMS was capable of maintaining occupant's thermal comfort at a lower energy demand from the air conditioning unit, where the energy demand with and without the EMS were 7.59 MJ and 14.4 MJ per 2400 seconds respectively.

Lastly, Farzaneh and Tootoonchi conducted a research on the optimised controller of a vehicle air conditioning system, where the aim was to maintain thermal comfort in the cabin whilst at the same time minimising the energy consumption through modification of the fuzzy controller (Farzaneh and Tootoonchi, 2007). The evaporator cooling capacity indicated the energy usage. Thermal comfort was analysed using the PMV index, but simplified to only two factors, namely occupant's compartment ambient temperature and air speed, without the occurrence of notable errors. Two versions of fuzzy controller were modified to receive the

PMV index and temperature as its feedback input. Through simulation, it was found that the former version was able to achieve thermal comfort faster and minimised energy usage as compared to the latter. Thermal comfort was achieved at a higher rate at a lower energy consumption was later achieved by the implementation of genetic algorithm on the fuzzy controller. Finally, the controller was tested for its robustness and proven to be robust as it was able to respond to changes in system factors.

Various researches have reached the conclusion that the cabin cooling system has a significant negative impact on the energy stored in the EV's battery pack, therefore affecting the maximum driving range of the vehicle. Furthermore, improvement on the energy consumption of the cabin cooling system is also discussed, where improvement can be implemented through the use of advanced glazing, cabin ventilation, use of heat pump technology, EMS and modification to the cabin cooling system's fuzzy logic controller.

2.3 Summary

The literature review looks into the basic cooling principle of the vehicle's cabin cooling system, thermal load calculation approach and software associated with the vehicle cabin, along with the passenger's thermal comfort analysis as well as the energy consumption of vehicle due to the cabin cooling system and ways to reduce its consumption.

The basic cooling system explains the refrigeration principle, which is the vapour-compression refrigeration cycle with its associated components and performance index.

The thermal load calculation approach explores the different type of methods and software used to approximate the thermal load in a vehicle's cabin. The most popular approach is the HBM that categorised thermal loads into nine distinct thermal loads. There was also numerous types of software for analysis, with MATLAB®/SIMULINK® being one of the most comprehensive and popular among researchers.

In the analysis of thermal comfort, the simpler method to quantify this state of mind is Fanger's model where environmental and personal factors are considered in the calculation that resulted in the PMV index. Another popular method is the Berkeley's model that is more complex due to the use of virtual or physical thermal

manikin. However, in this research paper, the method selected is the maintenance of cabin temperature within the human thermal comfort temperature range of 20 °C to 25 °C.

From the researches being performed on the energy consumption of EV, it is found that the ambient temperature, which directly implies that the cabin cooling system, holds an important role in the energy usage of the EV. Various methods have been recommended to minimise energy consumption, while bearing in mind to maintain the thermal comfort of the cabin occupants. These methods include implementation of advanced glazing, cabin ventilation, heat pump technology, utilisation of EMS and modification to the fuzzy controller of the cabin cooling system.

CHAPTER 3

METHODOLOGY AND WORK PLAN

3.1 Introduction

The methodology is a structured manner this particular research is approached. Information obtained in the literature review is used to establish the methodology of this research. The work plan for this entire research is visually represented in Figure 3.1.

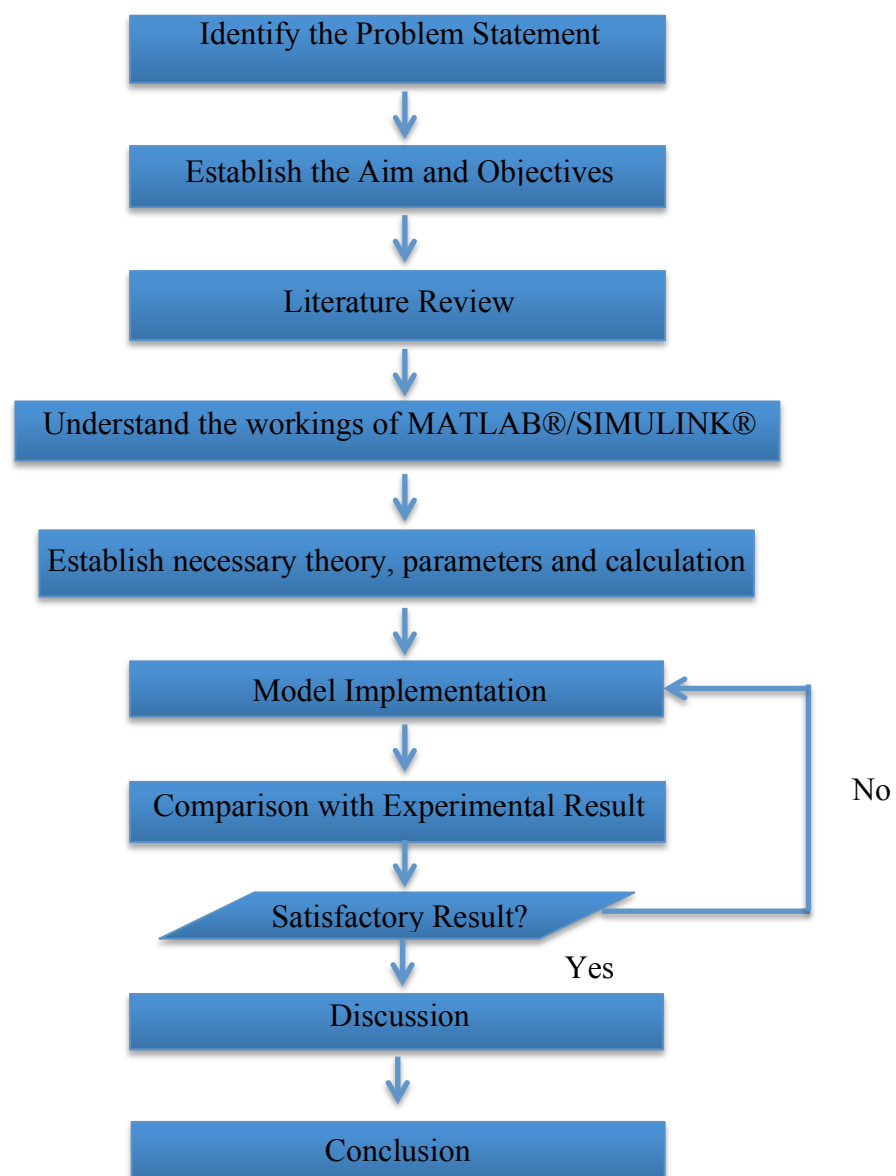


Figure 3.1: Research Flow Chart

The Model Implementation represents the construction and simulation of the respective model with refinements introduced if the experimental result does not agree with the response from the experimental model. The Model Implementation can be elaborated into four different phases as illustrated in Figure 3.2.

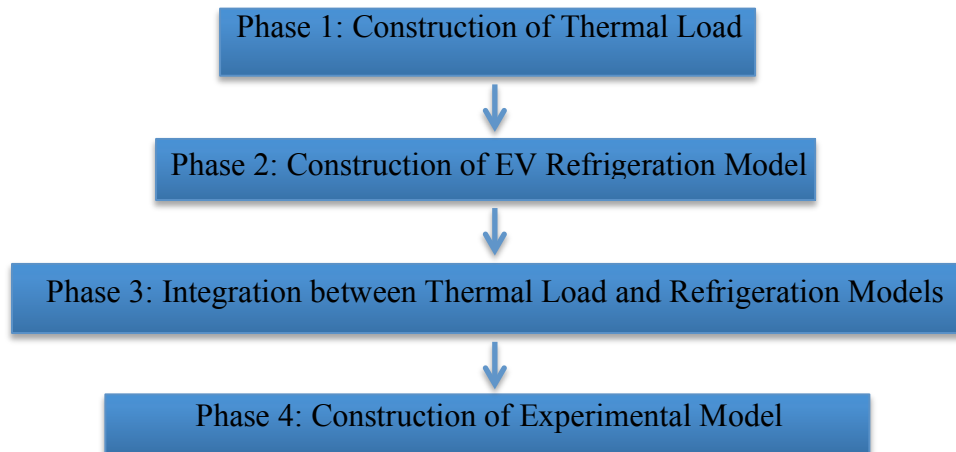


Figure 3.2: Expansion of Model Implementation

Initially, the necessary governing theories, formula and parameters will be established, where elaboration will only be theoretical and mathematical based, without references to MatLab® Simulink®.

In the second subsection, discussion will be conducted in the different phases as depicted in Figure 3.2, where this sequence will provide a better understanding on the chronological order of the work performed, with reference to MatLab® Simulink®. After the models have been duly verified, expansion on the current model can be commenced, which includes application battery thermal load due to different driving cycles on the refrigeration circuit, construction of cabin temperature-predicting algorithm and study of effects supporting infrastructure on the cabin temperature and combined thermal load.

3.2 Governing Theories and Formula

The following subsections will examine in depth the relevant theories, formula and methods utilised in order to satisfy the aim of this research.

3.2.1 Thermal Load Calculation

This subsection explores the thermal load calculation of an EV along with its pertinent theory and formula, as well as any modification and its respective justification to such amendment.

As previously mentioned, there are two fundamental methods to analyse the thermal load acting on a vehicle. The WFM is simpler in its implementation but it sacrifices details and accuracy during calculation. On the contrary, HBM is more sophisticated and tedious during calculation, but it is useful in preserving the accuracy of the thermal load. The method chosen for this research is the HBM with the nine categories of thermal loads, as a higher level of accuracy is desired, with simplicity given a lower priority. Fayazbakhsh and Bahrami stated that the overall thermal load on a vehicle is the summation of individual distinct thermal load. The mathematical representation of this statement is in the form as shown by Equation 2.4.

The first thermal load type is the metabolic load, which represents the heat generated and radiated by the human body from the driver and passengers alike. The heat is generated by the body itself in order to sustain the body temperature at its optimal level of 37 °C. The heat radiated by the body is also introduced to the cabin environment; hence it is considered as a heat source or thermal load for the cabin compartment. It is assumed that there is always a driver in the vehicle, and the number of passenger is varied from zero to a maximum of four. The mathematical representation of this the metabolic thermal load is described in Equation 3.1, where M is the human metabolic thermal generation rate and A_{DU} is surface area of the occupants. According to ISO 8996:2004, the human metabolic heat rate for a driver is 85 W/m^2 , while the passenger is quoted to be 55 W/m^2 . A_{DU} also known as the DuBois area is calculated using Equation 3.2, where W and H is the weight and height of the respective occupants. The weight and height of the occupants are taken to be 82.59 kg and 1.685 m respectively, as per the average adult weight and height in the US (US Department of Health and Human Services, 2016).

$$\dot{Q}_{Met} = \sum_{Occupants} MA_{DU} \quad (3.1)$$

$$A_{DU} = 0.202W^{0.425}H^{0.725} \quad (3.2)$$

In the HBM method, direct, diffused and reflected solar radiation has been considered as three separate entities. Direct solar radiation is a type of solar radiation that is in direct contact with the vehicle's surface. Another type of solar radiation is known as the diffused radiation, which is regarded as the kind that strikes on clouds and diffused onto the vehicle's surface. This often occurs during cloudy days, where the direct solar radiation diffused after passing through the cloud. This type of solar radiation is also known as the indirect radiation. The third type of solar radiation is the reflected solar radiation that is due to reflection of solar radiation from the ground and subjecting on the vehicle's surface. However, they may be combined together in order to represent the total thermal load on the EV due to solar radiation. Equation 3.3 represents the total solar radiation from every direction of the vehicle, where τ_B , τ_D , and τ_G are beam/direct, diffused, and reflected transmittance respectively. $I_{B,TLT}$, $I_{D,TLT}$, and $I_{G,TLT}$ are beam/direct, diffused, and reflected slope irradiance respectively, and A is the surface area of the subject window. Doyle has ascertained both τ_D , and τ_G to be 0.676 and 0.660 for 4 mm and 5 mm windows respectively. The area for each window surface is listed down in Table 3.1 for Renault Zoe EV.

$$\dot{Q}_{solar} = \sum_{\substack{Side\ 2\ Glazing \\ Windshield}} (\tau_B I_{B,TLT} A + \tau_D I_{D,TLT} A + \tau_G I_{G,TLT} A) \quad (3.3)$$

Table 3.1: Area (in m²) and Thickness (in mm) of Window Surface for Renault Zoe EV (Doyle, 2017)

Window Surface	Area, m ²	Thickness, mm
Windshield	0.48	5
Front Side Glazing	0.23	4
Rear Side Glazing	0.22	4
Rear Windshield	0.24	4

In order to obtain the remaining parameters, solar geometry has to be initially computed, starting with the sun's position, which is quoted in Solar Altitude (SOLALT) and Solar Azimuth (SOLAZM) both denoted in degrees. The former parameter represents the angle of elevation between the sun and horizon, whereas later signifies the location of the sun's beam on the earth's plane, where the angle increments in clockwise from North. Equation 3.4 and Equation 3.5 are the formula for both SOLALT and SOLAZM.

$$SOLALT = \sin^{-1}(\sin LAT \sin DEC + \cos LAT \cos DEC \cos SHA) \quad (3.4)$$

$$SOLAZM = \cos^{-1}\left(\frac{\cos DEC (\cos LAT \tan DEC - \sin LAT \cos SHA)}{\cos (SOLALT)}\right) \quad (3.5)$$

LAT represents the latitude position of the subject vehicle, DEC is the angle between the sun-earth vector and equatorial plane, and SHA is the solar hour angle. The latter two formulas are denoted in Equation 3.6 and 3.7 respectively. All the variables involved are elaborated between Equation 3.8 to Equation 3.15. The independent input variables are d , m , y , λ , h , min , and sec are the day, month, year, longitudinal position of the subject vehicle, hour, minute and second at the time of simulation. It is worth noting that if G , L and SHA lies do not lie between the range of 0° to 360° , then multiples of 360° should be added to or subtracted from the calculated value. Another important solar geometry is the angle of incidence; θ shown in Equation 3.16, where ASP is the aspect of the vehicle and TLT is the angle of slope of the vehicle's window. The aspect and slope angle for each window surface is tabulated in Table 3.2.

$$DEC = \tan^{-1}(\tan \varepsilon \tan \alpha) \quad (3.6)$$

$$SHA = 15UT - 180 - C + L - \alpha \quad (3.7)$$

$$\varepsilon = 23.4393 - 0.013T \quad (3.8)$$

$$T = \frac{\left(\frac{UT}{24}\right) + d + (30.6m + 0.5) + (365.25(y - 1976)) - 8707.5}{365.25} \quad (3.9)$$

$$UT = t_{LAT} + \left(\frac{\lambda}{15}\right) \quad (3.10)$$

$$t_{LAT} = h + \left(\frac{min}{60}\right) + \left(\frac{sec}{3600}\right) \quad (3.11)$$

$$\alpha = L - 2.466 \sin 2L + 0.053 \sin 4L \quad (3.12)$$

$$L = 280.46 + 63000.77T + C \quad (3.13)$$

$$C = 1.915 \sin G + 0.02 \sin 2G \quad (3.14)$$

$$G = 357.528 + 35999.058T \quad (3.15)$$

$$\theta = \cos^{-1}(SOLALT \cos(SOLAZM - ASP) \sin TLT + \cos TLT \sin SOLALT) \quad (3.16)$$

Table 3.2: ASP (in °) and TLT (in °) of Window Surfaces for Renault Zoe EV (Doyle, 2017)

Window Surfaces	ASP, °	TLT, °
Windshield	ASP	26
Side 1 Glazing	ASP-90	77
Rear Windshield	ASP+180	50
Side 2 Glazing	ASP+90	77

At this point, the beam/direct transmittance can be ascertained using the angle of incidence via Equation 3.17. The normal transmission ratio, τ_n is found to be 0.82 for a 4 mm thick glazing and 0.8 for a thicker 5 mm glazing, as per Muneer et. al..

$$\tau_B = \tau_n(\cos \theta + \sin^3 \theta \cos \theta) \quad (3.17)$$

The ground reflected slope irradiance, $I_{G,TLT}$ can be easily found using only one governing equation based on the information currently known. Equation 3.18 is used to find this parameter, with G denoting ground surface reflectivity and I_G is the global irradiance obtainable from the local meteorological station of interest. The ground solar surface reflectivity is dependent upon the ground surface on which the body of interest is on, and the values corresponding to different surfaces are tabulated in Table 3.3.

$$I_{G,TLT} = GI_G \sin\left(\frac{TLT}{2}\right)^2 \quad (3.18)$$

Table 3.3: Reflectivity Coefficient of Surface Types (Thevenard & Haddad, 2006)

Surface Types	Reflectivity Coefficient
Water	0.07
Dry Bare Ground	0.20
Weathered Concrete	0.22
Grass	0.26
Desert Sand	0.40
Light Building Surfaces	0.60

The computation of diffused slope irradiance, $I_{D,TLT}$ requires certain conditions be known before proceeding with the final formula. The conditions to be determined are the extra terrestrial radiation, I_{ERAD} and clearness index, k_t as depicted in Equation 3.19 and Equation 3.20 respectively. Equation 3.19 is only applicable if both extra terrestrial radiation and global irradiance is non-zero; otherwise clearness index will also take a zero value. DN in Equation 3.18 denotes the day number of the day of interest, where 1st January is denoted as the first day and 31st December as 365th day or 366th day on leap years. Furthermore, diffused irradiance, I_D can then be calculated using the information at hand, via Equation 3.21.

$$I_{ERAD} = 1367(1 + 0.033 \cos(0.01720254DN)) \sin SOLALT \quad (3.19)$$

$$k_t = \frac{I_G}{I_{ERAD}} \quad (3.20)$$

$$I_D = I_G(1.006 - 0.371k_t + 3.124k_t^2 - 12.7616k_t^3 + 9.7166k_t^4) \quad (3.21)$$

If $I_{ERAD} > I_G$, then Equation 3.22 will be utilised to find the diffused slope irradiance, $I_{D,TLT}$, with variable X expressed in Equation 3.23 for shaded and overcast condition, otherwise I_D will take the same value as I_G . The value of variable b in the latter equation is associated with the day's climate, with Table 3.4 establishing the conditions and values of b to be used. However, in sunlit and non overcast condition, diffused slope irradiance, $I_{D,TLT}$ is computed using Equation 3.24 with variable F and r_B denoted in Equation 3.25 and Equation 3.26 respectively.

$$I_{D,TLT} = I_D X \quad (3.22)$$

$$X = \left\{ \cos^2 \frac{TLT}{2} + 2b[\pi(3 + 2b)]^{-1} \left(\sin TLT - TLT \cos TLT - \pi \sin^2 \frac{TLT}{2} \right) \right\} \quad (3.23)$$

Table 3.4: Conditions and Relevant Values of $2b[\pi(3 + 2b)]^{-1}$ (Muneer et.al., 2000)

Description	Condition	$2b[\pi(3 + 2b)]^{-1}$
Shaded Condition	$\theta > 90^\circ$	0.252
Overcast Condition	$I_G - I_D < 5 Whm^{-2}$	0.168
Sunlit, Overcast	-	$0.00333 - 0.415F - 0.6987F^2$

$$I_{D,TLT} = I_D [X(1 - F) + Fr_B] \quad (3.24)$$

$$F = \frac{I_G - I_D}{I_{ERAD}} \quad (3.25)$$

$$r_B = \frac{\cos \theta}{\sin SOLALT} \quad (3.26)$$

Lastly, the beam/direct slope irradiance can be found by virtue of two simple formulas, as shown in Equation 3.27 and Equation 3.28 respectively.

$$I_B = I_G - I_D \quad (3.27)$$

$$I_{B,TLT} = I_B r_B \quad (3.28)$$

Substituting all the calculated parameters into Equation 3.3 allows the beam/direct, diffused and reflected thermal load to be calculated, where the summation of thermal load on all window surfaces gives the total solar thermal load on the vehicle.

Moreover, thermal ambient load refers to the heat introduced to or absorbed from the cabin compartment due to the difference in temperature between the interior and exterior environment of the vehicle. This form of heat load is represented in its mathematical form in Equation 3.29, where U is the total coefficient of heat transfer due to internal convection, surface conduction and external convection. Equation 3.30 represents the total coefficient of heat transfer. T_o , T_s , and T_i represents the external environment, surface and internal cabin temperatures respectively. Constants h_o and h_i are convection coefficients for the external and internal cabin environments respectively, meanwhile λ is the surface thickness and k is the thermal conductivity of the surface. Besides that, Muneer et al., estimated the heat convection coefficient of the internal and external environment using a common formula, depicted in Equation 3.31, where V is the speed of the vehicle. The application of this formula assumes that the air in the cabin compartment is stationary and the external environmental air velocity is the speed of the vehicle. For practicality, the vehicle is also assumed to be stationary. Another assumption is made where the cabin and exterior ambient temperatures are the same as the cabin and exterior surface temperature, therefore T_s in Equation 3.9 is ignored. The thermal conductivity of vehicle materials were compiled by Muneer et al. and Khayyam et al., where it is shown in Table 3.5. Doyle measured and calculated indoor cabin dimensions of the Renault Zoe EV and their SU values, which are compiled in Table 3.6.

$$\dot{Q}_{Amb} = \sum_{Surfaces} SU(T_o - 2T_s + T_i) \quad (3.29)$$

$$U = \frac{1}{\frac{1}{h_o} + \frac{\lambda}{k} + \frac{1}{h_i}} \quad (3.30)$$

$$h = 0.6 + 6.64\sqrt{V} \quad (3.31)$$

Table 3.5: Thermal Conductivity (in W/m²K) of Vehicle Materials (Muneer et al., 2000; Khayyam et al., 2011)

Components	Material	Thermal Conductivity, W/m ² K
Window	Glazing	5
Door Material	Polypropylene	4
Roof Material	Polypropylene	4
Floor Material	Polypropylene	4

Table 3.6: Indoor Cabin Dimensions (in m²) and Their *SU* Values in (W/K) (Doyle, 2017)

Components	Total Area, m ²	SU values, W/K
Door Panels	2.08	8.3
Roof Surface Area	2.02	8.1
Floor Surface Area	2.40	9.6
Back Window Space	0.19	0.8
Front Windshield and Dashboard Area	1.35	6.8
Back Windshield Area and Seat	0.51	2.6
Front Cabin Window to Roof Area	0.50	2.5
Rear Windows to Roof Area	0.49	2.5

The next type of thermal load to consider is the heat generated from the exhaust, which is present and significant on ICEV and hybrid vehicles. However, this type of thermal load is absent from the EV due to the utilisation of electric motor as its propulsion system as compared to the ICE in ICEV and hybrid vehicle, thereby

eliminating the expulsion of hot gases from the engine. The exhaust thermal load is therefore not considered in the overall thermal load calculation of this research.

Additionally, in a conventional ICEV and hybrid vehicle, another important source of heat generation is from the combustion of their engine. This heat is attributed to the inefficient working of ICE, where it is only 30 % efficient, with the rest of the energy converted to various other sources, mainly heat. The engine-generated heat may penetrate through the vehicle bulkhead and into the cabin, contributing to the overall cabin thermal load. On the contrary, an EV motor is 80 % efficient, thus less heat is generated from the engine, which is capable of penetrating into the cabin space. Therefore, the thermal load due to the engine is not considered in an EV due to its insignificance as compared to and ICEV or hybrid vehicle.

Ventilation is an important feature to include in a compartment that houses occupants, due to the need of constantly replenishing the air inside the enclosed space. Due to human respiration, the carbon dioxide level increases over time in the enclosed space, thus necessitates a constant supply of fresh air to replenish the stagnant air in the cabin compartment. A flow of air is drawn from the outside atmosphere and a similar amount is expelled to the external environment. Air is expelled to the external environment through cabin leakages due to pressure difference between the cabin interior and exterior environment. This air leakage is assumed to be the mass flow rate of fresh air into the cabin, where for a small sedan car, this value is approximately 0.02 m³/s. This phenomenon causes a ventilation load on the overall thermal load of the cabin, which is described mathematically in Equation 3.32, where \dot{m}_{ven} is mass flow rate of fresh air, e_o and e_i are enthalpies of the ambient and passenger compartment environment. Singh et al. presented the mathematical formulation to calculate the enthalpies, as depicted in Equation 3.33, where T represents the air temperature and X is ratio of humidity, in units of gram of air over gram of dry air. The X coefficient is again defined using Equation 3.34, where ϕ , P_s , and P are the relative humidity, pressure of air and pressure of water saturation at T temperature. The relative humidity in Malaysia is approximated from the neighbouring Singapore's National Environmental Agency Annual Relative Humidity Data, where the average relative humidity is 80%. Furthermore, in order to compare the result with Doyle's thesis, where the experiment is conducted in Edinburgh, UK, the relative humidity of the location is also found to be 80%,

according to weatheronline.co.uk. The pressure is assumed to be at atmospheric pressure of 101.325 kPa and the pressure of water saturation at T temperature is calculated using Teten's Formula. Monteith and Unsworth commented that this formula is accurate within the range of 0 °C to 50 °C, where it is also highly applicable in metrological calculation. Teten's formula is stated in Equation 3.35.

$$\dot{Q}_{ven} = \dot{m}_{ven}(e_o - e_i) \quad (3.32)$$

$$e = 1006T + (2.501 \times 10^6 + 1770T)X \quad (3.33)$$

$$X = 0.62198 \frac{\phi P_s}{100P - \phi P_s} \quad (3.34)$$

$$P_s = 0.61078 \exp \frac{17.27T}{T - 237.3} \quad (3.35)$$

The next type of load contributing to the overall thermal load is the air conditioning load, which the air conditioning system creates depending on the system and operating characteristics. A positive load is known as heating due to the need to introduce heat during a typical cold external climate into the cabin, and a negative load, also known as cooling due to hot outside climate that necessitates heat to be removed from the cabin. The mathematical equation to describe this thermal load is described in Equation 3.36. In this particular mathematical expression, m_a and c_a define the mass and specific heat of cabin air; DTM , T_{comf} , and t_c are the thermal inertia of elements in the compartment excluding cabin air, thermal comfort temperature per standards of ASHRAE and pull-down constant respectively. The pull-down constant is described using Equation 3.37. The required amount of time to reach the thermal comfort temperature from an initial cabin temperature, T_o is regarded as the pull down time, t_p . However, this load will not be considered in the simulation process, as some of these parameters cannot be accurately established.

$$\begin{aligned} \dot{Q}_{AC} = & - \left(\dot{Q}_{Met} + \dot{Q}_{Dir} + \dot{Q}_{Dif} + \dot{Q}_{Ref} + \dot{Q}_{Amb} \right. \\ & \left. + \dot{Q}_{Exh} + \dot{Q}_{Eng} + \dot{Q}_{Ven} \right) \\ & - (m_a c_a + DTM)(T_i - T_{comf})/t_c \end{aligned} \quad (3.36)$$

$$t_c = 0.62198 \frac{t_p}{\ln(T_o - T_{comf})} \quad (3.37)$$

An addition to the Equation 2.4 is the battery thermal load in the case of an EV. The EV draws power from the battery pack, where charging and discharging of the battery pack generates heat. The heat generated is significant due to the large size of the battery pack, and possesses the capability to penetrate into the cabin environment from the cabin floor. A Renault Zoe EV has a 6 x 210 Lithium Ion cells with a total capacity of 22 kWh. Based on simple calculation, it is found that the battery pack consists of a total of 1260 cells. It is assumed that 0.1 W of heat from each cell penetrates into the cabin environment, thus an aggregate thermal load of 126 W is introduced into the cabin environment. The battery thermal load is stated in Equation 3.38.

$$\dot{Q}_{Batt} = 0.1 \text{ W}(1260 \text{ cells}) \quad (3.38)$$

Based on the original HBM formula that constitutes of nine different types of heat load, addition and omission has been introduced in order to modify Equation 2.4 for application on EV. Exhaust, engine thermal load, and air-conditioning load have been removed, while battery thermal load has been added to the formula. Formula 3.39 states the modified formula that is suitable for use on thermal load calculation of an EV.

$$\begin{aligned} \dot{Q}_{Tot} = & \dot{Q}_{Met} + \dot{Q}_{Dir} + \dot{Q}_{Dif} + \dot{Q}_{Ref} + \dot{Q}_{Amb} \\ & + \dot{Q}_{Ven} + \dot{Q}_{Batt} \end{aligned} \quad (3.39)$$

3.2.2 Thermal Comfort Indication

As previously mentioned in the literature review, there are two acceptable common methods to indicate occupant's thermal comfort in a vehicle, namely Franger's Model and Berkeley's Model.

Due to the complexity and amount of steps required for both of these methods, a simpler indication of thermal comfort will be used. Musat and Helerea mentioned the importance of cabin temperature in preserving thermal comfort, where temperatures between 20 °C to 25 °C are considered as ideal thermal comfort temperature. In this research paper, the thermal comfort temperature is designated as 23 °C, which is in the middle of the range proposed by Musat and Helerea.

3.2.3 Cabin Temperature Predicting Calculation

The thermal load model can be further expanded to include the function of predicting the cabin temperature. Changes in cabin temperature are mainly dependent on the solar irradiance and ambient thermal load acting on the cabin space, which can be predicted if the thermal loads are known. Equation 3.40 predicts the cabin temperature in the next instance of observation. Variables t_{i+1} , t_i , τ , m , and c denote predicted temperature, initial cabin temperature, time interval between observations, mass of the vehicle and specific heat of indoor space.

$$t_{i+1} = t_i + \frac{\tau[Q_{Total} - (UA(t_i - t_o))]}{mc} \quad (3.40)$$

3.2.4 Cooling Capacity of Supporting Infrastructure

The study on the supporting infrastructure of the cabin cooling is to satisfy the third objective, which is the optimisation control of cabin cooling. Supporting infrastructure, which may be classified as passive or active cooling infrastructure, can assist the overall EV's cabin cooling. Passive cooling infrastructure is supporting element added to the vehicle in order reduce the cabin temperature without any energy consumption by the infrastructure. Active cooling infrastructure is supporting element added to the vehicle in order to achieve the same purpose, but it requires energy to be consumed.

Passive cooling infrastructure that will be considered and explored in this study is the glazing of the vehicle window. The fundamental differences between a

single, double and triple glazed window is their respective transmission value, which are 0.82, 0.67 and 0.56 respectively (Muneer, et. al., 2000). A triple glazed window will stop a higher amount of solar irradiance than a single glazed window, thus reducing the solar thermal load into the cabin space. The effects of cabin temperature due to different transmission value used will be studied.

Active cooling infrastructure that will be studied in this thesis is the use of extractor fan to impart an airflow in the cabin, thus allowing the heated air to be dispelled out of the cabin space, effectively reducing the cabin temperature. In this study, two 21 W extractor fan will be used to impart the airflow that allows heated air to be drawn out, thus applying a cooling load on cabin space. The energy used for the extractor fan can be derived from the solar cell installed on the roof and bonnet of the EV. This solar cell capitalises on the solar irradiance striking the surface of the vehicle, which converts the solar energy into electrical energy, which is subsequently routed to an auxiliary battery that is used to store and supply power to the extractor fan. The cooling capacity of the extractor fan is calculated using Equation 3.41; meanwhile the cabin temperature changes can be predicted using Equation 3.42.

$$\dot{Q}_{Ext} = \dot{m}_{ext}c(T_i - T_o) \quad (3.41)$$

$$t_{i+1} = t_i + \frac{\tau[Q_{Total} - Q_{Ext}(UA(t_i - t_o))]}{mc} \quad (3.42)$$

Where:

\dot{Q}_{Ext} is the cooling capacity of the extractor fan.

\dot{m}_{ext} is the air flow imparted by the extractor fans, which is 0.0801 kg/s in this case.

3.3 Simulation

The theoretical result in this research is obtained using thermal modelling of the studied EV. The modelling is separated into four different stages that are performed using a powerful modelling tool known as MATLAB®/SIMULINK®. The different stages of modelling are illustrated in Figure 3.2.

This particular platform is selected due to its popular usage in the study of air conditioning in the industry, as compared to the other OEM software, such as

“Autonomie”. Simulink® is preferred by engineers due to its ability to preserve the accuracy of simulation, and more importantly the ease to interface and consolidate the air conditioning model into an entire vehicle model built on the same platform (Kiss and Chaney, 2013). This capability not only saves time but also unlocking the ability to analyse the effect of the air conditioning system on the entire vehicle holistically.

Thermal load modelling (Phase 1) is performed using the mathematical functions in the SIMULINK library. Basic mathematical functions such as addition, subtraction, product, division and exponential blocks will be used along with constant and signal builder as inputs, as well as scope and display as output display. These functions are linked together to build each of the thermal load equations, where these chains of blocks will perform mathematical function on the inputs and give an output results that represents the thermal loads.

The EV refrigeration model (Phase 2) is constructed using Simscape™ within the MatLab® Simulink® environment, where various components of a physical system can be represented on this platform. Additionally, this platform allows for simulation of physical system that has been built, where the data for a variety of parameter can be logged and recorded on the time domain.

Phase 3 of the simulation requires the integration of the thermal load model with the refrigeration model in order to observe the response of the refrigeration model based on parameter variations in the thermal load model. This step necessitates the thermal load model's signal to be conditioned to ensure proper operation on the Simscape™ platform.

Phase 4 is concerned with the construction of an experimental model, where the experimental refrigeration test rig is digitally represented on the Simscape™ platform. The results will also be logged, recorded and compared with the response from an actual experimental test rig.

Lastly, in the expansion work, battery thermal load generated by the different driving cycles are applied to the refrigeration circuit model, where their effects are studied. The cabin temperature predicting model is also constructed and used along with the refrigeration circuit model to study the effect of supporting infrastructure on the cabin and refrigeration circuit parameter.

3.3.1 Phase 1: Thermal Load Modelling

The thermal load model is subdivided into subsystems purposed to provide a clearer segregation between components of respective type of thermal loads, besides presenting a more visually appealing and uncluttered look of the model. The subsystem symbolises the different thermal loads that constitutes the entire thermal load model. The basis of modelling in this phase is the translation of governing mathematical equations into links of mathematical blocks using addition, subtraction, multiplication, division and exponential blocks from the Simulink® library.

The first subsystem is the metabolic thermal load that includes both driver and passenger metabolic thermal load, where both of these subsystems are modelled separately due to the difference in metabolic rate, with the driver and passenger emitting 85 W/m^2 and 55 W/m^2 respectively. The driver metabolic thermal load model is depicted in Figure 3.3 and Figure 3.4 respectively. Both inputs and outputs of the model are located on the left and right side of the model respectively. The input to the driver model is modelled using a “Constant” block signifying the presence of a driver, with 0 representing the absence and 1 representing the presence of the driver.

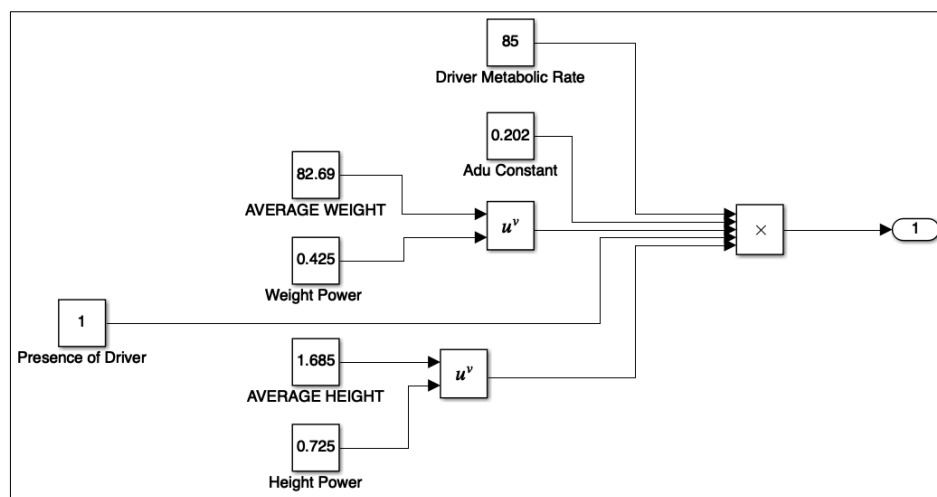


Figure 3.3: Driver Metabolic Thermal Load Model

The input to the passenger is also modelled using a “Constant” block, which denotes the number of passengers in the vehicle. As the Renault Zoe EV is a small sized sedan with a maximum legal passenger capacity of four passengers, excluding driver, the range for this block is limited from zero to a maximum of four passengers.

Users may manually input the number of passengers using the “Constant” block to output the passenger metabolic load or automatically vary the number through the range of possible passengers based on time using a “Signal Builder” Block found under “Sources” in the Simulink® library. Figure 3.5 shows the input of “Signal Builder” block, where the number of passenger increases by one after 1000 seconds, ranging from zero to four passengers. Output for both models are modelled using “Outport” block denoted by the number “1”.

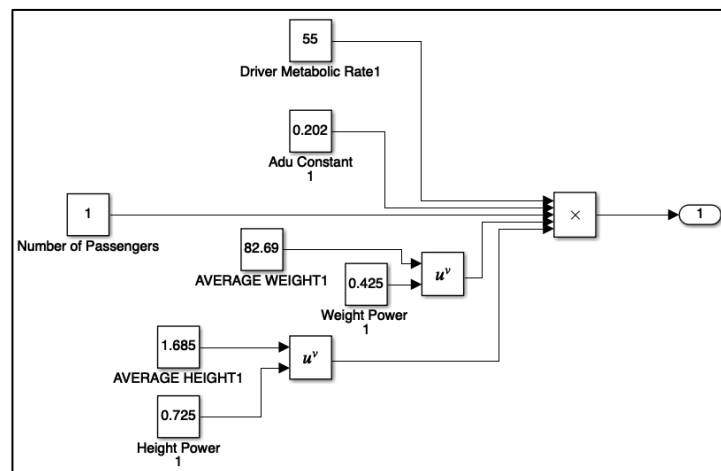


Figure 3.4: Passenger Metabolic Thermal Load Model

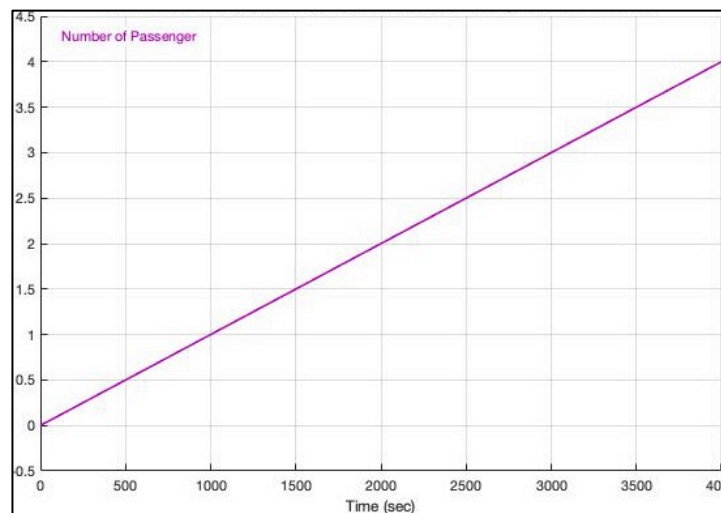


Figure 3.5: Variation of Passenger with Time

The next subsystem deals with the ambient heat load, where heat is introduced based on the temperature difference between the interior and exterior of the vehicle. The exterior temperature was chosen as the input variable, as the interior

temperature is a function of the thermal load, thermal conductivity of the vehicle, area of cabin space, exterior temperature, mass of car and the specific heat of the cabin space. As the focus of this study is the exploration of the effects of external climate on the cabin cooling, it furthers justified the choice of exterior temperature as the manipulated variable. The subsystem for ambient thermal load is depicted in Figure 3.6. The input is modelled using a “Constant” block denoting the exterior temperature and the output of the model is modelled using “Output” block.

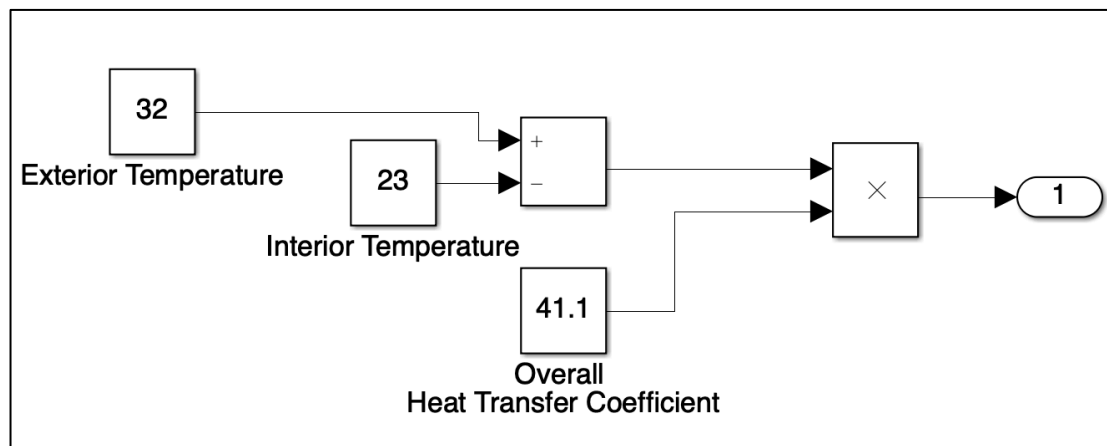


Figure 3.6: Ambient Thermal Load Model

The battery thermal load has been assumed to be fixed at 126 W as mentioned in the previous subsection, therefore the model is relatively simple, where only a “Constant” block is used with an value of 126 to represent the thermal load for battery.

The ventilation thermal load subsystem can be further subdivided into smaller subsystems based on the four governing equations as shown in Figure 3.7. Equation 3.12 is modelled as seen in Figure 3.7, where the top and bottom portions signify the enthalpies of both the ambient and cabin space respectively. The inputs for this model are the ambient and cabin space temperature, where intermediate results such as saturation pressure, humidity ratio and enthalpies are calculated in stages in order to obtain the final ventilation thermal load. Expansion of saturation pressure, humidity ratio and enthalpy equations for ambient condition can be found in Appendix A.

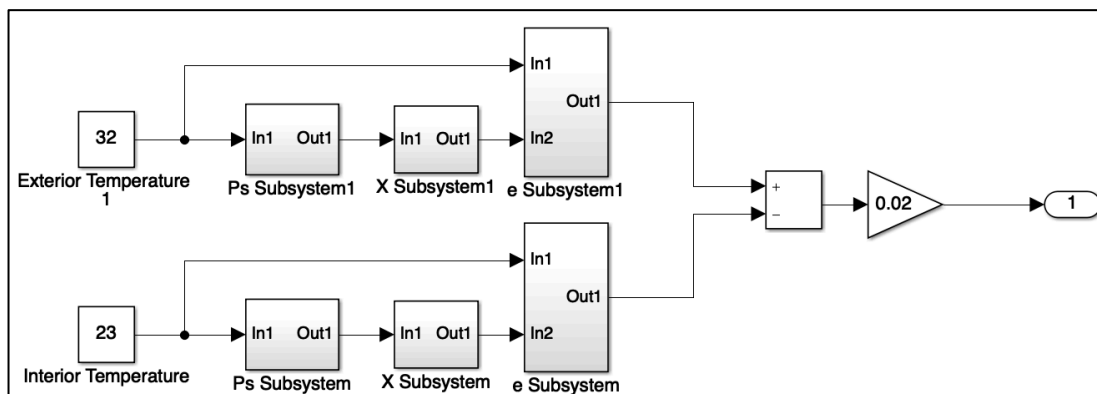


Figure 3.7: Ventilation Thermal Load Model

The last and most complicated thermal load model is the one due to solar irradiation, as represented in Equation 3.3. Instead of individually modelling beam/direct, diffused and reflected solar irradiation, and these parameters are consolidated into a single model with inputs shown in Figure 3.8. This model allows a variety of factors to be manipulated, including time, date and location of observation, aspect of the vehicle, tilt angle of the window surfaces, the reflectivity coefficient of the surface on which the vehicle is located at, and the global horizontal irradiation of the particular day of observation.

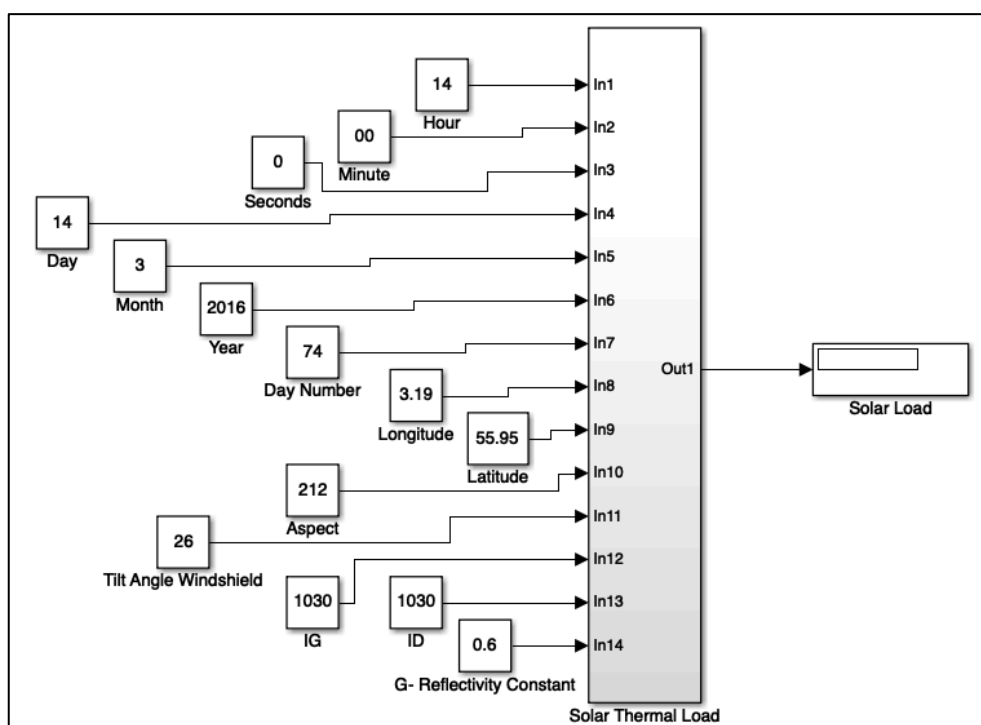


Figure 3.8: Base Level of Solar Thermal Load Model

The next level into the model categorises the window surfaces on which solar irradiation act on, along with their respective solar load as output and this is shown in Figure 3.9. The governing equations for all window surfaces are the same, save for certain parameters such as tilt angle, surface area, transmittance, aspect and thickness of the windows. Therefore exploring one of the window's models is self explanatory for the rest.

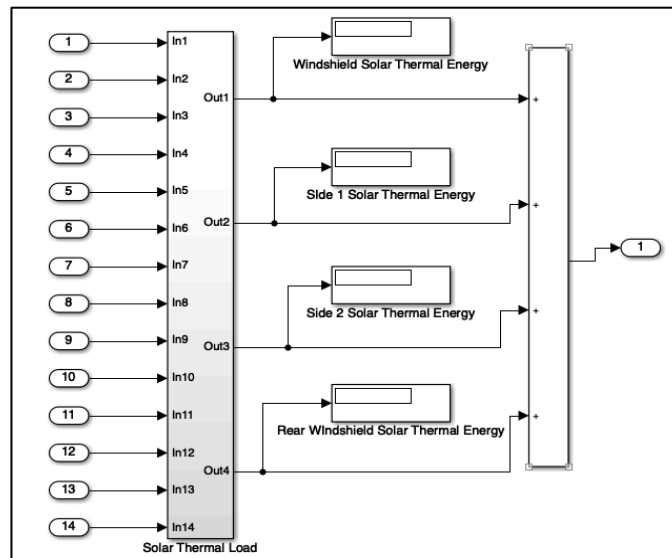


Figure 3.9: Level Two of Solar Thermal Load Model

Considering the windshield subsystem, five different subsystems are additionally subdivided in order to ascertain the solar load through this surface, as shown in Figure 3.10. These subsystems include major clumps of relevant formula such as those for solar geometry and slope irradiance, as well as simpler equations used for calculation of extra terrestrial radiation, I_{ERAD} , beam/direct transmittance, τ_B , and summation of the beam/direct, diffused and reflected solar irradiation. Effort will only be made to elaborate further on the two major subsystems as they are additionally broken down into smaller subsystems, The minor subsystems in level three will not be discussed, as they only consists of governing equations as discussed previously, which can be easily constructed using blocks from the library. Figure 3.11 shows the link of subsystems in the solar geometry model and Figure 3.12 shows the link of subsystems in the slope irradiance model.

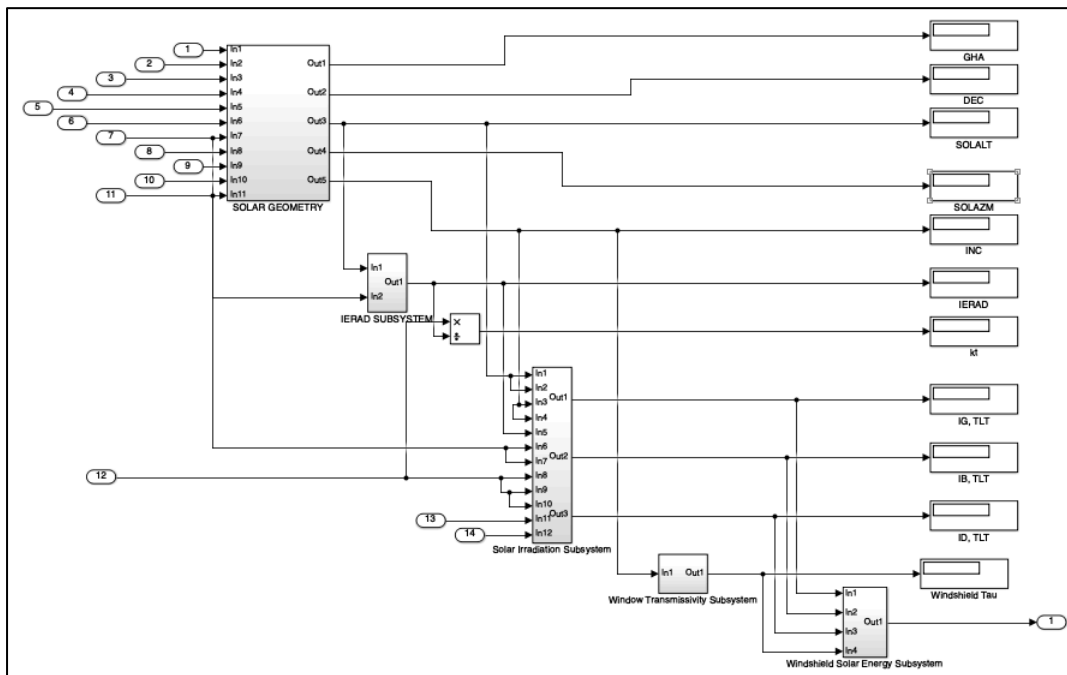


Figure 3.10: Level Three of Solar Thermal Load Model

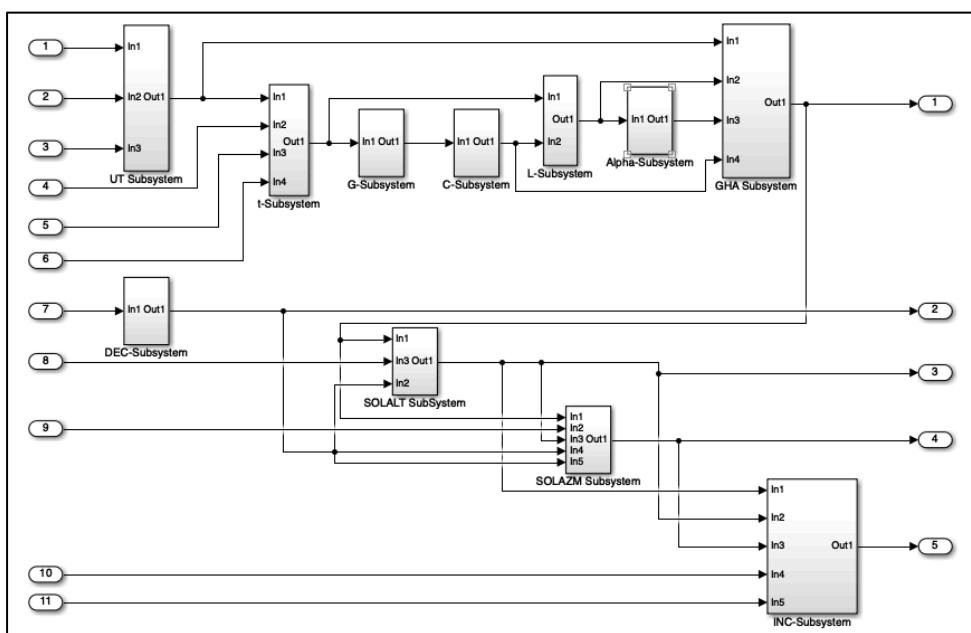


Figure 3.11: Solar Geometry Subsystem as Expanded from Level Three

In the solar geometry, five different outputs are desired, as indicated by the five “Output” blocks on the right side of Figure 3.11, namely GHA, DEC, SOLALT, SOLAZM, and INC denoting the Solar Hour Angle, angle between the sun-earth vector and equatorial plane, Solar Altitude, Solar Azimuth Angle, and angle on inclination. Various inputs are symbolised by the “Inport” blocks on the left side of

the figure. Each subsystem in Figure 3.11 represents the solar geometry equations discussed in the previous section.

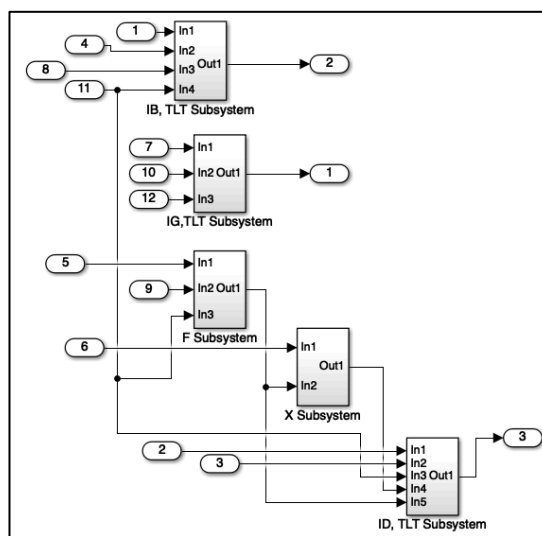


Figure 3.12: Slope Irradiance Subsystem

The equations necessary for determining the beam/direct, diffused, and reflected slope irradiance are grouped in the respective subsystems. The beam/direct and reflected slope irradiance subsystems contains relatively simple construction and blocks, as the equations used are straight forward and do not have any conditions imposed upon them. In the case of diffused slope irradiance, prior to the calculation of the slope irradiance, climate condition such as shaded, overcast or sunlit and non-overcast has to be established. The determination of which equations to used based on the conditions imposed can be achieved through “If Else” block under “Ports and Subsystem” category in the Simulink® library, where the quantification of the condition can be referred to in the second column of Table 3.4.

It is worth noting that the angles in the governing equation are based in degree, while computation of values in Simulink® are performed in radian. Thus, “Degree to Radian” and “Radian to Degree” blocks have to be used accordingly, at both the inputs and outputs of the links of governing equation blocks.

3.3.2 Phase 2: Construction of EV Refrigeration Model

After the thermal load model has been constructed, the next model that has to be established is the EV refrigeration model. This model can be similarly constructed in the MatLab® Simulink® environment, however it has to be done through the Simscape™ platform. The two major differences between the modelling environment between this model and the previous model are the types of blocks and signals used. In this environment, the blocks used are representation of components in a physical system, and the signals used are physical signal instead of Simulink® signals.

The basic refrigeration circuit is archived in MatLab® itself, coded as `ssc_refrigeration` along with its respective parameters. Based on the default parameters in the circuit, it can be implied that this refrigeration cycle is used in a domestic refrigerator. As the basics and operating principle are the same in both refrigerator and vehicle's air conditioner, the archived template serves as the base of the model construction. Alteration in the components, component arrangements and parameters will be subsequently discussed. The arrangement of components in the refrigeration model is depicted in Figure 3.13, where this refrigeration circuit is a two-phase fluid refrigeration system operating on R134a refrigerant.

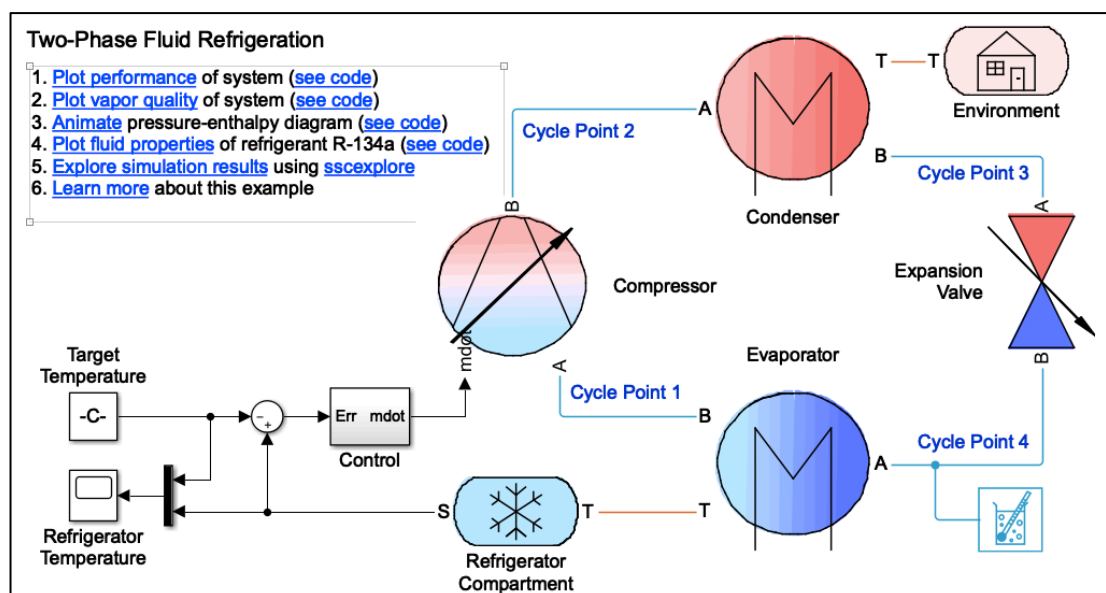


Figure 3.13: Two Phase Fluid Refrigeration Model

As previously mentioned, the parameters in the template of the refrigeration cycle belong to a domestic refrigerator; they have to be altered to the parameters of an air conditioning unit in a small sized EV. The altered parameters are listed in Table 3.7.

Table 3.7: Parameters for Refrigeration Circuit of Air Conditioning Unit in an EV

Parameter	Values	Units
Commanded Mass Flow	0.004	Kg /s
Condenser Length	10	m
Controller Time Constant	20	s
Copper Conductivity	400	W /m.K
Copper Density	8940	mg /cm ³
Copper Specific Heat	390	J/kg C
Environment Temperature	303	K
Evaporator Length	10	m
Exterior Surface Area	10	m ²
Fin Area	1	m ²
Fin Convection Coefficient	150	W/m ² K
Foam Conductivity	0.03	W /m.K
Foam Thickness	0.03	m
Initial Pressure	0.6	MPa
Initial Quality	0.05	-
Interior Surface Area	7	m ²
Maximum Throat Area	1.5	mm ²
Maximum Throat Temperature	250	K
Minimum Throat Area	0.1	mm ²
Minimum Throat Temperature	270	K
Natural Convection Coefficient	20	W/m ² K
Pipe Diameter	0.01	m
Pipe Thickness	0.0005	m
Target Temperature	296	K

As seen from Figure 3.13, the major components in the refrigeration circuit are compressor, condenser, expansion valve, evaporator, environment, and refrigerator compartment/ cabin space. Auxiliary components include the target temperature setting, control circuit and refrigerator/cabin space temperature indication.

In the auxiliary component, the target temperature setting is constructed using a “Constant” block that allows user to input the target temperature of the cabin space. In this project, the target temperature is taken to be the thermal comfort temperature of 23 °C. The refrigerator temperature scope indicates the actual temperature in the cabin space, as measured using physical sensor. The control circuit measures the difference between the target temperature and the actual temperature in the cabin space, where the temperature error is converted into mass flow rate data that serves as an input to the compressor.

The compressor is a component that compresses and drives the refrigerant around the refrigeration circuit, and the components of this subsystem are shown in Figure 3.14.

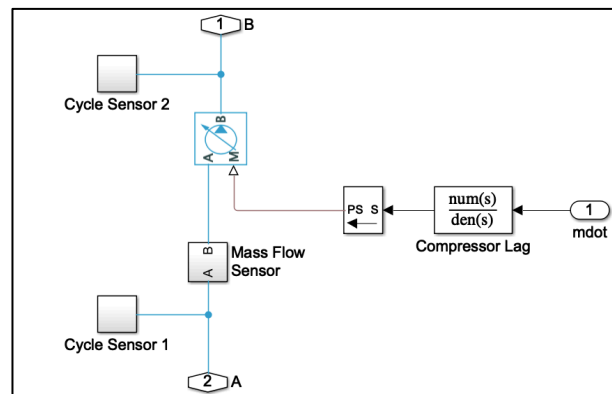


Figure 3.14: Compressor Subsystem

The compressor accepts mass flow rate data input from the control circuit through “Inport 1”, denoted as \dot{m} , which goes through a compressor lag block, to include the time required for the compressor to accelerate or decelerate, after which, the data is passed through a Simulink® to Physical System (SPS) Signal Converter before feeding to the Controlled Mass Flow Rate Source (CMFRS) block. The refrigerant flows from Physical Modelling Connection (PMC) port 2A to port 1B. The CMFRS block imparts isentropic power on the refrigerant, driving it at the mass

flow rate commanded by the control circuit. Cycle sensors 1 and 2 are included before and after the CMFRS to report the temperature, specific enthalpy, specific volume, vapour quality and specific internal energy of the refrigerant. The mass flow sensor reports the mass flow rate before the CMFRS block to be used as calculation through comparison with the commanded mass flow rate.

The refrigerant then flows to the condenser to allow for heat transfer to the outside environment. The subsystem for condenser is shown in Figure 3.15.

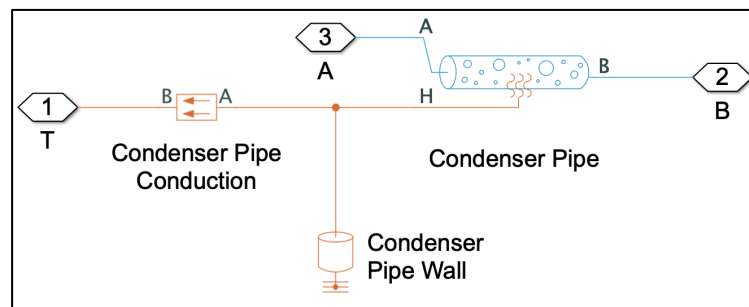


Figure 3.15: Condenser Subsystem

The refrigerant flows through the condenser pipe from PMC port 3A to port 2B, where heat is expelled to the to PMC port 1T through conduction. The conduction is modelled using the red lines, which includes the thermal mass and conductive heat transfer block. The thermal mass block represents the internal energy storage in the heat network and the conductive heat transfer block models the conduction of heat through the copper pipe. The parameters for condenser pipe are listed in Table 3.8.

Table 3.8: Parameters for Condenser Pipe

Parameter	Values
Internal Surface Absolute Roughness	1.5e-5
Laminar Flow Upper Reynolds Number Limit	2e+3
Turbulent Flow Lower Reynolds Number Limit	4e+3
Shape Factor for Laminar Flow Viscous Friction	64
Nusselt Number for Laminar Flow Heat Transfer	3.66

The heat from PMC port 1T is transferred to the environment subsystem, as shown in Figure 3.16. This subsystem represents the external environment the EV is in.

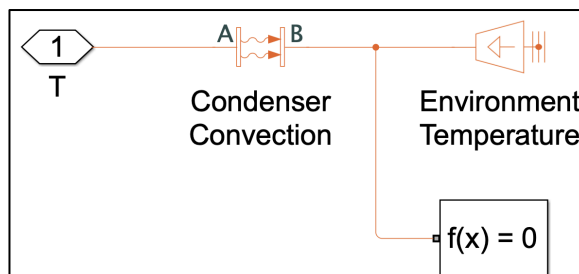


Figure 3.16: Environment Subsystem

The heat flows through the environment through convection, as represented by the condenser convection block. The convection effectiveness is governed by the fin area and heat transfer coefficient of the condenser. The environment temperature is represented using a Temperature Source block that models an ideal energy source, which maintains an absolute temperature irrespective of the heat transfer.

After the condenser, the refrigerant is channelled through the expansion valve that throttles the refrigeration, reducing its pressure and temperature. The expansion valve subsystem is shown in Figure 3.17.

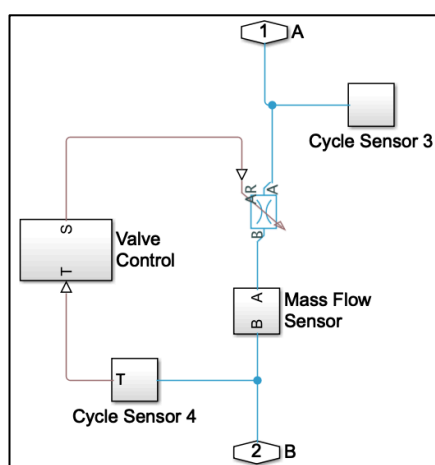


Figure 3.17: Expansion Valve Subsystem

The refrigerant flows from PMC port 1A to PMC port 2B, passing through a Variable Local Restriction (VLR) block and Mass Flow sensor, where the latter is used to measure and report the mass flow rate. The VLR block is used to model the

throttling effect of the expansion valve, where the restriction area is varied between the range of its minimum and maximum restriction area as listed in Table 3.7. It has a discharge coefficient of 0.7 and laminar flow pressure ratio of 0.999. Cycle sensors are located before and after the VLR block to detect and report parameters similar to the cycle sensors in compressor. The commanded restriction area for VLR block originates from the valve control that receives output from the cycle sensor after throttling. The valve control subsystem is illustrated in Figure 3.18. The valve control accepts input from PMC port 2T, which contain the information on the temperature after throttling from Cycle Sensor 4. This information is compared with the minimum throat temperature, generating an error signal that passes through a valve gain that outputs the change required in throat area via interpolation. The summation of error signal and minimum throat area is the commanded restriction area that is converted to the unit of m^2 before being sent to the VLR block via PMC port 1S.

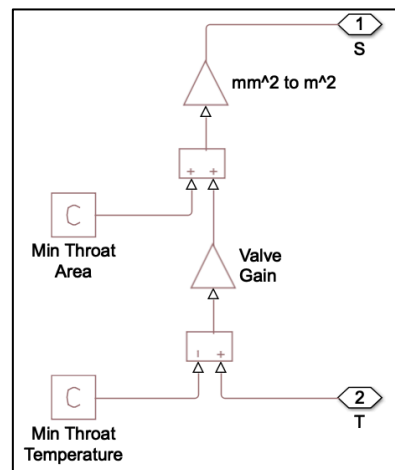


Figure 3.18: Valve Control Subsystem

The refrigerant enters the evaporator upon exit from the expansion valve, where the subsystem for evaporator can be seen in Figure 3.19.

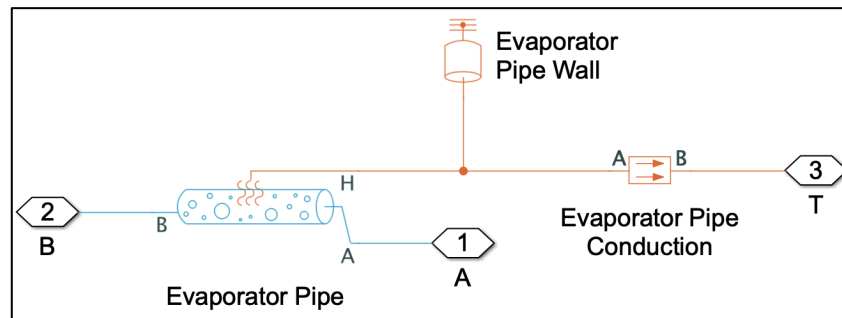


Figure 3.19: Evaporator Subsystem

The operating principle of evaporator is similar to the condenser, with the only difference being the heat transfer direction. The refrigerant flows through the evaporator pipe from PMC port 1A to port 2B, where the evaporator pipe has the same parameter as Table 3.8. The direction of heat flow originates from the cabin space via PMC port 3T and subsequently transfers into the evaporator pipe through convection.

The heat extracted from the refrigerated/ cabin space flows to the evaporator pipe, where this subsystem will be covered more in depth in the next subsection.

3.3.3 Phase 3: Integration between Thermal Load and Refrigeration Model

The integration between thermal load and refrigeration model takes place at the cabin space as seen in Figure 3.20.

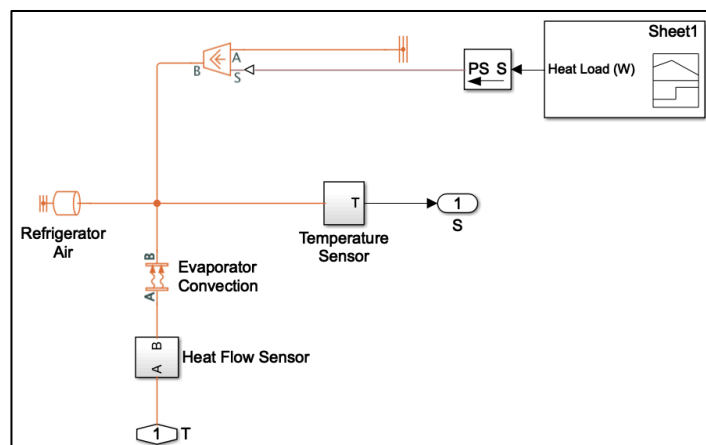


Figure 3.20: Cabin Space Subsystem

The cabin space subsystem models the convection that occurs in the cabin space. Modification has made to the MatLab® refrigeration circuit template in order

to integrate the results from the thermal load model into the refrigeration system. The results from the thermal load model has to be tabulated into a Microsoft® Office Excel file before it can be imported and read by the Signal Builder block located in the top right corner of Figure 3.20. Thermal load signal from the Signal Builder block is converted to Physical Signal type using an SPS converter, after which it is introduced into the cabin space through Controlled Heat Flow Rate Source (CHFERS) block. CHFERS block signifies an ideal heat source that maintains a controlled heat flow irrespective of the temperature difference between the two points. The heat flows from this block to the evaporator via PMC port 1T after passing through the convective heat transfer block and heat flow sensor. The convective heat transfer block represents the convection occurring in the cabin space, while the heat flow sensor measures and reports the amount of heat flowing to the evaporator. The thermal mass, denoted as Refrigerator Air represents the internal energy storage of this heat network, where it is governed by the mass and specific heat of air in the cabin space. Furthermore, the temperature in the cabin space is measured and reported by the temperature sensor to the refrigeration cycle control circuit via PMC port 1S.

3.3.4 Phase 4: Construction of Experimental Model

The experimental model is similar to the EV refrigeration model as mentioned in Phase 2 in terms of component arrangement, as both are systems are based on the two-phase fluid refrigeration cycle running on R-134a refrigerant. The primary differences between the two models are the refrigeration circuit parameters as both systems have their own distinct dimension and operating range, as well as the thermal load input in the refrigerated space due to the difference in the heat introduction and profile. The dimension and operating range of the experimental model is based on G.U.N.T Hamburg ET400 Refrigeration Circuit that has the capability of varying the thermal load. The thermal input to the experimental model is shown in Figure 3.21. The parameters and respective values that have to be changed in the experimental model are listed in Table 3.9.

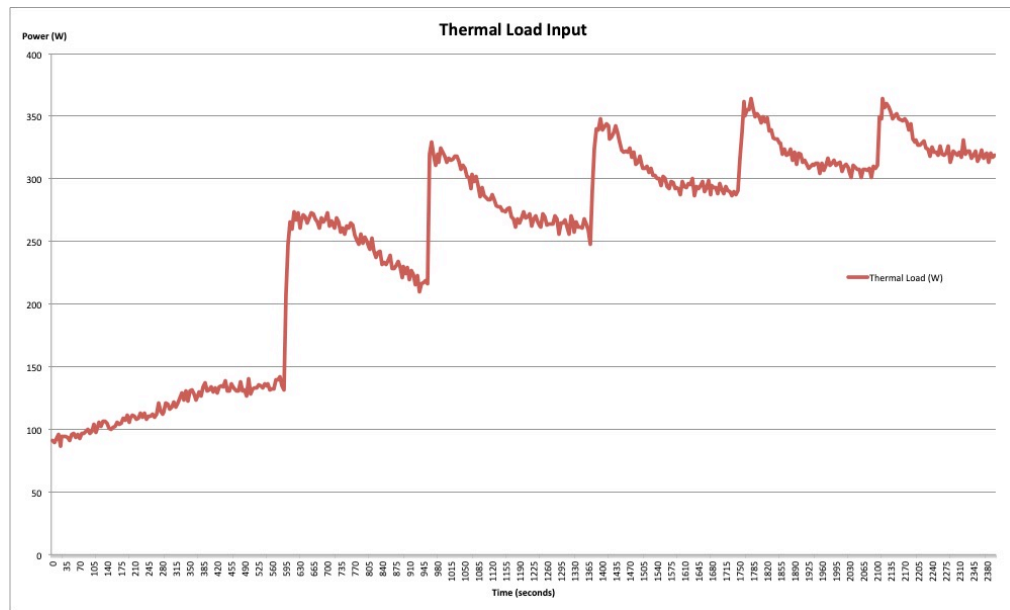


Figure 3.21: Thermal Load Input to Experimental Model

Table 3.9: Parameters Adjustment for G.U.N.T Hamburg ET400 Refrigeration Circuit

Parameter	Values	Units
Commanded Mass Flow	0.006	Kg /s
Condenser Length	5.5	m
Evaporator Length	3	m
Exterior Surface Area	6	m ²
Interior Surface Area	4.5	m ²
Maximum Throat Area	2.8	mm ²
Maximum Throat Temperature	255	K
Minimum Throat Area	0.75	mm ²
Minimum Throat Temperature	280	K
Pipe Diameter	0.012	m
Targeted Temperature	280	K

3.4 Validation with Experimental Result

Validation of theoretical modelling is important in order to verify the accuracy and viability of the formed model. One of the most popular methods to validate a modelling performed through software is to compare its produced data against a real life experiment. The thermal load model and the EV refrigeration circuit model are independently validated using experimental results.

The obtained results from the thermal load modelling in this research is compared against the results published by Aisling Doyle in her PhD thesis, titled The Development of A Numerical Temperature Algorithm To Predict The Indoor Temperature of An Electric Vehicle's Cabin Space. In order to preserve the precision and accuracy of the theoretical modelling, the input data and parameters between the theoretical model and experimental study must be similar. Any information in doubt should be intelligently approximated to the closest experimental condition. Comparison will be made between the results and a discussion performed on the outcome to address any similarities and discrepancies alike.

The EV refrigeration circuit model is validated through replication of the G.U.N.T Hamburg ET 400 refrigeration cycle in Simulink® environment. The replication process has been discussed in Phase 4 via the construction and simulation of the experimental model. An actual experiment is then conducted using the actual refrigeration cycle, as depicted in Figure 3.22, where the operating parameters are logged into a computer connected to the refrigeration circuit. The results from the model and actual experiment will be compared and discussed in order to validate the accuracy of the refrigeration model.



Figure 3.22: G.U.N.T Hamburg ET 400 Refrigeration Circuit

3.5 Expansion on Simulation Model

3.5.1 Expansion on Refrigeration Circuit Model

The validated model can be further expanded in order to analyse different types on thermal load on the vehicle. Heat generation from the battery during EV's operation is a type of thermal load that is unique to this niche of transportation. The components and their arrangement in the refrigeration circuit remains the same for this expansion work, where the only difference is the thermal load profile that has to be inputted to the "Signal Builder" block in the cabin space. The heat generated by the battery varies with different driving pattern, therefore various profile of thermal load may be inputted to the "Signal Builder" in order to study the response of the refrigeration circuit. In this expansion work, three types of driving pattern will be studied, namely Urban Dynamometer Driving Schedule (UDDS), Highway Fuel Economy Driving Schedule (HWFET) and US06 driving cycle. These three driving cycles are designed by the United States Environmental Protection Agency in order to replicate different vehicle driving patterns. UDDS is designed to represent driving in the city, especially for light duty vehicle, where the test spans 1369 seconds, covering 7.45 miles averaging at speed of 19.59 mph. HWFET represents driving on the highway under speed of 60 mph, timed for 765 seconds, covering a distance of 10.26 miles at an average speed of 48.3 mph. The US06 driving cycle is used to replicate high acceleration, aggressive driving pattern with a sample period of 596 seconds, for 8.01 miles, averaging at speed of 48.37 mph (USEPA, 2017).

3.5.2 Expansion on Thermal Load Model

The primary thermal load profile acting on a vehicle, especially solar and ambient heat load can also be applied to a cabin temperature-predicting algorithm. This algorithm functions to predict the changes in the cabin temperature due to the introduction of heat from the sun and difference in cabin and outdoor temperature. The temperature predicting algorithm can be modelled in Simulink® environment as shown in Figure 3.23, using various mathematical blocks from the library. The variable in this model consists of the solar thermal load, interior and exterior temperature, which are representatives of the solar and ambient thermal load. This algorithm may also be applied to different type of vehicles provided the parameters such as the area and specific heat of the cabin space, as well as mass and thermal

conductivity of the vehicle are known. The changes in cabin space temperature can then be simulated and observed using the “Scope” block.

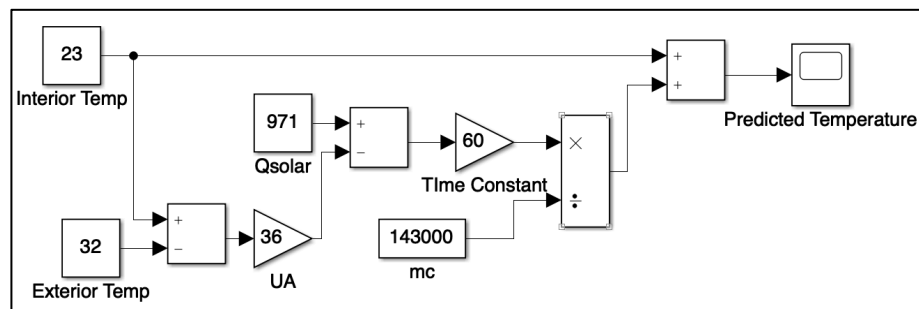


Figure 3.23: Cabin Temperature Predicting Algorithm Model

3.5.3 Supporting Infrastructure for Cabin Cooling

There are two types of supporting infrastructure, the namely the passive and active infrastructure.

The passive cooling infrastructure is the installation of triple glazing on the windows in order to reduce the solar irradiance transmittance into the cabin space. This is modelled by changing the values of the window transmittance value in the “Constant” block in the solar thermal load model.

The active cooling infrastructure is the use of two 21 W extractor fans. The equation for the cooling capacity of the two 21 W extractor fans can be constructed using simple mathematical blocks as shown in Figure 3.24. Meanwhile the equation used to predict the cabin temperature changes due to solar and ambient heat load, as well as the extractor fan cooling capacity is modified from the model in Figure 3.23. The modified model is shown in Figure 3.24. It is worth noting that the interior temperature for extractor fan cooling model is the maximum or saturated temperature after the cabin space has been “soaked in” under the sun. Meanwhile, the extractor fan-cooling load in the modified cabin temperature-predicting model is the value obtained from the extractor fan-cooling model, which is modelled using a “Constant” block.

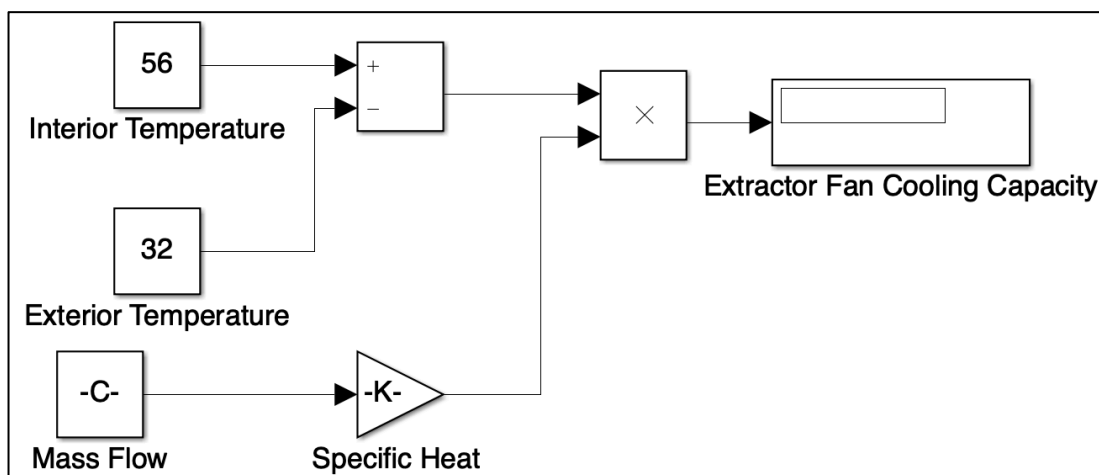


Figure 3.24: Extractor Fan Cooling Model

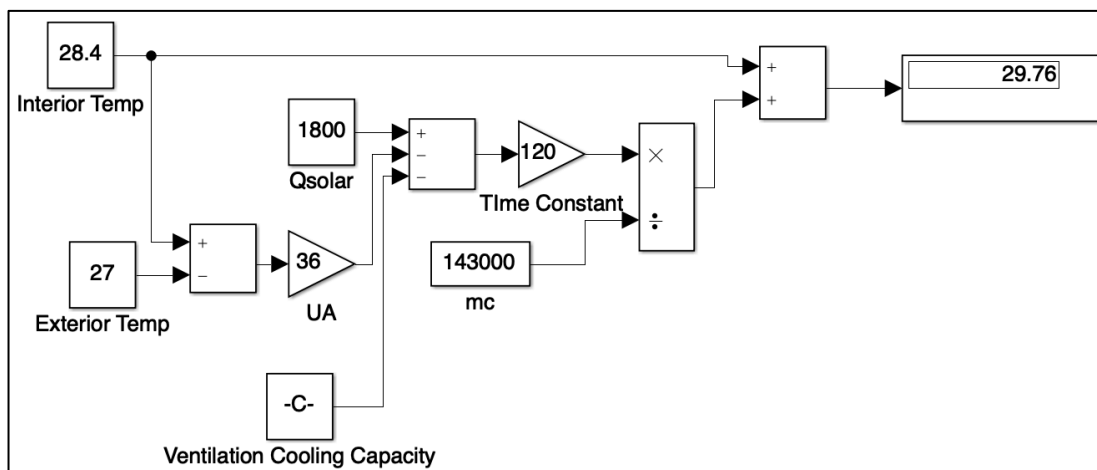


Figure 3.25: Modified Cabin Temperature Predicting Model

3.6 Summary

Initially, the methodology states the research flow chart, which lists down the steps to adhere to during the course of this research. Subsequently, the thermal load calculation is explained in depth along with the formula and input parametric value required. The thermal load approach is modified and amended to suit the operation of an EV, where these modifications are duly justified. The simulation software selected is MATLAB®/SIMULINK® due to its simplicity, popularity and low in computing power requirement. A brief description of the operation of SIMULINK® was also described, where basic mathematical functions are deployed to represent mathematical formula and equations. Validation of thermal load simulation result is performed through comparison with experimental results based on Aisling Doyle's thesis, with any similarities and discrepancies addressed in the discussion section.

Furthermore, comparing the modelled result with the actual experimental response validates the accuracy of the refrigeration circuit. Lastly, the refrigeration circuit modelled can be expanded and applied to understand the response the refrigeration cycle to different driving cycle. The thermal load model can also be further expanded to predict the cabin temperature using a cabin temperature-predicting algorithm.

CHAPTER 4

RESULTS AND DISCUSSION

4.1 Introduction

The results and discussion in this chapter will be segregated into four major parts, namely thermal load modelling, refrigeration circuit modelling, verification test and expansion on current model. The expansion in current model includes the expansion of thermal load model via cabin temperature prediction, expansion of refrigeration model via application to three different driving cycles and the expansion of models to the supporting infrastructure of cabin cooling. The results will be graphically presented for ease of comprehension and discussion will cover the inputs, output response, and justification on the behaviour of the model.

4.2 Thermal Load Modelling

The first stage of modelling is the thermal load modelling, where the equations governing all the thermal loads in the HBM are modelled and constructed using basic mathematical function. The purpose of this modelling is to represent the governing equations in SIMULINK®, so that an overall thermal load imposed on the EV's cabin can be found.

4.2.1 Metabolic Thermal Load

In this modelling, it is assumed the driver is always present, and the passenger's number is varied from zero to four passengers. The result of metabolic thermal load modelling with passengers varied from zero to four is shown in Table 4.1 and Figure 4.1.

Table 4.1: Metabolic Thermal Load of Occupants (in W)

Number of Passengers	Metabolic Thermal Load, W
0	163.7
1	269.6
2	375.5
3	481.4
4	587.3

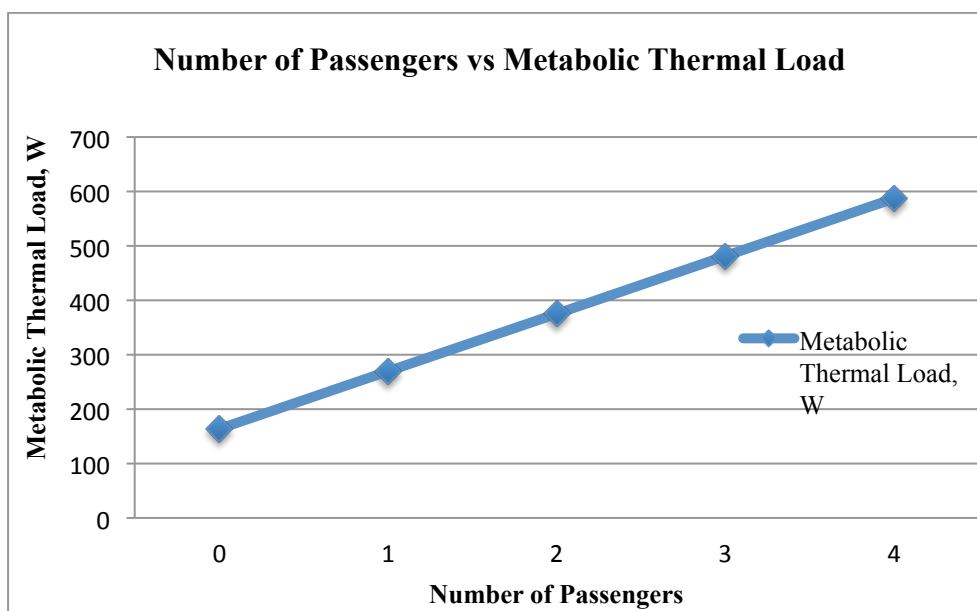


Figure 4.1: Metabolic Thermal Load

The result shows an initial metabolic thermal load of 163.7 W with no passengers, as this is due to the heat emitted by the driver that is assumed to always be present. The metabolic thermal load is seen to increase in a linear trend when the number of passenger is varied to its minimum to maximum. Each increment of passenger saw an increase in metabolic thermal load of 105.9 W. This linear trend is justified by the nature of the governing equation that increases linearly with every increment of number of passengers. The maximum amount of passenger is restricted at four due to the maximum legal passenger capacity in a small sized sedan car, thus the maximum metabolic thermal load for this vehicle size is 597.3 W. However, this model is useful to be expanded into other modes of transportation, such as busses and trains where the large number of passenger plays a significant role in the cabin space heat generation.

4.2.2 Ambient Thermal Load

The variables for ambient thermal load are the cabin space interior and exterior temperature. The cabin temperature is set at thermal comfort temperature of 23 °C, which is the temperature that the cabin space maintains. The ambient temperature is varied between 15 °C to 40 °C at 1 °C increment, representing the possible climate temperature changes over the year in Malaysia. The result from ambient thermal load modelling is graphically presented in Figure 4.2.

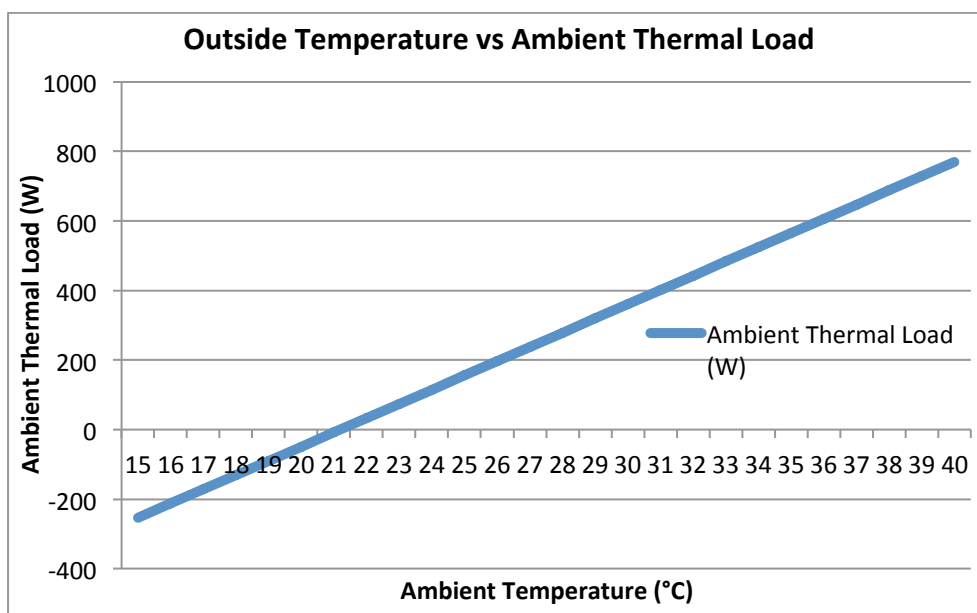


Figure 4.2: Ambient Thermal Load

From simple calculation, it can be seen that at every increment of 1 °C, the ambient thermal load increases by 40.9 W, and the maximum ambient thermal load is 769.4 W with the ambient temperature of 40 °C and cabin temperature at a constant 23 °C. The minimum thermal load is -253.4 W at 15 °C. The overall trend of the ambient thermal load is linear, therefore consistent with the proportionate nature of the governing equation. It can be seen that at lower temperatures, the ambient thermal load is in the negative region, but subsequently enters into the positive region as the temperature increases. The polarity of the thermal load is indicative of the direction of heat flow. A positive thermal load assumes the heat flows from the ambient environment into the space, whereas a negative thermal load assumes the heat flows from the cabin space to the ambient environment. At lower ambient temperature, the heat flows from the cabin space and to the ambient environment, and the otherwise applies. This data is therefore consistent with the Second Law of Thermodynamics, which implies that the heat flows from a region with higher temperature to a region with lower temperature.

4.2.3 Ventilation Thermal Load

The ventilation thermal load model has the same type of input parameters as the ambient thermal load. The governing parameters in this thermal load are cabin temperature that is set at thermal comfort temperature of 23 °C and ambient

temperature, which is varied between 15 °C to 40 °C at 1 °C increment, representing the possible range of temperature in Malaysia. The result from ventilation thermal load modelling is depicted in Figure 4.3.

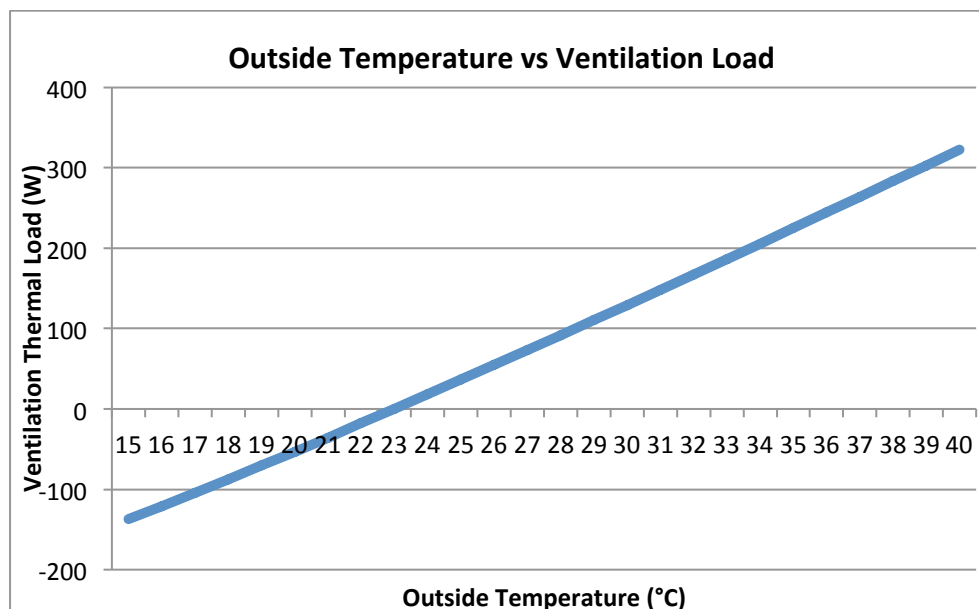


Figure 4.3: Ventilation Thermal Load

Based on the raw data, the ventilation thermal load increases by an average of 18.29 W with every increment of 1 °C, when the ambient temperature is varied from 15 °C to 40 °C. The minimum ventilation thermal load is -137.2 W at 15 °C and the maximum is capped at 322.5 W at 40 °C. The ventilation thermal load increases linearly with the varied outside temperature, which is consistent with the governing equation that suggests a linear relationship between the manipulated and responding variable. Similarly to the ambient thermal load, at lower temperatures, the ventilation thermal load exhibits a negative value, signifying that the direction of heat transfer is from the cabin space to the external environment. As the temperature passes the cabin temperature, the thermal load increases in the positive direction, thus complying with the Second Law of Thermodynamics. In the case of ventilation load, the governing equation deals with enthalpies, where in this model, the same temperature will result in the same enthalpies as the pressure is assumed to be the same at atmospheric pressure for both the interior and exterior of the vehicle, thus resulting in zero ventilation thermal load when the ambient temperature is the same as the cabin temperature.

4.2.4 Battery Thermal Load

Although the amount of heat released by the battery pack is dependent upon usage during charging and discharging, it is fixed to be constant at 0.1 W per cell. The total battery thermal load is calculated to be 126 W for the 1260 cells battery pack, where this heat is assumed to be penetrating into the cabin space due to insufficient or worn out thermal insulation foam.

4.2.5 Solar Thermal Load for Edinburgh, Scotland

The solar thermal load contributes to the overall heat generation of the cabin only in daytime when the sun is out, therefore it is imperative to analyse this thermal load in the time domain. Based on solar geometry, solar irradiance on mid day typically plays a significant part in heat generation in a cabin space, thus this time period will be used to simulate the solar thermal load in order to give a representation of the top extreme of the solar irradiance. This is supported by information from United States Office of Energy Efficiency and Renewable Energy, which states that the solar irradiance received on ground is the highest when the sun is directly overhead, as they are less slanted, thus contributing to less scatter and diffusion of the solar energy. The time period that will be considered for simulation is between 10:45 am to 2:00 pm. The solar thermal model will be initially simulated to replicate the experimental conducted by Aisling Dyle in order to verify the validity of the model and the input to the model is listed in Table 4.2. The solar thermal model will then be applied to a localised vehicle; in this case, Kuala Lumpur will be the designated location.

Table 4.2: Input to Solar Thermal Load Model for Edinburgh, Scotland

Parameters	Values
Hour	10 to 14
Minute	0 to 60
Seconds	0 to 60
Day	14 th
Month	March
Year	2016
Day Number	74
Latitude	55.95 °N
Longitude	3.19 °W
Aspect	212 °
Global Horizontal Irradiation	1.030 kWh/m ²

Based on the input in Table 4.2, a solar thermal load response based on time is generated from 10:45 am to 2:00 pm, as shown in Figure 4.4. The graph in Figure 4.4 shows the amount of solar thermal load that would be introduced into a Renault Zoe EV at a specific time of a day, in the mid day range. The graph is presented in increments of five minutes for comprehension of how this thermal load changes with time.

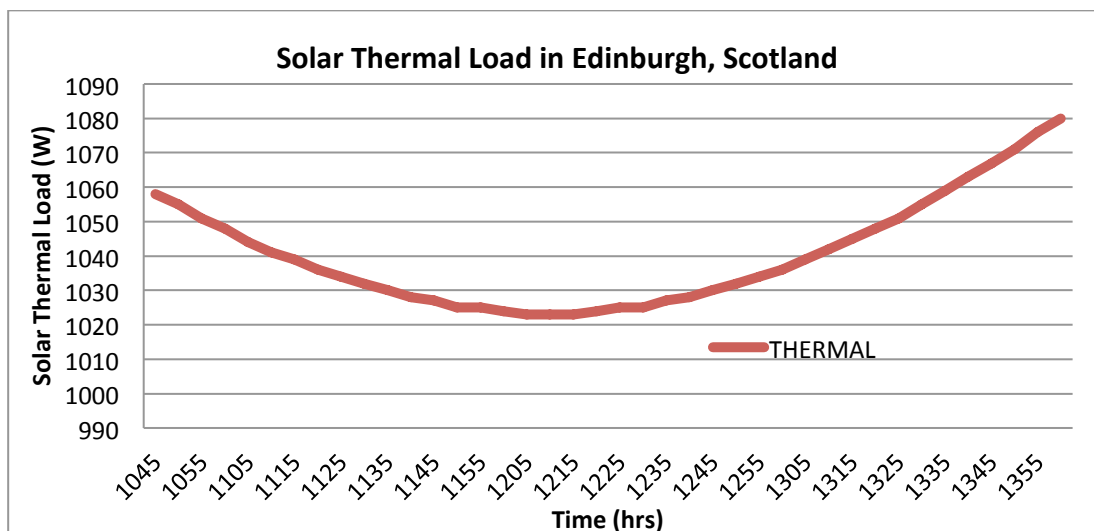


Figure 4.4: Solar Thermal Load in Time Domain in Edinburgh, Scotland

The trend line in Figure 4.4 shows that the solar irradiance decreases before noon and bottoms out between 12:10 pm to 12.15 pm, which can be classified as midday. The solar load then increases after noon and capped out at around 2.00 pm. The solar thermal load is observed to be declining at an average rate of 2.19 W every five minutes from 10:45 am to 12:05 pm, and seen to be increasing at an average rate of 2.48 W per five minutes from 12:10 pm to 2:00 pm. The minimum thermal load is observed to be at 12:10 pm with value of 1023 W and the maximum is at 2:00 pm with a thermal load of 1080 W. Initially this data is counter intuitive, as the general perception is that solar irradiance should be highest at noon, however the angle of solar irradiance is not only governed by the time of day, but also the latitude of the location of observation. Edinburgh, Scotland is located at 55.95 °N, signifying that it is located higher up in the globe further from the Equatorial Line, somewhere in the Northern Hemisphere. Therefore, this affects the sunray's angle on the location of interest, thus resulting in a lower solar irradiance during noon and a higher irradiance later in the day.

Based on the experiment conducted by Aisling Doyle in calculating the amount of solar irradiance received from the same time, it was concluded that an average of 971 W of solar irradiance was introduced into a Renault Zoe EV during the specific time duration. Based on the calculation from the results of this solar model, the average solar irradiance for the same time period is 1040.58 W. In comparison, a percentage error of 7.17 % is found between this solar model and the experiment conducted by Aisling Doyle. Albeit having an error of 7.17 %, the error is considered acceptable and justifiable, as a number of reasonable assumptions have been made in this simulation. The longitudinal and latitudinal coordinates used in this model are an approximation of the Edinburgh's location, whereas the experiment may use a more accurate coordinates. Furthermore, the global horizontal irradiance used in the experiment is measured using a pyrometer at the specific time of interest, whereas the global horizontal irradiance data used in the model's simulation is obtained from Edinburgh's local meteorology station that published the day's average global horizontal irradiance. The governing equations used in the experiment is specific to conditions in the Northern Hemisphere, while the governing equations used in the simulation model can be applied to any location on the globe, but having a drawback on the result's precision. Both these factors contributed to the reasonable amount of percentage error, however it can be implied that the simulation model is capable of producing a satisfactory approximation.

4.2.6 Solar Thermal Load for Kuala Lumpur, Malaysia

As the solar thermal model produces a satisfactory result with an acceptable level of percentage error, it can be further expanded to simulate the solar irradiance in other locations, in this case, Kuala Lumpur. The input data for simulation of solar irradiance in Kuala Lumpur is listed in Table 4.3.

Table 4.3: Input to Solar Thermal Load Model for Kuala Lumpur, Malaysia

Parameters	Values
Hour	10 to 14
Minute	0 to 60
Seconds	0 to 60
Day	14 th
Month	March
Year	2016
Day Number	74
Latitude	3.14 °N
Longitude	101.69 °W
Aspect	212 °
Global Horizontal Irradiation	2 kWh/m ²

Based on the input in Table 4.3, a simulation of the model is ran in order to ascertain the solar irradiance on a Renault Zoe EV between 10:45 am to 2:00 pm based on a five minutes increment. The parameters of time, day, date and aspect are unchanged in order to study the effects of varying the location on the solar irradiance on the same vehicle. The coordinate is changed to reflect its current position in Kuala Lumpur, Malaysia, as well as the change associated to the global horizontal irradiation. The result from the thermal model simulation is shown in Figure 4.5.

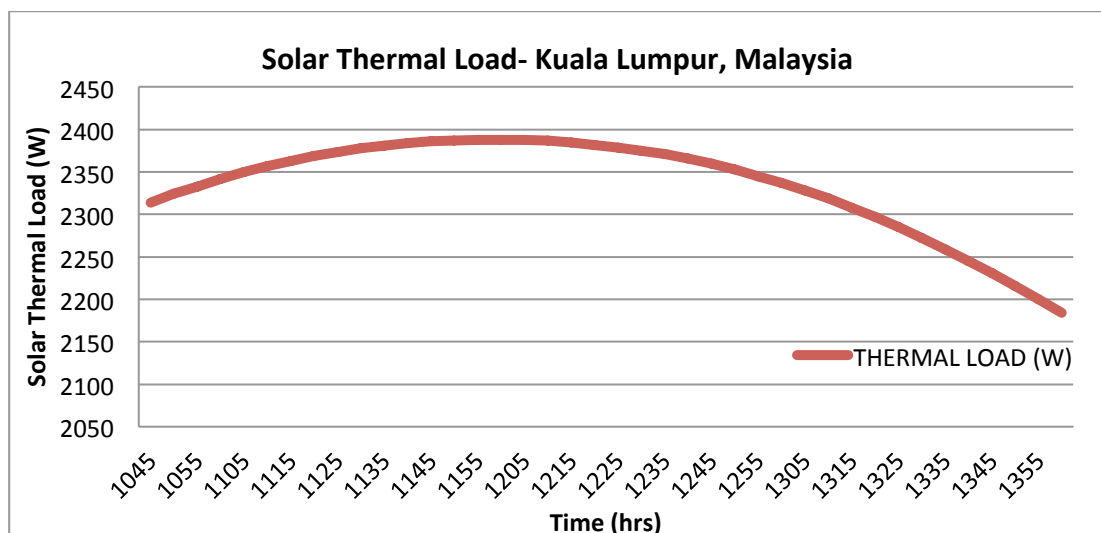


Figure 4.5: Solar Thermal Load in Time Domain in Edinburgh, Scotland

Based on the trend line in Figure 4.5, it can be observed that the solar irradiance increases from the morning and peaks between 12 noon to 12:05 pm. The solar irradiance subsequently decreases past noon. The solar thermal load is observed

to be increasing at an average rate of 5.29 W every five minutes from 10:45 am to 12 noon, and seen to be declining at an average rate of 8.87 W per five minutes from 12:05 pm to 2:00 pm. The minimum thermal load is observed to be at 2 pm with value of 2184 W and the maximum is at 12 noon to 12.05 pm with a thermal load of 2388 W. This trend line is intuitive to daily subjective observation, especially those in tropical countries, where the population often perceive noon as the time of the day to be the hottest. The data and subjective observation is supported by the fact that Kuala Lumpur is located near the Equatorial line, where the solar irradiance is the highest. Furthermore, the solar irradiance is highest in noon due to the overhead position of the sun, forming an angle of almost 90° from the horizon, therefore causing less slant on the sunray, resulting in less solar irradiance scatter and diffusion. These factors translate into a higher solar irradiance on a reference surface of observation.

Another difference that can be noted about the solar irradiance between Edinburgh and Kuala Lumpur is the magnitude of solar irradiance, where it can be seen that the solar irradiance is almost double of that in Edinburgh. This is large justified by the higher value of global horizontal irradiation in Kuala Lumpur, which has a value of 2 kWh/m^2 that is two times as compared to Edinburgh. The global horizontal irradiation in Kuala Lumpur is obtained from the daily average global horizontal irradiation data archived and published by the local meteorology station. Annually, the average global horizontal irradiation near the equatorial line is higher than those located further away from it, due to the greater amount of solar irradiation received relative to a horizontal surface on earth as a result of the orientation of the earth relative position to the sun that causes a more oblique angle of the sun's ray relative to locations further away from the equatorial line.

4.2.7 Combined Thermal Load

The individual thermal loads have been discussed and elaborated, along with their manipulating variables. Therefore, a combined thermal load can be computed based on conditions imposed on each individual thermal loads, where the combined thermal load is merely the summation of each thermal load.

As an illustration, two types of case are depicted in Table 4.4 and Table 4.5 respectively to illustrate the combined thermal loads on a Renault Zoe EV in Edinburgh and Kuala Lumpur respectively.

Table 4.4: Combined Thermal Load Model for Edinburgh, Scotland

Parameters	Values
Presence of Driver	Yes
Number of Passenger	2
Desired Cabin Temperature	23 °C
Ambient Temperature	27 °C
Date	14 th March 2016
Time of Day	10:45 am
Location	Edinburgh, Scotland
Aspect of Vehicle	212 °
Combined Thermal Load	1880.14 W

Table 4.5: Combined Thermal Load Model for Kuala Lumpur, Malaysia

Parameters	Values
Presence of Driver	Yes
Number of Passenger	2
Desired Cabin Temperature	23 °C
Ambient Temperature	27 °C
Date	14 th March 2016
Time of Day	10:45 am
Location	Kuala Lumpur, Malaysia
Aspect of Vehicle	212 °
Combined Thermal Load	3136.14 W

In both cases, the thermal load models can be used to approximate the combined thermal load acting on a vehicle through the summation of the individual thermal loads, with conditions imposed as shown in Table 4.4 and Table 4.5. In Kuala Lumpur, the thermal load is calculated to be 3136.14 W as opposed to 1880.14 W in Edinburgh, where the former location is shown have 40.05 % thermal load introduced into a vehicle of interest. The results from this combined thermal load model is meant to be a sample to illustrate its applicability. The combined thermal load can also be used to calculate instantaneous thermal loads with carrying number of passengers, desired cabin temperature, ambient temperature, day, time of day, location, and aspect of vehicles.

4.3 Refrigeration Model Response

The individual thermal load is introduced to the refrigeration model as thermal input, after which simulation will be performed for certain duration of time, dependent on the type of solar input. The response from the refrigeration model will be presented

and discussed, including compressor pressures, compartment heat extracted, compressor pressure ratio, and compressor power. The thermal loads simulated include human metabolic, ambient, ventilation, battery and solar thermal load. It is worth noting that the compressor power discussed below refers to the instantaneous power consumption, however total power consumption during simulation period can be calculated by integrating the area under the line in the compressor power graph.

4.3.1 Human Metabolic Thermal Load

The simulation duration for this thermal load is 5000 seconds, with a driver added into the system at 1000 seconds and a passenger every subsequent 1000 seconds. The refrigerant circuit response including compressor pressures, compressor pressure ratio, cabin heat extracted and compressor power for this thermal load is shown in Figure 4.6 to Figure 4.9.

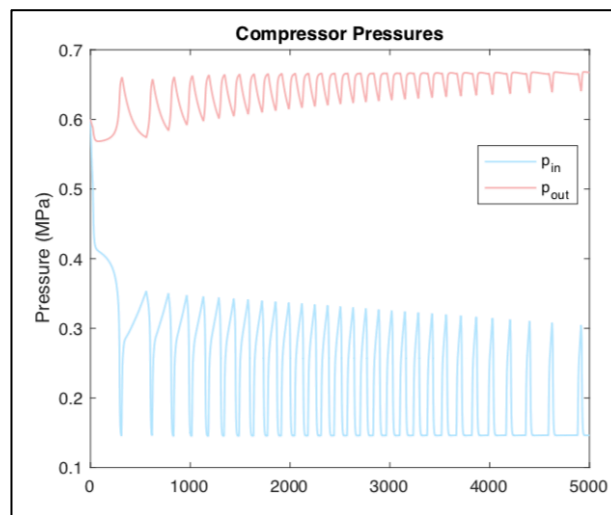


Figure 4.6: Metabolic Load Compressor Pressures

Based on Figure 4.6, during the compressor activation period, the compressor inlet pressure averages at 0.14 MPa, and the compressor outlet pressure averages at 0.65 MPa, which produces an average compressor pressure ratio of approximately 4.5 as seen in Figure 4.7.

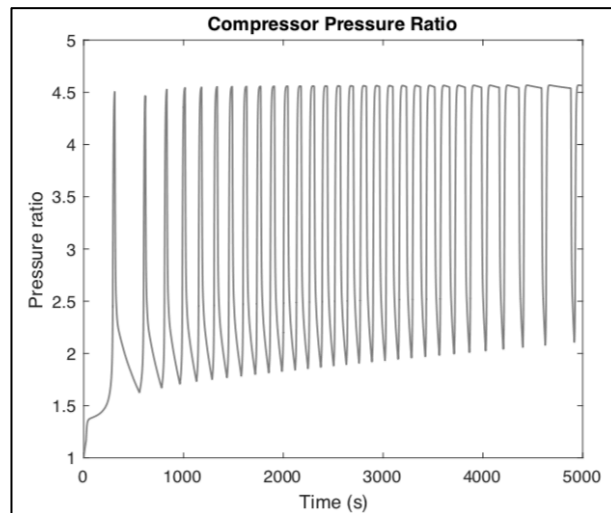


Figure 4.7: Metabolic Load Compressor Pressure Ratio

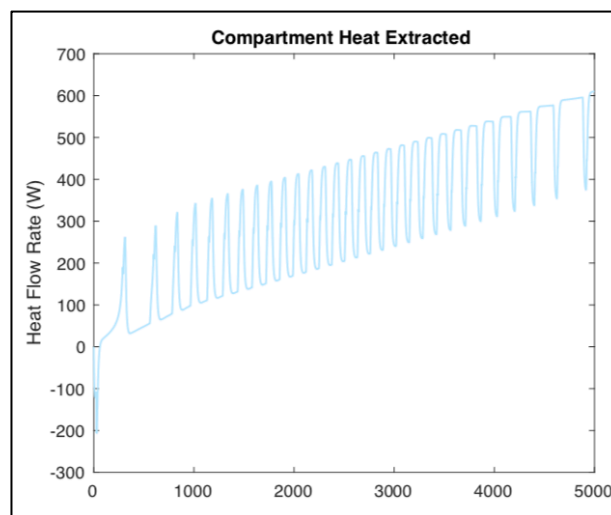


Figure 4.8: Compartment Load Heat Extracted

As the compressor is activated, the heat in the cabin space is extracted, where the initial heat extracted at the first peak or activation period is 255 W. The amount of heat extracted increases gradually as per the increment of thermal load, where at 5000 seconds of simulation, the peak amount of heat extracted from the cabin is approximately 600 W. The heat extracted is in agreement with the metabolic thermal load applied, where the peak thermal load is 597.3 W, thus the system has the ability to extract the same amount of heat that is supplied to the cabin space.

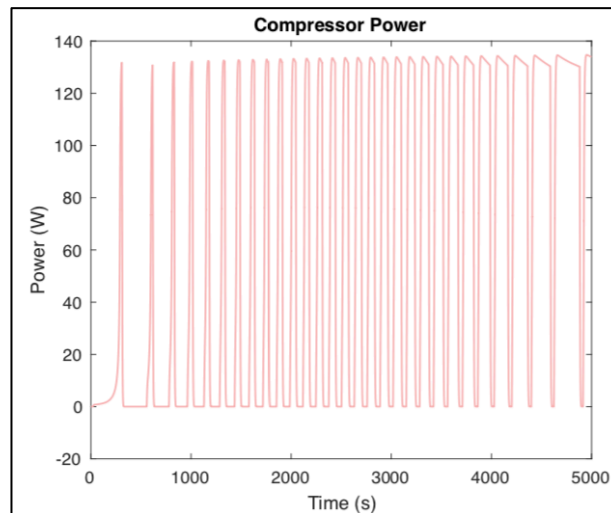


Figure 4.9: Metabolic Load Compressor Power

Furthermore, upon inspection of the data in Figure 4.9, it can be seen that during the activation period, the compressor consumes an average power of approximately 130 W in order to extract the heat supplied to the cabin space.

The first parameter to discuss is the compartment heat extracted, where it can be seen that the response line trends upwards with fluctuations in the signal. The upward trend corroborate with the increasing metabolic thermal load introduced into the system. Thus it can be seen that the refrigeration circuit is extracting more heat as an increasing amount of metabolic thermal load is added into it. The energy consumption of compressor follows the same fluctuation as the heat extracted from the compartment. The fluctuation can be explained by the operational nature of this refrigeration system, where the system is triggered on when a certain threshold of heat is introduced into the cabin, and subsequently triggered off when the heat in the cabin drops below a certain amount, where the cabin space is allowed to heat up by virtue of the thermal load to the targeted cabin temperature. These thresholds form a range of operational temperature that the actual cabin temperature is allowed to fluctuate. This system is commonly used in refrigeration cycle in order to reduce or eliminate the compressor power consumption when the refrigerated space reaches its target temperature. This phenomenon can be classified as hunting, as the system continuously attempts to lock in at the cabin target temperature, causing the system to fluctuate above and below its target. Another profile to note in these two signals is the peak duration, also known as the amount of time when the system is switched on. At lower cabin heat level, the system is switched on and off for shorter duration, as

indicated by a sharp peak of the compressor power. However, as the amount of heat introduced into the cabin space increases, the peak gradually become flatter, as seen at in the later stage of the simulation period. A flatter peak of power consumption indicates the system is running for a longer time period, thus extracting more heat at the later stage of the simulation period, where greater amount of heat is introduced into the cabin space. The compression ratio, compressor inlet and outlet pressure are well within the operating limits of the compressor. The inlet and outlet compressor pressure exhibits the same fluctuation, explainable by the same reasoning. It can be seen that the compressor outlet pressure's fluctuation decreases at the later stage of simulation, signifying the continuous working of compressor in order to maintain an increase pressure of the compressor in order to reduce the increased amount of heat in the space. Another important refrigeration cycle response profile to observe is the changes in cabin temperature, which is shown in Figure 4.10.

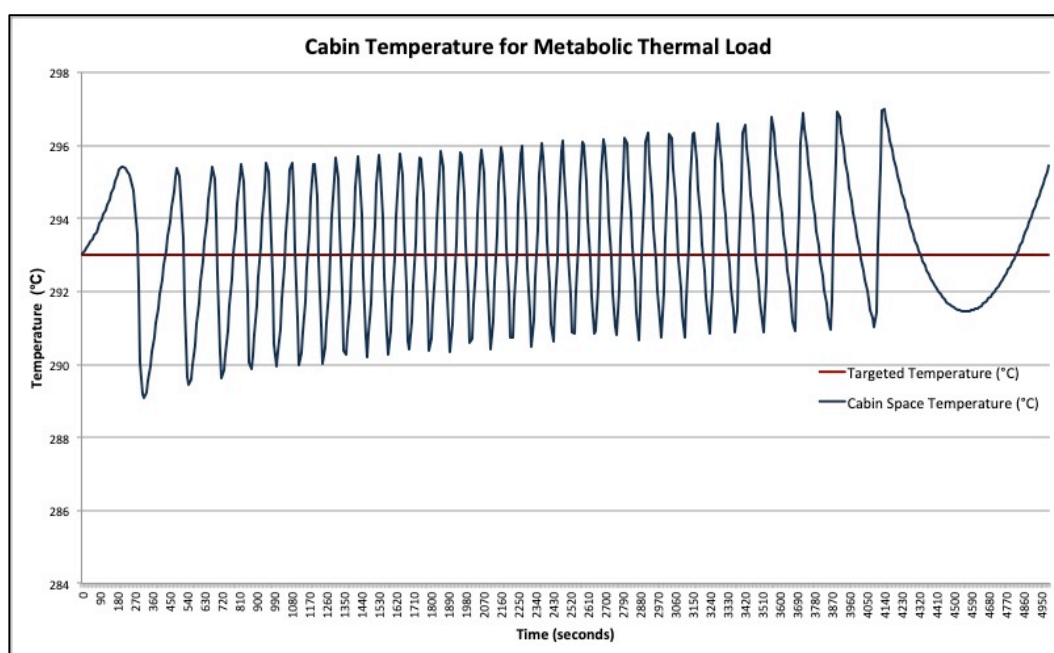


Figure 4.10: Cabin Temperature Profile for Metabolic Thermal Load

The red line in Figure 4.10 represents the constant cabin target temperature of 20 °C, which is also the human thermal comfort temperature, whereas the blue line represents the real time changes in cabin temperature during simulation. The maximum of temperature deviation after the system is activated is at 4150 seconds with a 1.37 % deviation from targeted temperature. The same pattern of fluctuation appears in the cabin temperature profile, which can be explained by the operational

nature of the refrigeration system, as well as the compressor lag. Compressor lag occurs, as the compressor requires a certain amount of time before reaching the desired speed and pressure. At the initial stage of the simulation period, the cabin temperature increases for a longer duration before the temperature reaches the operational trigger point, resulting in the correction of the cabin temperature by powering up the compressor. As the signal progresses with the simulation, the cabin temperature appears to be gradually increasing. This is justified by the increment of thermal load in the cabin space, causing the cabin to heat up to a higher temperature.

4.3.2 Ambient Thermal Load

The simulation duration for this thermal load is 7500 seconds, where a 1 °C increment of ambient temperature occurs once every 300 seconds. The ambient temperature is assumed to be 15 °C initially and reaches 40 °C at the end of simulation. The responses of the refrigeration circuit are shown in Figure 4.11 to Figure 4.14.

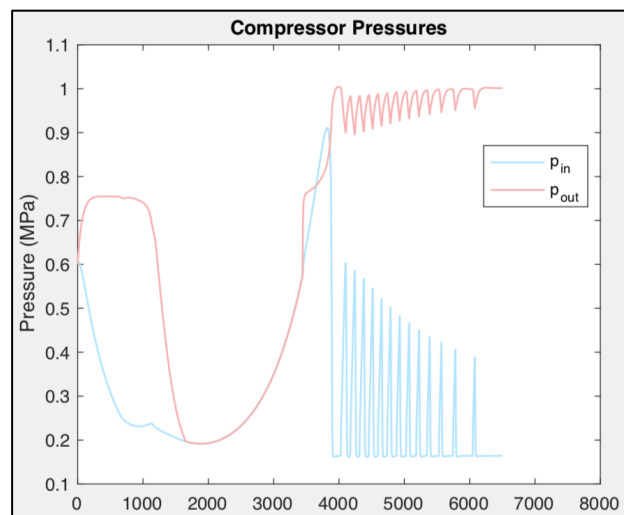


Figure 4.11: Ambient Load Compressor Pressures

Based on Figure 4.11, during the compressor activation period, the compressor inlet pressure averages at 0.16 MPa, and the compressor outlet pressure averages at 0.95 MPa, which produces an average compressor pressure ratio of approximately 6 as seen in Figure 4.12.

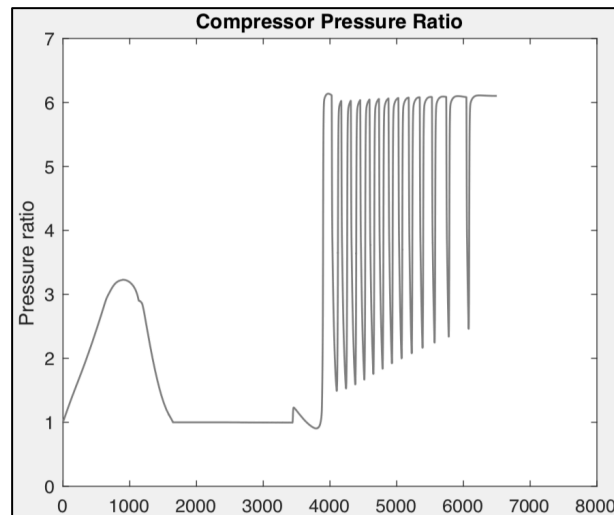


Figure 4.12: Ambient Load Compressor Pressure Ratio

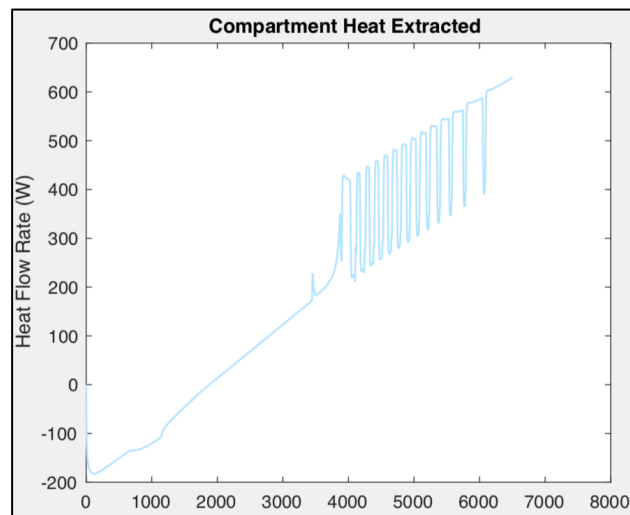


Figure 4.13: Ambient Load Compressor Pressure Ratio

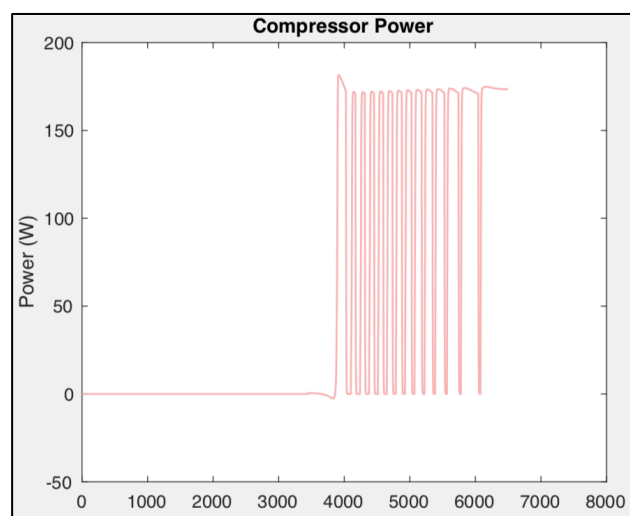


Figure 4.14: Ambient Load Compressor Power

As the compressor is activated, the heat in the cabin space is extracted, where the initial heat extracted at the first peak or activation period is 400 W. The amount of heat extracted increases gradually as per the increment of thermal load, where at 7500 seconds of simulation, the peak amount of heat extracted from the cabin is approximately 650 W. The maximum ambient thermal load introduced into the cabin space is 769.4 W, where the refrigeration circuit only manages to extract only 650 W, therefore the system is only able to extract 84.49 % of the heat introduced. It is projected that the refrigeration circuit is capable of extracting 100 % of the heat introduced if the model is allowed to run for an extended of time.

Furthermore, upon inspection of the data in Figure 4.14, it can be seen that during the activation period, the compressor consumes an average power of approximately 173 W in order to extract the heat supplied to the cabin space.

From the figures of ambient thermal load, all four graphs of the refrigeration circuit response exhibits two very different behaviour at the initial and later stage of simulation. In the initial stage, it can be infer that the refrigeration system is idle, indicated by zero compressor power up until approximately 3800 seconds. This idle phenomenon is justifiable, as negative thermal load is supplied to the cabin during this period. This indicates that the temperature in the cabin is higher than the ambient temperature, thus causing heat to flow from the cabin to its environment. As this is a cooling system that does not have heating capabilities, the system will always remain dormant as long as the temperature and heat inside the cabin is below the operational threshold. Initially, there is a difference in compressor inlet and outlet pressure, due to the residual/ initial pressure existing in the compressor, but the pressure eventually equalises, resulting in unity compression ratio.

Upon reaching the operational threshold, the system is switched on; causing heat to be extracted from the cabin, where the upward trend line indicates a linearly increasing amount of heat is extracted due to a proportionally increasing heat introduction into the cabin space. The compressor pressures, compression ratio, compartment heat extracted and compressor power have parameters within normal operational limits and all of them exhibits the same type of operating behaviour as found in the previous thermal load. This implies the consistency of operation of the model.

The changes in cabin temperature can be seen in Figure 4.15, where two very distinct characteristics can be observed, before and after the 3800 seconds mark. The maximum cabin temperature deviation after the system is activated is 4.19 % from the targeted temperature at 3760 seconds. In the early stages of simulation, it can be seen that the cabin temperature is well below the cabin target temperature due to cabin heat loss, as a result of a colder ambient environment. However, the cabin temperature floors out and eventually warm up by virtue of positive ambient thermal heat. Upon reaching the operational threshold, the system starts to extract heat from the cabin, resulting in the decline of cabin temperature. The actual cabin temperature then fluctuates, as the system attempts to lock onto the cabin temperature. The peaks of the line appear to be slightly increasing due to the greater amount of thermal heat that increases the cabin temperature to a higher value.

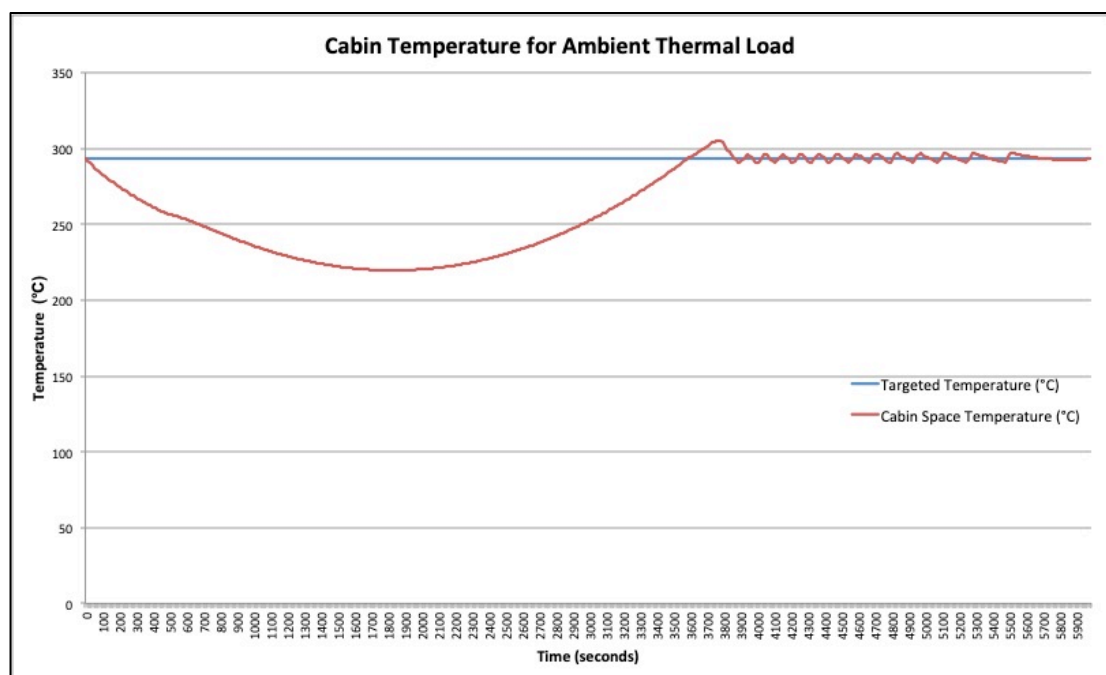


Figure 4.15: Cabin Temperature Profile for Ambient Thermal Load

4.3.3 Ventilation Thermal Load

The simulation duration for this thermal load is 2500 seconds, where a 1 °C increment of ambient temperature occurs once every 100 seconds. The ambient temperature is assumed to be 15 °C initially and reaches 40 °C at the end of simulation. The responses of the refrigeration circuit are shown in Figure 4.16 to Figure 4.19.

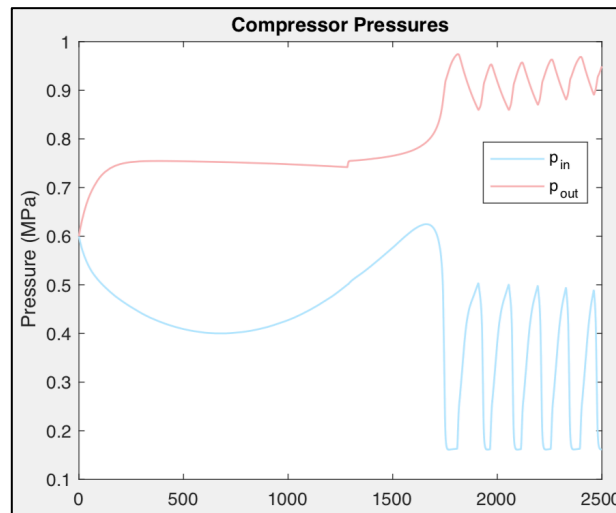


Figure 4.16: Ventilation Load Compressor Pressures

Based on Figure 4.16, during the compressor activation period, the compressor inlet pressure averages at 0.16 MPa, and the compressor outlet pressure averages at 0.94 MPa, which produces an average compressor pressure ratio of approximately 5.9 as seen in Figure 4.17.

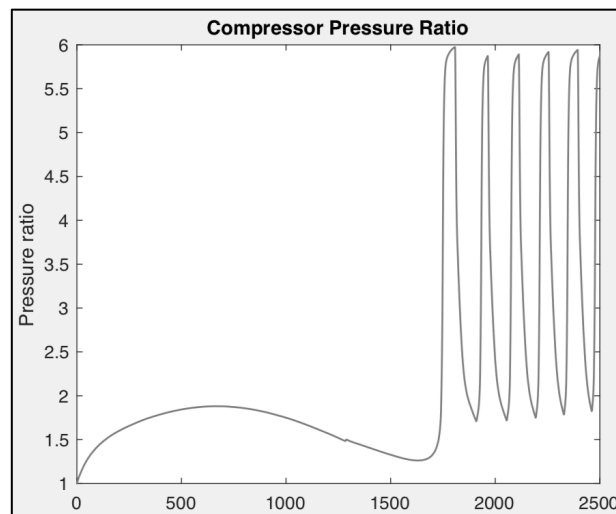


Figure 4.17: Ventilation Load Compressor Pressure Ratio

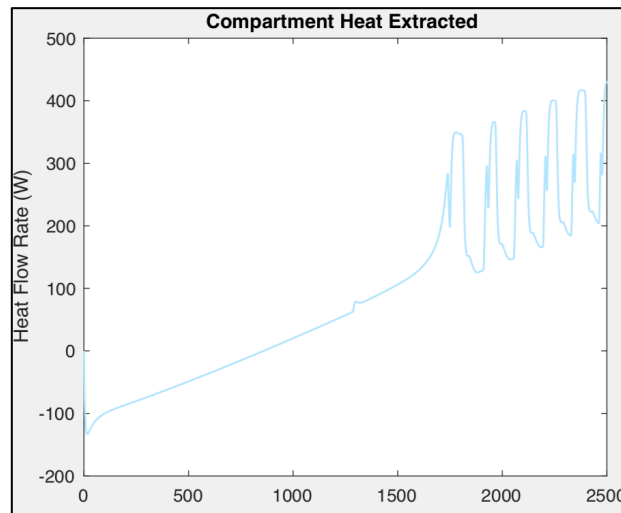


Figure 4.18: Ventilation Load Heat Extracted

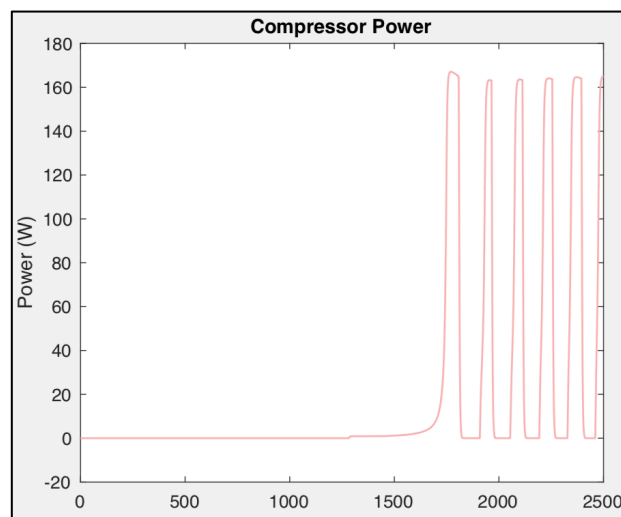


Figure 4.19: Ventilation Load Compressor Power

As the compressor is activated, the heat in the cabin space is extracted, where the initial heat extracted at the first peak or activation period is 340 W. The amount of heat extracted increases gradually as per the increment of thermal load, where at 2500 seconds of simulation, the peak amount of heat extracted from the cabin is approximately 400 W. The maximum ventilation thermal load introduced into the cabin space is 322.5 W, where the refrigeration circuit manages to extract 400 W, therefore the system extracts 24.03 % more than the heat introduced, thus the system has the ability to extract the heat that is supplied to the cabin space.

Furthermore, upon inspection of the data in Figure 4.19, it can be seen that during the activation period, the compressor consumes an average power of approximately 160 W in order to extract the heat supplied to the cabin space.

Upon observation of the above figures, it can be seen that the system response for ventilation thermal load is similar to the response for ambient thermal load, where the graphs exhibit two regions with different system behaviour. The earlier region shows relatively dormant system behaviour and the latter exhibits the operational state of the system. The same reasoning as the response in ambient thermal load causes these behaviours. The system is operational after approximately 1700 seconds. Before the system's operational period, the cabin has a lower temperature compared to its surrounding, thus heat flows from the cabin towards its environment, in pursuance of the Second Law of Thermodynamics, where at this stage the air inside the cabin has a higher enthalpy. After a certain amount of time, where the temperature in the ambient environment has risen above that of the cabin space, its enthalpy also rises accordingly, thus resulting in heat flow from the ambient environment to the cabin space. However, the refrigeration system is not activated immediately after the change of direction of heat flow, as the temperature in the cabin space rises for a while before the system is activated, as seen in Figure 4.20.

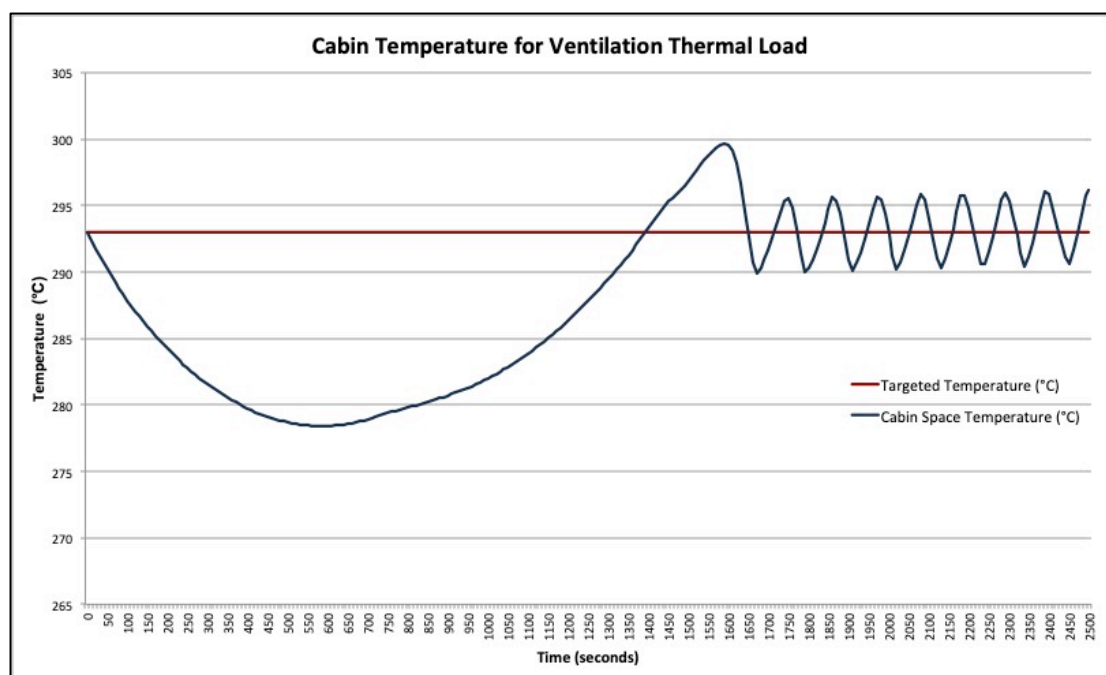


Figure 4.20: Cabin Temperature Profile for Ventilation Thermal Load

This phenomenon can be associated to the operational trigger threshold, where the system will be activated only after a certain amount of temperature threshold is reached. This operational trigger threshold forms a limit of temperature above the targeted cabin temperature; where the cabin space temperature is allowed fluctuating below the threshold without intervention from the refrigeration circuit. However, once this threshold is reached, the system will be in operating state. This is a common operating feature in machineries dealing with fluctuating signal, as it improves the energy consumption of the machine. Compressor lag also contributes to the total lag time of the machine, although this factor is less significant than the previous reasoning.

As seen in Figure 4.20, the temperature is allowed rise to a certain limit before the refrigeration system operates to bring the temperature down to the targeted value. The maximum cabin temperature deviation after the system is activated is 1.08 % from targeted temperature at 2500 seconds. The actual cabin temperature is allowed to fluctuate across the target temperature, with the peaks of the signal gradually increasing due to the increasing thermal load that causes the cabin to be heated to a higher temperature in the same duration of time.

4.3.4 Battery Thermal Load

The battery thermal load is assumed to be constant at 136 W, where the model is simulated for 3000 seconds in order to study the response of the refrigeration circuit and the subsequent actual cabin temperature profile. The refrigeration circuit responses for battery thermal load are depicted in Figure 4.21 to Figure 4.24.

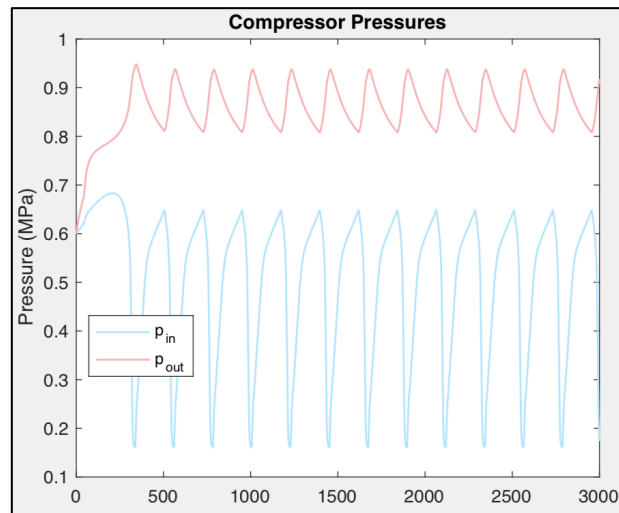


Figure 4.21: Battery Load Compressor Pressures

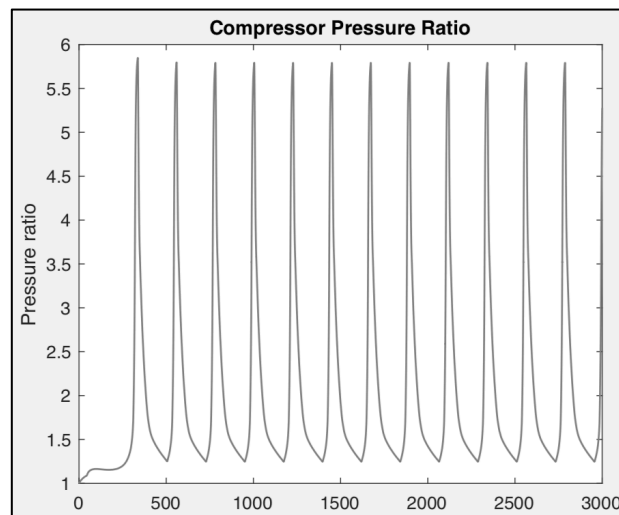


Figure 4.22: Battery Load Compressor Pressure Ratio

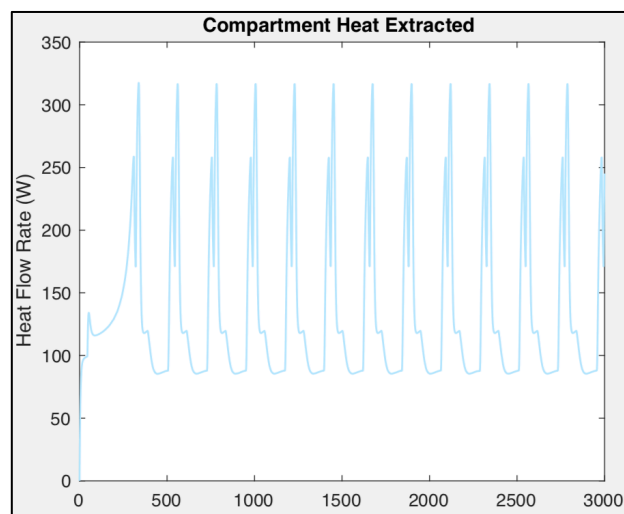


Figure 4.23: Battery Load Heat Extracted

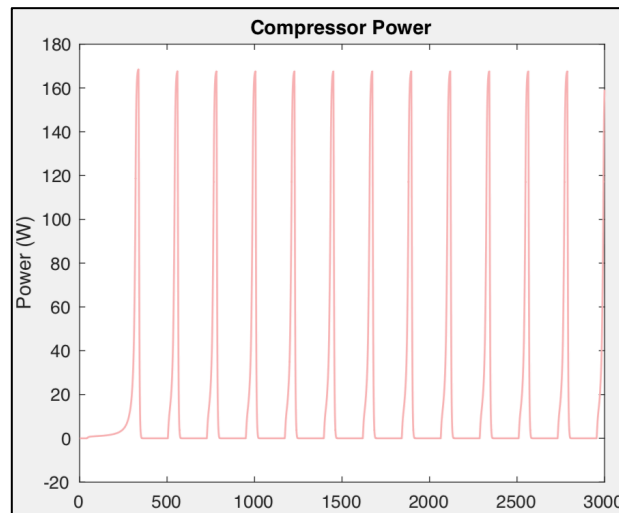


Figure 4.24: Battery Compressor Power

Based on Figure 4.21, during the compressor activation period, the compressor inlet pressure averages at 0.16 MPa, and the compressor outlet pressure averages at 0.93 MPa, which produces an average compressor pressure ratio of approximately 5.8 as seen in Figure 4.22.

As the compressor is activated, the heat in the cabin space is extracted, where the instantaneous heat extracted is constant 320 W. The instantaneous heat extracted is found to be 154 % greater than the constant battery thermal load. The higher instantaneous heat is only extracted at a short duration of time with intervals in between to address the constant battery thermal load.

Furthermore, upon inspection of the data in Figure 4.24, it can be seen that during the activation period, the compressor consumes an average power of approximately 163 W in order to extract the heat supplied to the cabin space.

As seen from the above figures, the heat extracted from the compartment follows the same pattern of fluctuation as in the previous thermal loads, however the main difference is the peaks for signals for this thermal load. The signal can be seen to be fluctuating across the base line and the peaks of the signal do not gradually increase or decrease, as well as no gradual blunting of the peaks can be observed. This signal profile is attributed to the nature of the battery thermal load, as this load is constant over time, therefore the heat extracted from the cabin space is also constant, thus resulting in the same pattern of signal at both the early and later stage of the simulation. Furthermore, the compressor power can also be seen to be fluctuating at the same frequency as the heat extracted signal, where there is also no

blunting out and gradual rise of the peaks of the signal. This represents the compressor power consumption for this type of thermal load is constant with time, where there is no requirement to increase or decrease the compressor power. The fluctuation for compressor inlet and outlet pressure, as well as the pressure ratio remains in operational limits and the signals are fluctuating with consistent frequencies. The cabin temperature profile for battery thermal load is plotted in Figure 4.25.

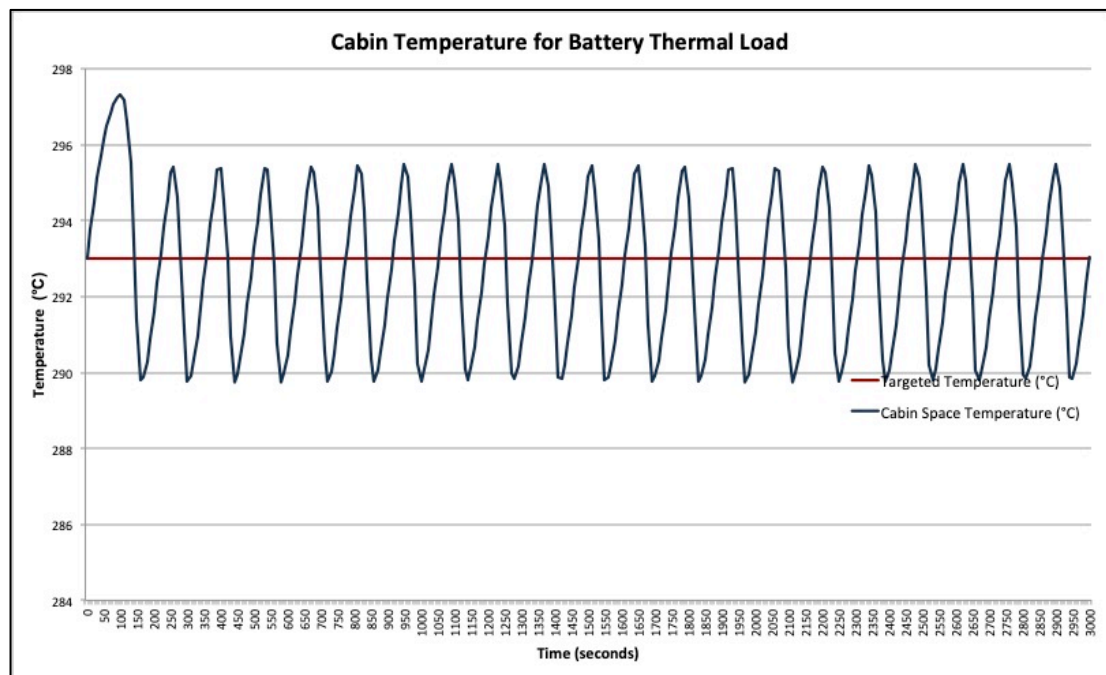


Figure 4.25: Cabin Temperature Profile for Battery Thermal Load

As expected based on the previous results, the cabin temperature is allowed to rise to a higher temperature before the refrigeration system operates to cool the cabin space, thus bringing the temperature towards the targeted cabin temperature. The maximum of temperature deviation after the system is activated is at 1230 seconds with a 0.85 % deviation from targeted temperature. Once the cabin space reaches the lower temperature limit, the refrigeration system shuts off to allow the thermal load to heat up the cabin space to the upper limit before it operates again to cool down the cabin space to the desired temperature, where this phenomenon forms the signal fluctuation. It can be observed that the peaks of the signal remain at a constant height and frequency, thus implying that no additional heat is added to the existing heat to

raise the temperature for the entire duration of the simulation. Therefore, the cabin temperature profile behaves as expected with the battery thermal load.

4.3.5 Solar Thermal Load

For the simulation of refrigeration circuit for solar thermal load, the simulation will be run for 10000 seconds. As the thermal load model is ran for both Edinburgh and Kuala Lumpur, the simulation for the refrigeration circuit will also be conducted with respect to these two locations. The refrigeration circuit response for both Edinburgh and Kuala Lumpur simulation will be discussed concurrently, as well as for the cabin temperature profile. The refrigeration circuit response for solar thermal load at Edinburgh and Kuala Lumpur is depicted in Figure 4.26 to Figure 4.33 respectively.

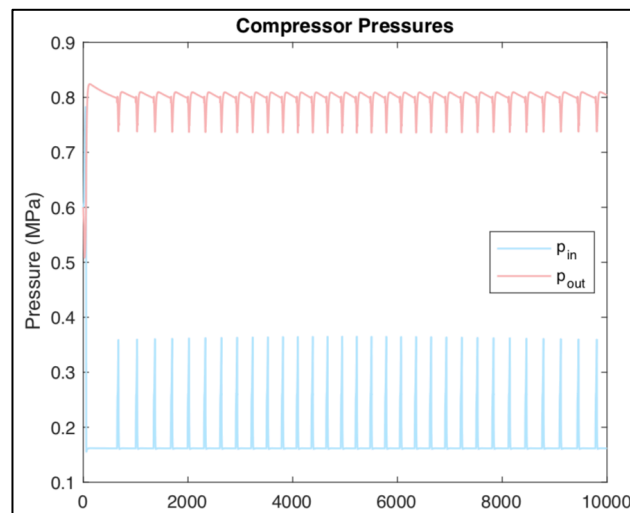


Figure 4.26: Solar Load Compressor Pressures, Edinburgh

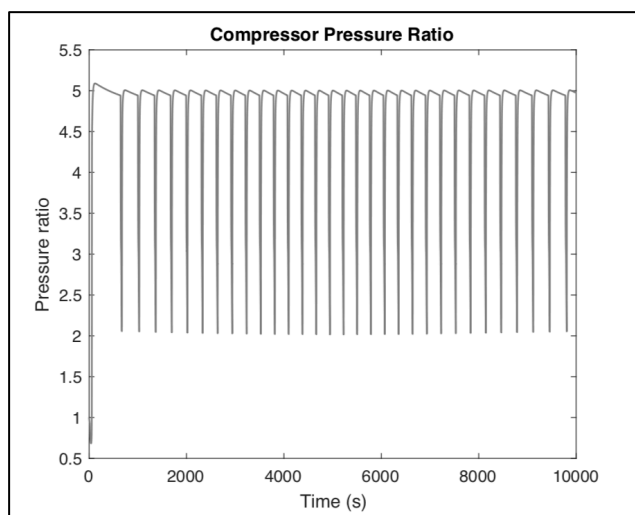


Figure 4.27: Solar Load Compressor Pressure Ratio, Edinburgh

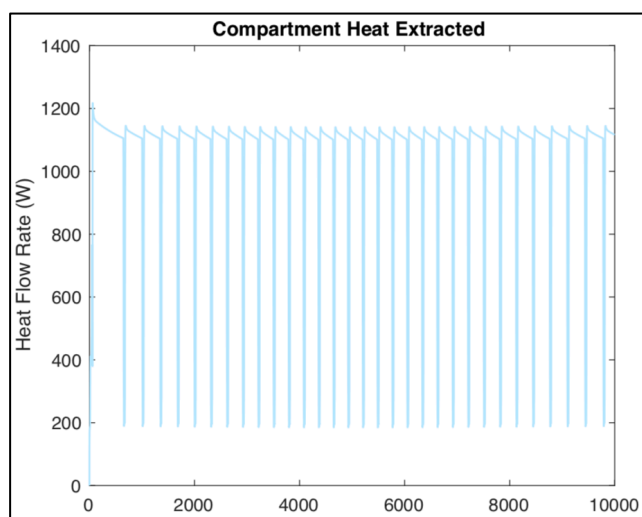


Figure 4.28: Solar Load Heat Extracted, Edinburgh

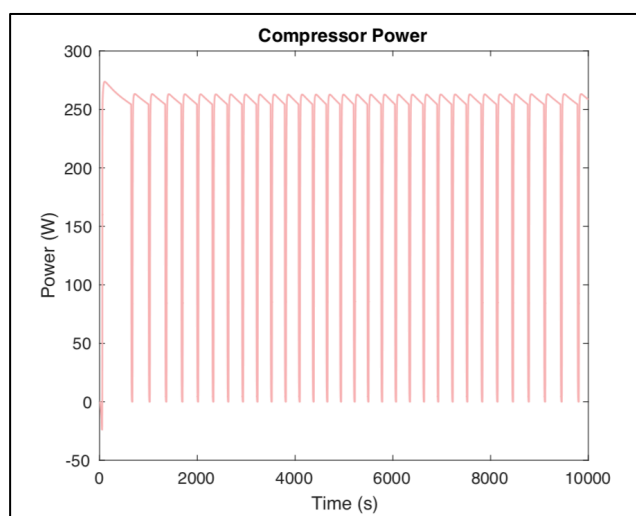


Figure 4.29: Solar Load Compressor Power, Edinburgh

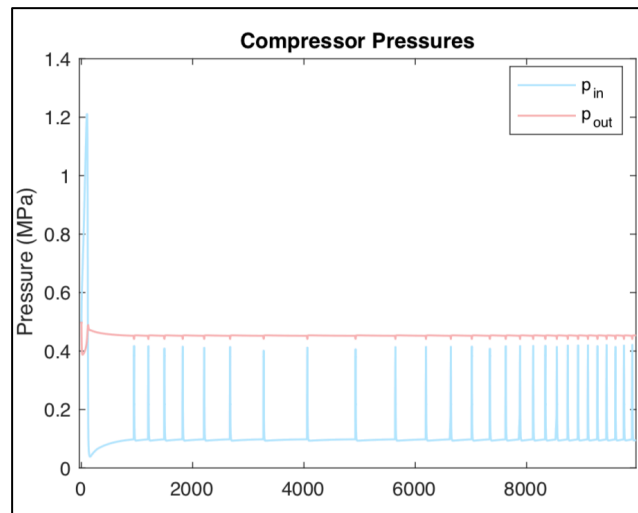


Figure 4.30: Solar Load Compressor Pressures, Kuala Lumpur

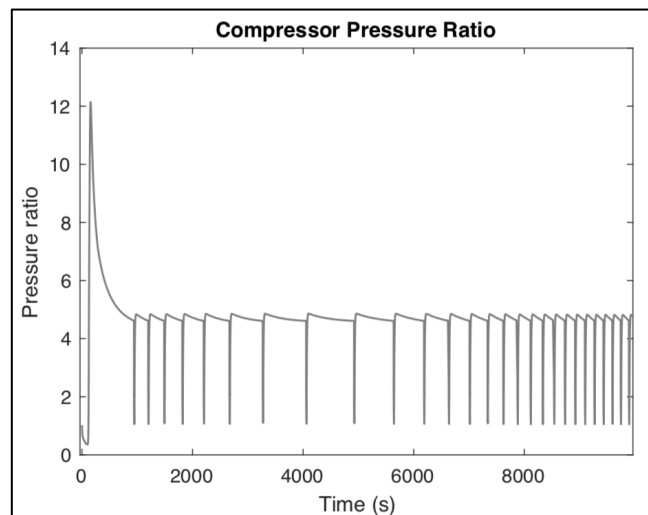


Figure 4.31: Solar Load Compressor Pressure Ratio, Kuala Lumpur

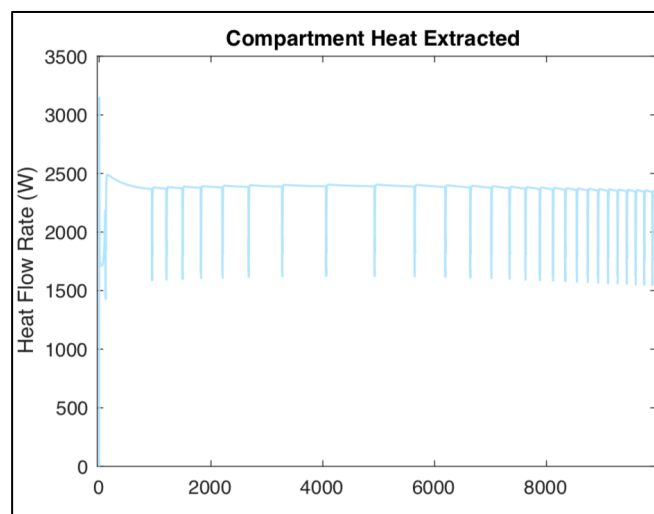


Figure 4.32: Solar Load Heat Extracted, Kuala Lumpur

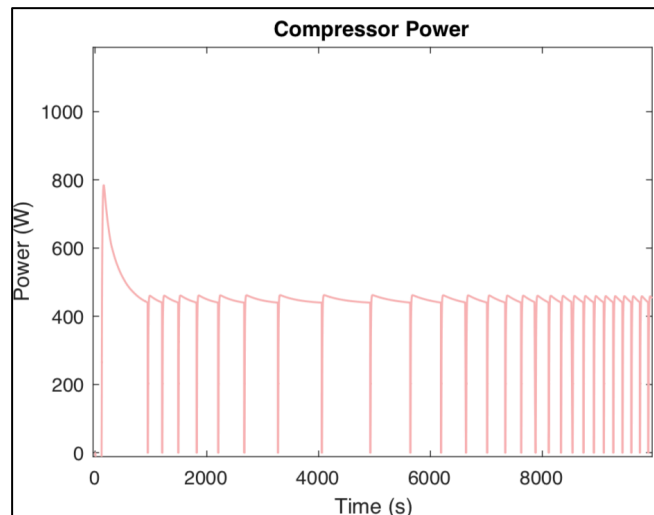


Figure 4.33: Solar Load Compressor Power, Kuala Lumpur

Based on Figure 4.27 and Figure 4.31, it can be seen that for both cases of Edinburgh and Kuala Lumpur, the compressor pressure ratio is seen to average at 5, which is considered a value acceptable in an air conditioning system.

As the compressor is activated, the heat in the cabin space is extracted, where the instantaneous heat extracted averages at 1130 W for the case of Edinburgh and a value of 2450 W for the case of Kuala Lumpur.

Furthermore, upon inspection of the data in Figure 4.29 and Figure 4.33, it can be seen that during the activation period, the compressor power averages at 260 W for the Edinburgh case and 470 W for the Kuala Lumpur case.

Even though the inputs to the refrigeration circuit for both Edinburgh and Kuala Lumpur are different in magnitude and trend, the signals for all the refrigeration circuit parameters appear to exhibit similar behaviour and profile after comparison between Figure 4.26 to Figure 4.33. Therefore, they will be discussed collectively, instead of individually, as the elaboration and justification of the signals profile will be similar for both locations. As expected, fluctuation exists in the refrigeration circuit signals for both cases, due to the operational nature of the circuit. As observed in Figure 4.29 and Figure 4.33, it can be seen that the compressor operates for a longer duration in the Kuala Lumpur case when it is activated when compared to the Edinburgh case, which can be attributed to the higher thermal load in the former case, thus necessitating the refrigeration circuit to be ran for a longer duration in order to extract the larger amount of heat from the cabin space. Furthermore, in Figure 4.33 alone, it can be seen that during midday, the compressor

can be seen to be operating at a longer duration, thus corroborating the concept that the compressor has to be operated for a longer duration in order to extract the higher amount of thermal load that exists in midday. In comparison, it can be seen that the heat extracted from cabin in Kuala Lumpur is twice the amount of heat extracted in the Edinburgh case, as the solar thermal load in Kuala Lumpur is also twice as much as the solar thermal load in Edinburgh. Comparison of the compressor power in both the Edinburgh and Kuala Lumpur case, the compressor power increment also follows the trend of the heat extracted. Thus, it is implied that the refrigeration circuit manages to remove twice the amount of heat at twice the amount of compressor power when compared between the Edinburgh and Kuala Lumpur case.

In order to further explain the operation of the refrigeration circuit, the cabin temperature profile for solar thermal load has to be studied in order to provide more contexts on the operation of the circuit during the simulation duration. The cabin temperature profile for solar thermal load for both Edinburgh and Kuala Lumpur are shown in Figure 4.34 and Figure 4.35 respectively.

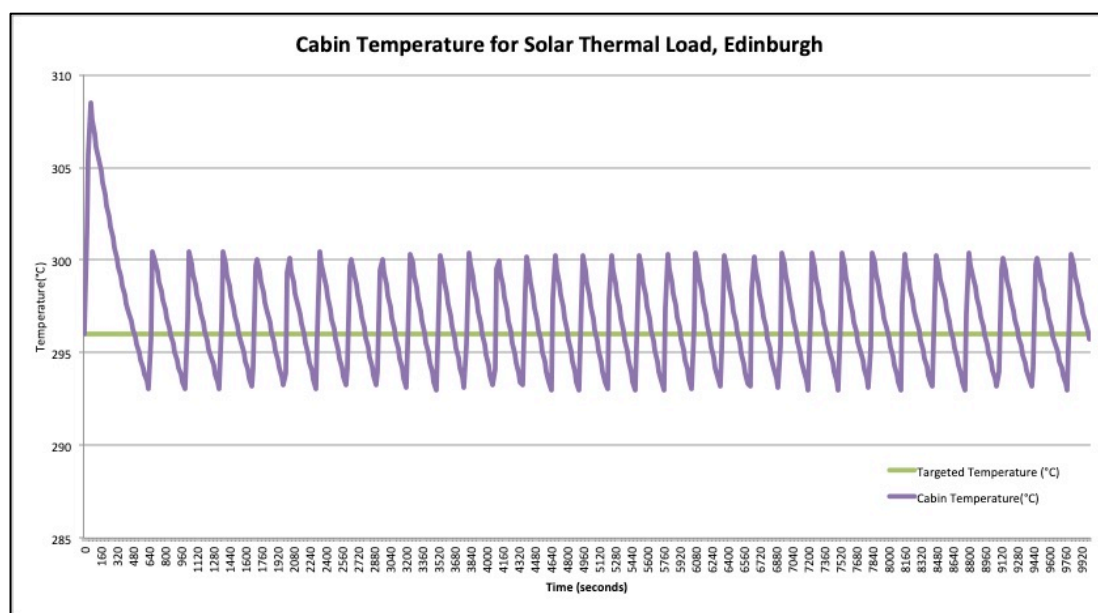


Figure 4.34: Cabin Temperature Profile for Solar Thermal Load in Edinburgh

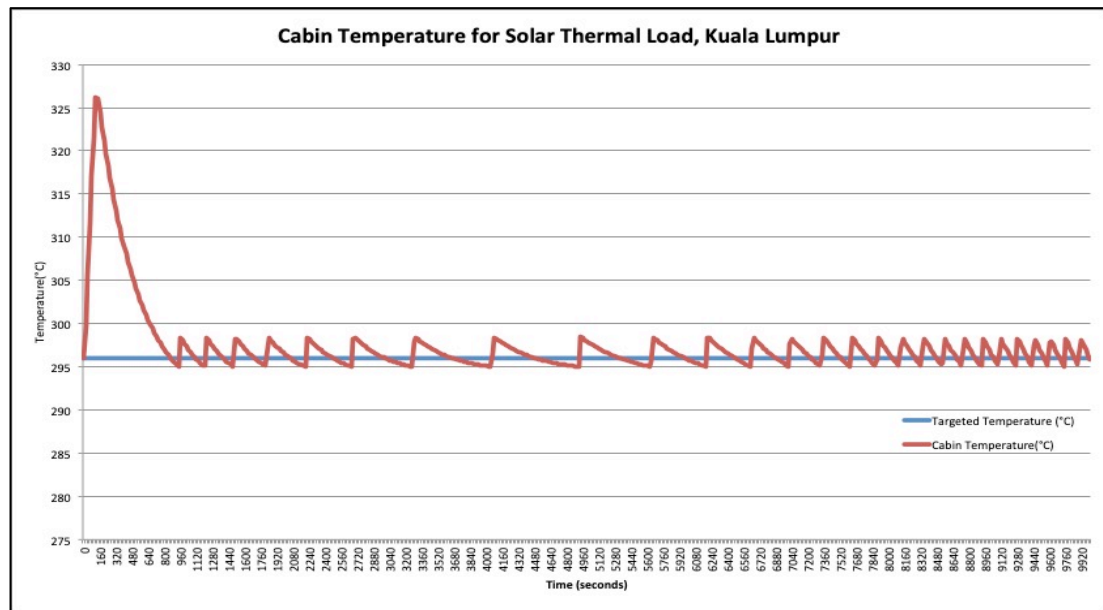


Figure 4.35: Cabin Temperature Profile for Solar Thermal Load in Kuala Lumpur

As observed in Figure 4.34 and 4.35, the temperature is allowed rise to a certain limit before the refrigeration system operates to bring the temperature down to the targeted value. The average cabin temperature deviation after the system is activated is 2.11 % and 1.85 % from targeted temperature for the case of Edinburgh and Kuala Lumpur respectively. This shows that the refrigeration circuit is capable of maintaining the actual cabin temperature acceptably near the targeted temperature.

Considering all individual thermal load cases, the refrigeration circuit response parameters are all well within normal operating limit, with the data corroborated and supported by the operating mechanism and nature, as well as interaction of the refrigeration circuit, cabin space and surrounding environment.

4.4 Comparison of Simulated and Actual Refrigeration Circuit Response

An actual experiment is conducted using the G.U.N.T Hamburg ET 400 refrigeration circuit in order to physically replicate the refrigeration circuit model. A model is also constructed in Simulink® environment based on the dimensions and operational parameters of the physical refrigeration circuit. Similar thermal load profile is inputted into both the physical and simulation model to obtain the operating performance and parameters of the refrigeration circuits. The compressor inlet temperatures, compressor outlet temperatures, compressor inlet pressures,

compressor outlet pressures and compressor powers for both simulated and physical experimental system are shown in Figure 4.36 to Figure 4.40.

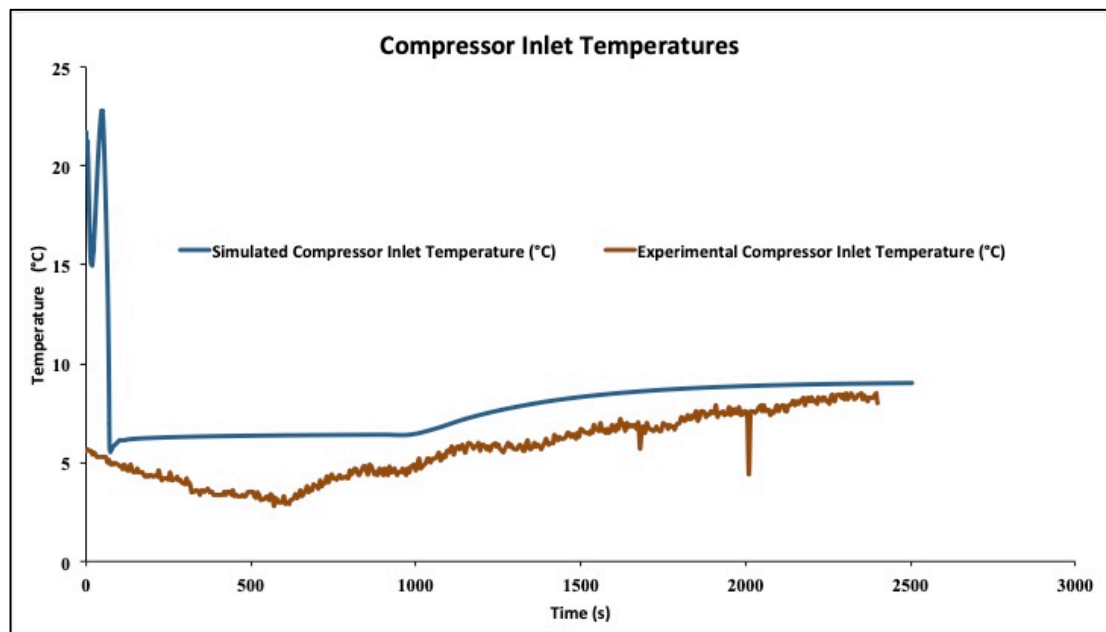


Figure 4.36: Simulated and Experimental Compressor Inlet Temperatures

Figure 4.36 shows the behaviour for both simulated and experimental compressor inlet temperature. Upon calculation of the data, the simulated compressor inlet temperature averages at 7 °C, meanwhile the experimental compressor inlet temperature averages at 5.71 °C, which has a relative error of 22 %. From the data signal, the simulated compressor inlet temperature undergoes a large fluctuation in the first 70 seconds, which is attributed to the initialisation phase of the model and subsequently remain fairly constant, with a gradual increment after 1000 seconds. This increment is attributed to the rise in thermal load input supplied to the system. In contrast, the experimental compressor undergoes its start up phase in the first 600 seconds, where the temperature gradually decreases and stabilises before subsequently increasing at a steady rate.

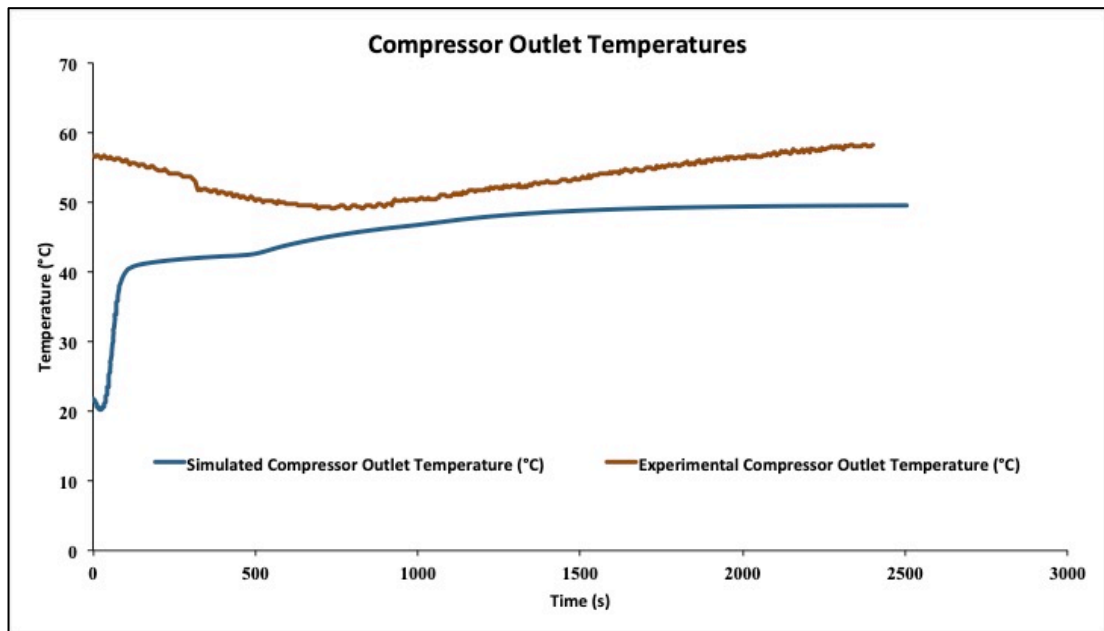


Figure 4.37: Simulated and Experimental Compressor Outlet Temperatures

Based on the data signal in Figure 4.37, the behaviour of the compressor outlet temperature is similar to the one displayed by the compressor inlet temperature. The simulated compressor outlet temperature averages at 43 °C, while the refrigerant in the physical experimental refrigeration circuit leaves the compressor at 53.42 °C. The percentage error between the two averages is 19.5 %. The simulated compressor outlet temperature experiences a large fluctuation in the first 70 seconds of simulation due to system initialisation, which behaves similarly to the physical experimental compressor that takes approximately 600 seconds to stabilise. Both the simulated and experimental compressor outlet temperature display upwards trend, associated to the rise of thermal load input supplied to the system. When the thermal load input into the system increases, it causes more heat to be extracted from the compartment, where signals sent to the compressor demand it to work at a higher rate, thus generating a larger compression ratio to cope with the rise in thermal load input. As per Gay-Lussac's Law, a rise in pressure in the compressor will cause its temperature to rise accordingly, which can be observed in the trend line of both the simulated and physical experimental compressor outlet temperature.

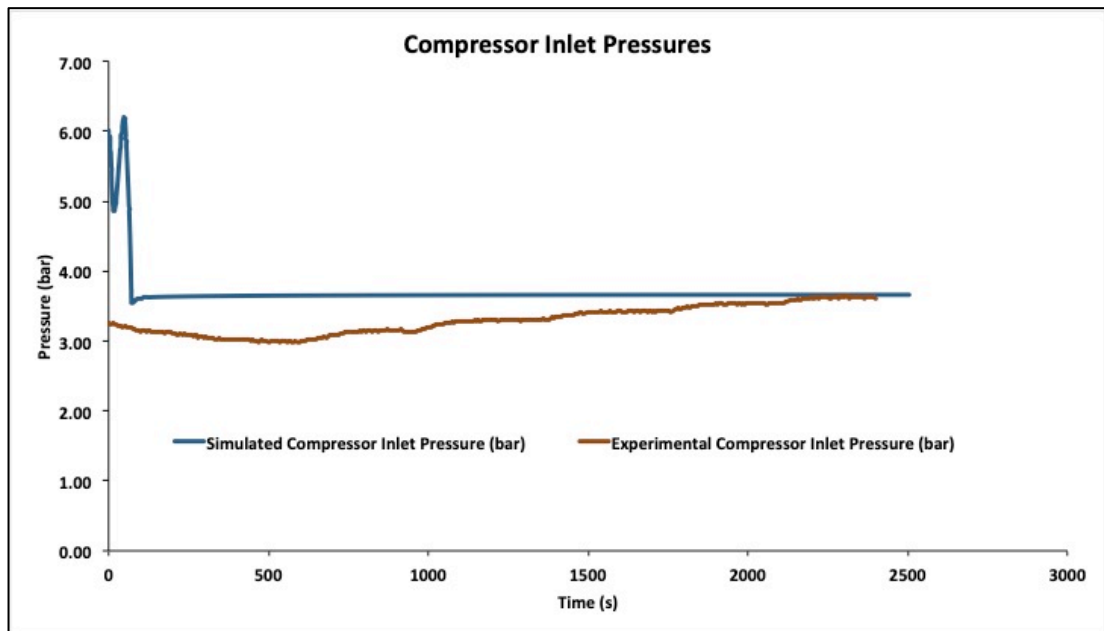


Figure 4.38: Simulated and Experimental Compressor Inlet Pressures

From Figure 4.38, the simulated compressor inlet pressure remains relatively constant with an average pressure of 3.65 bar after an initialisation phase in the first 60 seconds of the signal. The physical experimental compressor inlet pressure averages at 3.29 bar, and upon calculation, the relative error between the simulated and experimental pressure is found to be 10.94 %. The gradual rise in the experimental compressor inlet pressure can again be attributed to the rise in thermal load input. The increment in thermal load input causes greater amount of heat to be extracted from the refrigerated compartment via the evaporator, which causes the refrigerant to be superheated, where increase of temperature and pressure results from additional heat supplied.

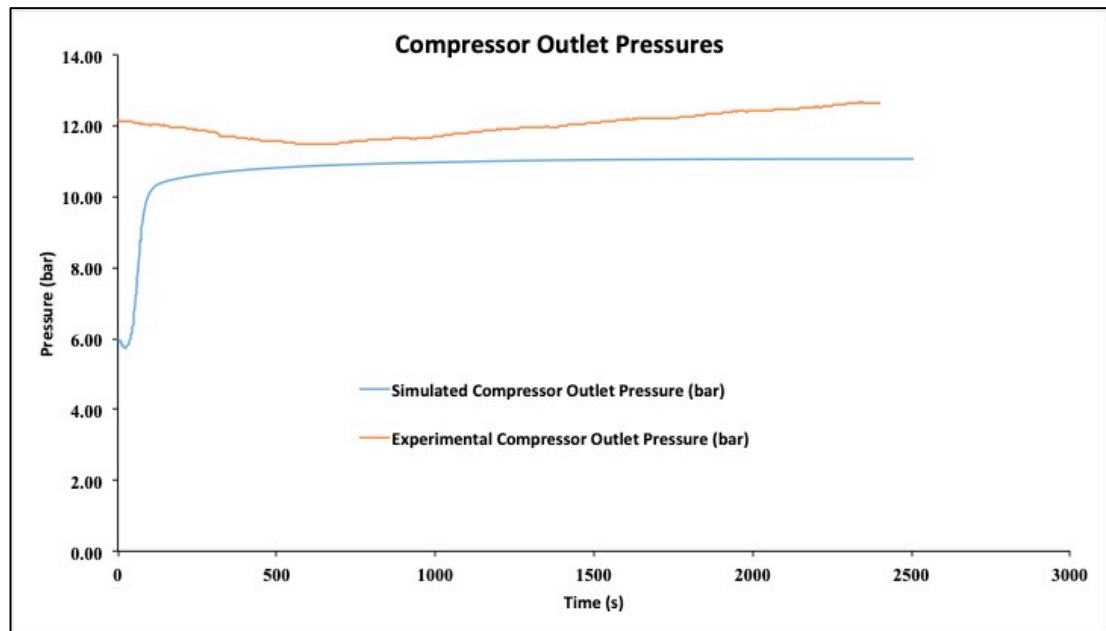


Figure 4.39: Simulated and Experimental Compressor Outlet Pressures

Based on the raw data from Figure 4.39, the average simulated compressor outlet pressure is found to be 10.37 bar, while in the case of the experimental compressor, the refrigerant is found to be compressed to an average pressure of 12 bar upon exit from the compressor. The two averages are relatively close to each other with a relative error of only 13.58 %. In this result, the experimental outlet pressure is consistently higher than the simulated result, whereas in the compressor inlet pressure, the experimental pressure is consistently lower than the simulated result, thus indicating that the compressor pressure ratio is consistently higher in the physical experiment. The compressor pressure ratio for physical circuit is relatively higher due to the need to compensate for non-ideal state of the physical system and pressure loss across each component. The compression ratio for the simulated system is lower due to the ideal state of the components in Simscape™ environment as well as the absence of pressure loss across each component. However so, the general behaviour of the pressure profile for both physical and simulated refrigeration circuit is similar.

Based on the averages of both the compressor inlet and outlet pressure, the compressor pressure ratio can be estimated for both simulated and physical refrigeration circuit. On average, the simulated compressor has a pressure ratio of 2.84; meanwhile the physical compressor has an average pressure ratio of 3.65, with a relative error of 22.12 %

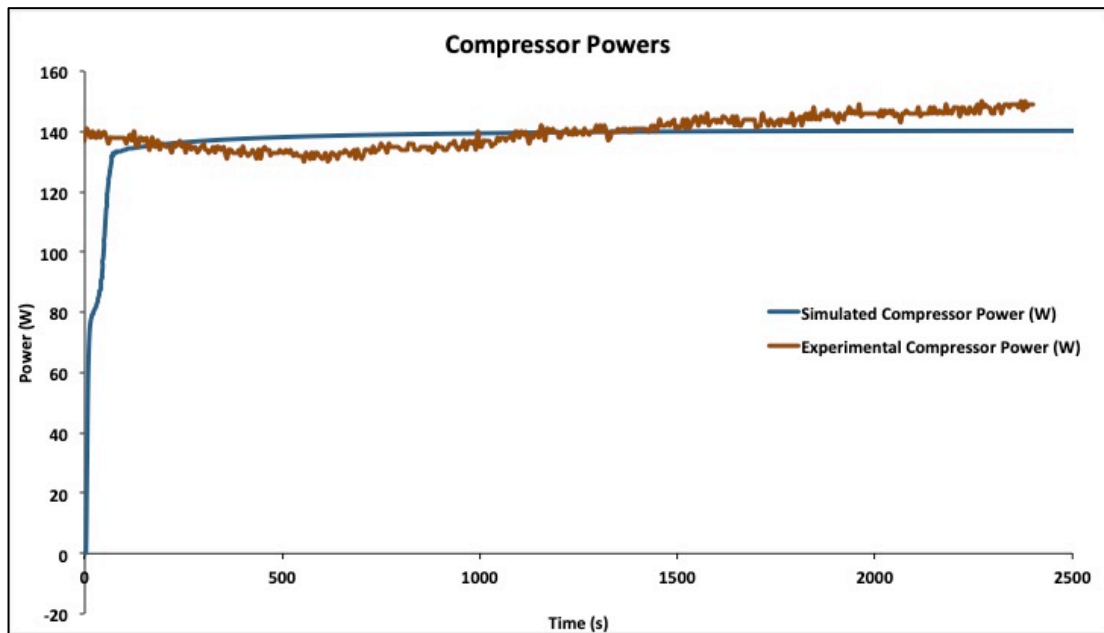


Figure 4.40: Simulated and Experimental Compressor Powers

According to the data in Figure 4.40, the physical refrigeration circuit consumes an average of 139.77 W for the operation of its compressor. As mentioned in the refrigeration circuit test rig's manual, the power consumption of the test compressor is supposed to be constant. In the actual experiment, the compressor power maintains a relatively straight line, although there is a slight reduction in power associated with the start up of the system and a slight increase in power, which is associated with the increased thermal load input. When contrasted with power consumption of the physical refrigeration circuit of 140 W, the power consumption estimation of 137.02 W by the simulation of experimental model suggest that the simulation produces a relatively precise value relative to the actual value, with a relative error of only 1.97 %.

In short, the simulated experimental model is capable of producing compressor inlet and outlet pressure, as well as compressor power consumption values that are relatively accurate to the physical refrigeration system. Although significant discrepancies occur between the simulated and actual physical temperatures in the refrigeration circuit, these errors can be justified by the heat loss in the physical experiment due to insufficient insulation of the refrigeration circuit. The parameter's behaviour and profiles are largely similar between the simulated and physical refrigeration circuit, hence it can be summarised that the simulation is

capable of producing a close approximation of the response of a physical refrigerant circuit.

4.5 Expansion Work on Different Driving Cycles

As the refrigeration circuit model is capable of producing good approximation of a physical system, it can then be expanded to study the effects of battery heat generation due to different driving cycles on the response of the refrigeration circuit. Battery heat load from three different driving cycles will serve as input to the refrigeration model, and their response will be discussed.

4.5.1 Response of Refrigeration Circuit on UDDS Driving Cycle

The heat generated by the EV's battery that is being tested on the UDDS driving cycle represents the battery thermal load when an EV is being driven in an urban environment. The simulation time for this driving cycle is 10560 seconds. The thermal heat profile is illustrated in Figure 4.41.

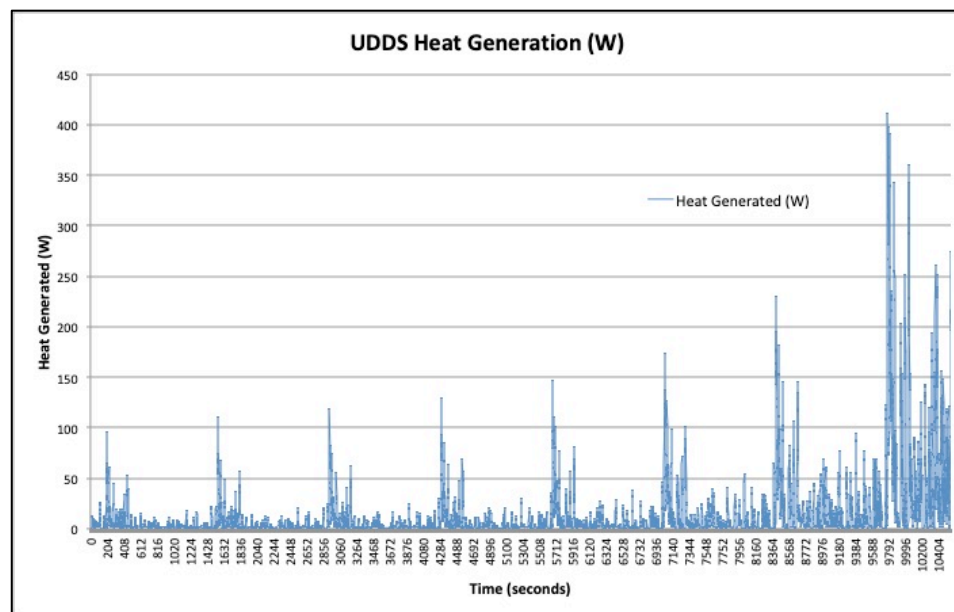


Figure 4.41: UDDS Heat Generation Profile

The heat generation profile of UDDS driving cycle suggests that there is intermittent large consumption of battery discharge that causes spikes in the heat generation. These heat spikes increases from the early stage to the end stage as indicated by the magnitude of the peaks of the thermal load, where in the later stage,

large amount of heat is generated by the battery for a continuous time period. The maximum amount of heat generated by the battery is 411.93 W at 9786 seconds. The responses of the refrigeration circuit to the UDDS driving cycle battery thermal load are shown in Figure 4.42 to Figure 4.45.

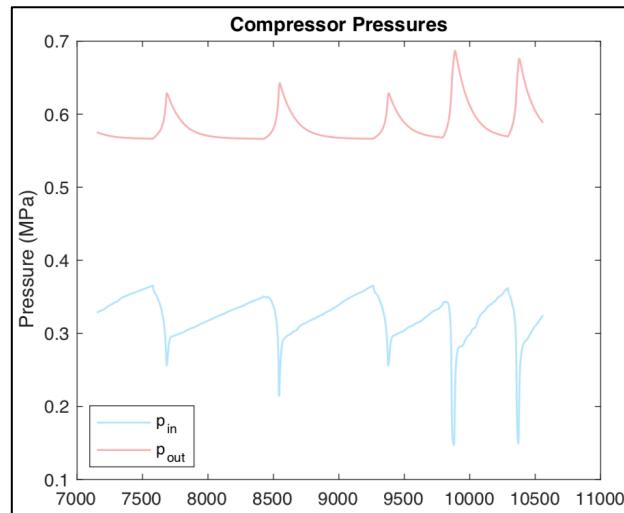


Figure 4.42: Compressor Cycle for UDDS Driving Cycle

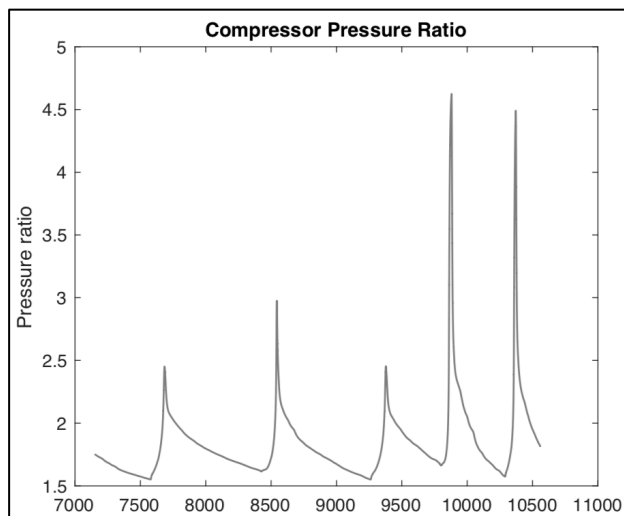


Figure 4.43: Compressor Pressure Ratio for UDDS Driving Cycle

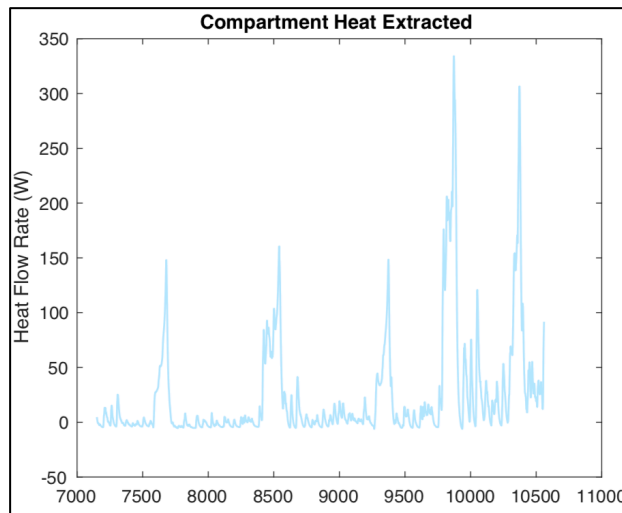


Figure 4.44: Heat Extracted for UDDS Driving Cycle

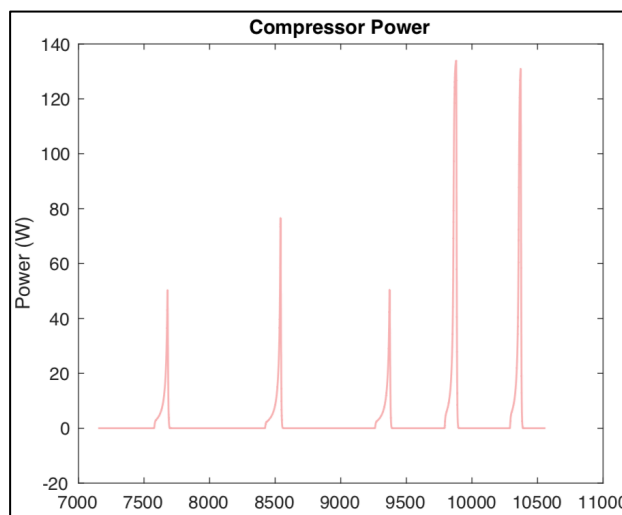


Figure 4.45: Compressor Power for UDDS Driving Cycle

Based on Figure 4.42, during the compressor activation period, the compressor inlet pressure bottoms at 0.15 MPa, and the compressor outlet pressure peaks at 0.68 MPa, which produces an average compressor pressure ratio of approximately 4.6 as seen in Figure 4.43.

As the compressor is activated, the heat in the cabin space is extracted, where the peak instantaneous heat extracted is 340 W.

Furthermore, upon inspection of the data in Figure 4.45, it can be seen that during the activation period, the compressor consumes a peak power of approximately 130 W in order to extract the heat supplied to the cabin space.

For the UDDS driving cycle heat generation, simulation from 7000 seconds to 105600 seconds will be discussed, as the heat generation in this region is significantly greater than the heat generation in the early stages of simulation. The heat extracted from the battery compartment matches the profile of the battery thermal load, where in the time period of interest, there is a total of five thermal load peaks in Figure 4.41 and also five peaks in the heat extracted graph in 4.44. Fluctuations in the heat extracted matches the battery thermal load, thus indicating the refrigeration circuit is successful in removing the heat. Furthermore, the instantaneous compressor power consumption also peaks at times specific to high thermal load, which represents the compressor, is activated only when the thermal load is high. At lower thermal load levels when the compressor is inactive, the heat is removed by virtue of the heat transfer to the refrigerant in the evaporator. It is worth noting that at the final stages of simulation, where the thermal load is higher, the compressor consumed more power in order to extract a greater amount of heat. The pressure and compression ratio are in acceptable operating range of the compressor and peaks only at time period when the compressor is activated.

Figure 4.46 shows the temperature profile of the battery location, where the compartment is desired to be kept constant at a temperature of 23 °C.

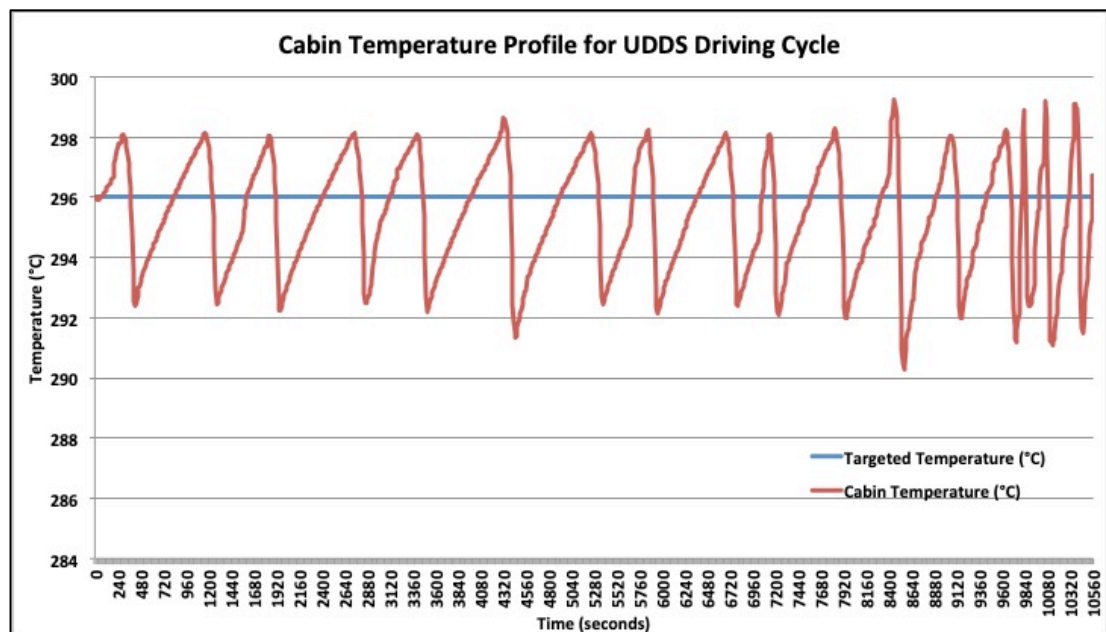


Figure 4.46: Battery Compartment Temperature Profile for UDDS Driving Cycle

For the entire duration of simulation, it is seen that the battery compartment temperature is fluctuating across the desired compartment temperature. The maximum of temperature deviation after the system is activated is at 8460 seconds with a 1.09 % deviation from targeted temperature. Fluctuations in the temperature profile is due to the nature of the system, where the temperature is allowed to fluctuate within a range of temperatures before the system is activated to remove the heat in the compartment in order to lower its temperature. It is interesting to note that when the thermal load is higher in the final stages, the temperature fluctuates more frequently as compared to early stages, due to a faster compartment heating as a result of larger heat generation. Even so, the refrigeration circuit still manages to maintain the compartment temperature within its desired limits.

4.5.2 Response of Refrigeration Circuit on HWFET Driving Cycle

The heat generated by the battery in the HWFET driving cycle represents the battery thermal load when an EV is driven on a highway. This driving cycle is typically tested for 4139 seconds, which will also be the duration for this simulation. The heat generated by the battery during a HWFET driving cycle rest is recorded as shown in Figure 4.47.

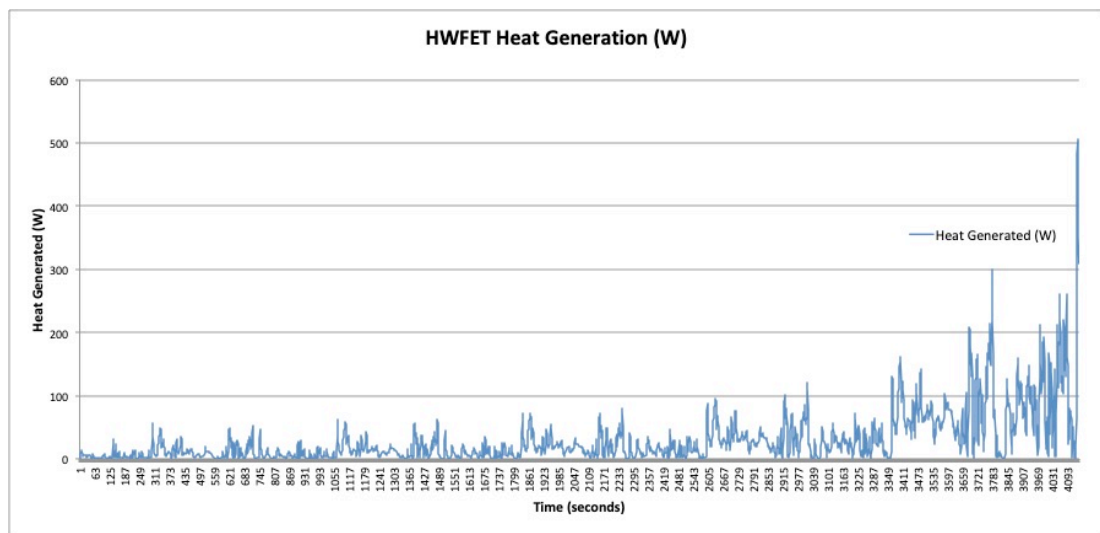


Figure 4.47: HWFET Heat Generation Profile

The majority of the heat generated during the HWFET driving cycle is relatively low, except for the final 3000 seconds, where an increased amount of heat is generated. The maximum amount of heat generated by the battery is 505.20 W at

4133 seconds. The heat profile also has less peaks and fluctuations as compared to the UDDS driving cycle, as commute on a highway is generally smooth with less acceleration and deceleration. The refrigeration circuit responses to HWFET driving cycle are presented in Figure 4.48 to Figure 4.51.

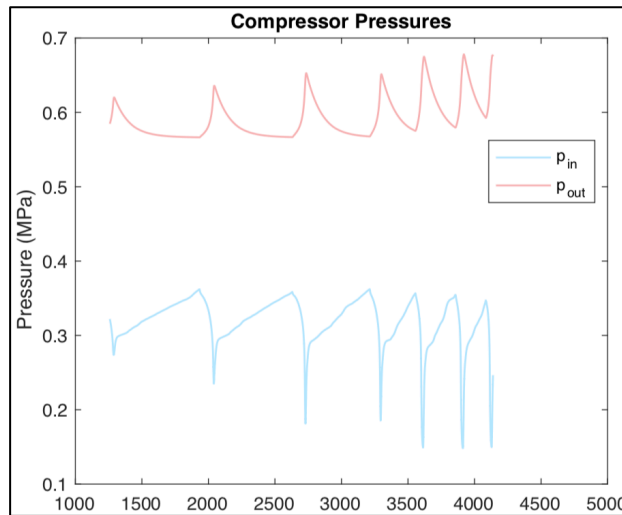


Figure 4.48: Compressor Cycle for HWFET Driving Cycle

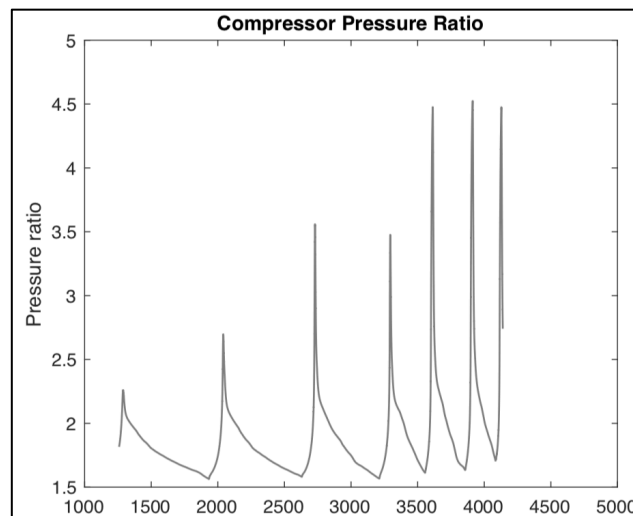


Figure 4.49: Compressor Pressure Ratio for HWFET Driving Cycle

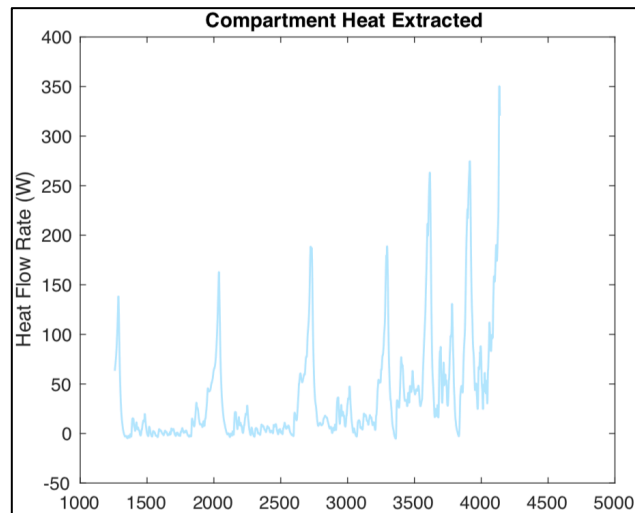


Figure 4.50: Heat Extracted for HWFET Driving Cycle

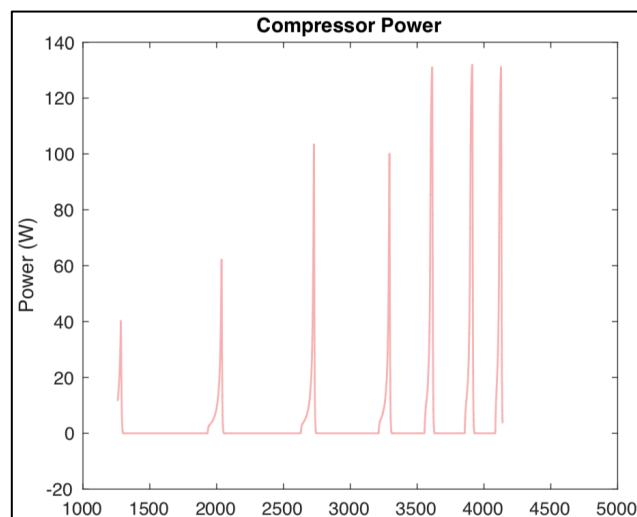


Figure 4.51: Compressor Power for HWFET Driving Cycle

Based on Figure 4.48, during the compressor activation period, the compressor inlet pressure bottoms at 0.15 MPa, and the compressor outlet pressure peaks at 0.68 MPa, which produces an average compressor pressure ratio of approximately 4.5 as seen in Figure 4.49.

As the compressor is activated, the heat in the cabin space is extracted, where the peak instantaneous heat extracted is 350 W.

Furthermore, upon inspection of the data in Figure 4.51, it can be seen that during the activation period, the compressor consumes a peak power of approximately 130 W in order to extract the heat supplied to the cabin space.

The simulation from 1000 seconds to 4139 seconds will be discussed, as this region has a relatively higher thermal load as compared to the earlier region of simulation. The compartment heat extracted profile matches the battery heat generation profile, especially at the final 1000 seconds of simulation, where the increased heat from the battery is compensated by an increased of heat extracted from the compartment, thus inferring that the refrigeration circuit behaves as predicted in successfully removing the thermal load from the compartment. Peaks in the thermal load closely matches the peaks in the compressor power and heat extracted, hence suggesting an increase of thermal load causes the system to react by activating the compressor to remove the heat added to the compartment. This behaviour is more prominent in the final 1000 seconds, where the heat generation is larger than earlier times, thus causing the compressor to consume more power in order to remove a greater amount of heat from the compartment. The data on compressor inlet and outlet pressure as well as the pressure ratio suggest the circuit is operating normally, with an increase in compression ratio during high compressor power consumption. A review of the compartment instantaneous temperature profile, shown in Figure 4.52 reveals more details on the behaviour of the refrigeration circuit.

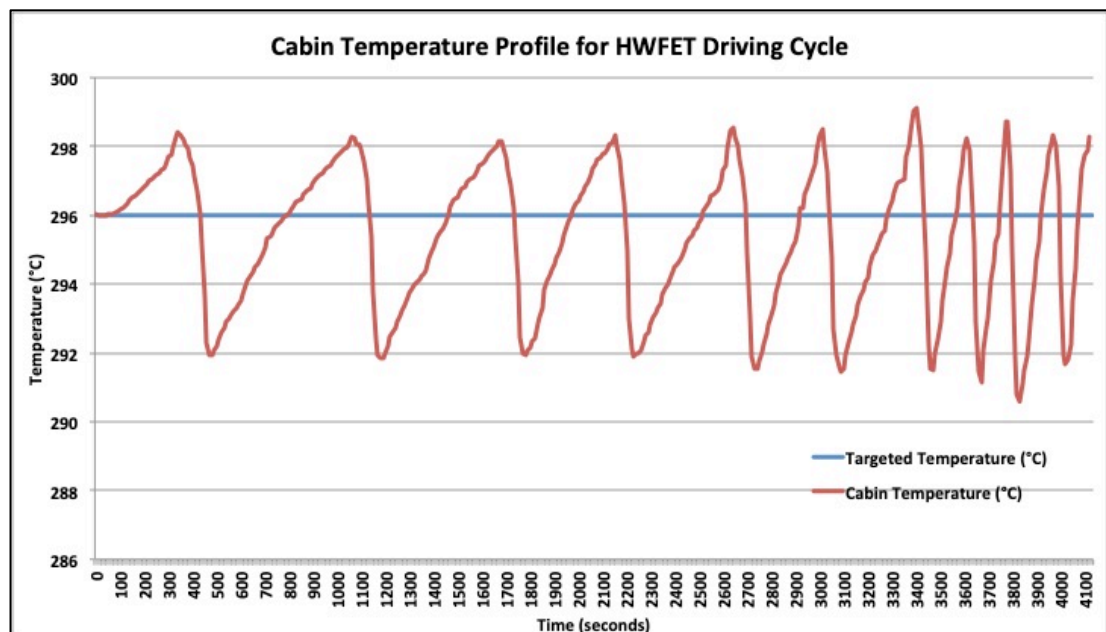


Figure 4.52: Battery Compartment Temperature Profile for HWFET Driving Cycle

A look on the battery compartment temperature profile reveals that the refrigeration circuit is successful in maintaining the compartment temperature near the targeted temperature. The maximum of temperature deviation after the system is activated is at 3390 seconds with a 0.81% deviation from targeted temperature. The actual temperature is fluctuating across the targeted temperature within a narrow range of temperature, which is behaviour acceptable to the current system. In the final 1000 seconds of simulation, it is observed that the fluctuation increase in frequency, indicating that an increased in thermal load that causes the temperature to increase at a higher rate, thus the system react accordingly by cooling down the compartment, whilst keeping the actual temperature within a narrow range of values across the desired temperature.

4.5.3 Response of Refrigeration Circuit on US06 Driving Cycle

US06 driving cycle battery heat generation profile is used to simulate the battery thermal load generated by battery discharging when the EV is driven aggressively, with frequent hard acceleration and deceleration. This driving cycle is typically tested and simulated for 2103 seconds. The heat generated by the battery during a US06 driving cycle is plotted in Figure 4.53.

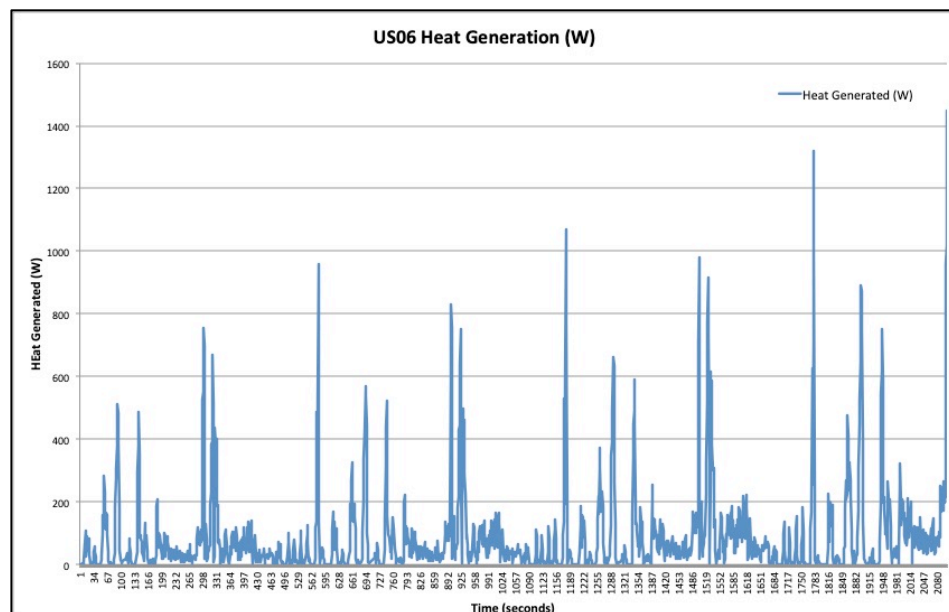


Figure 4.53: US06 Heat Generation Profile

The heat generation profile for this driving cycle shows stark contrast to the previous two driving cycles. The maximum amount of heat generated by the battery is 1318.06 W at 2103 seconds. The signal in this case has greater number of peaks, suggesting that the vehicle undergoes very frequent acceleration and deceleration, which causes more frequent heavy battery discharge and heat generation. The non peak regions of the graphs also record values that are higher than the non peak regions from the previous two driving cycles, therefore implying that a heavier discharge even at normal driving, resulting in a greater amount of heat generated during the entire driving cycle. The refrigeration circuit responses to US06 driving cycle are shown in Figure 4.54 to Figure 4.57.

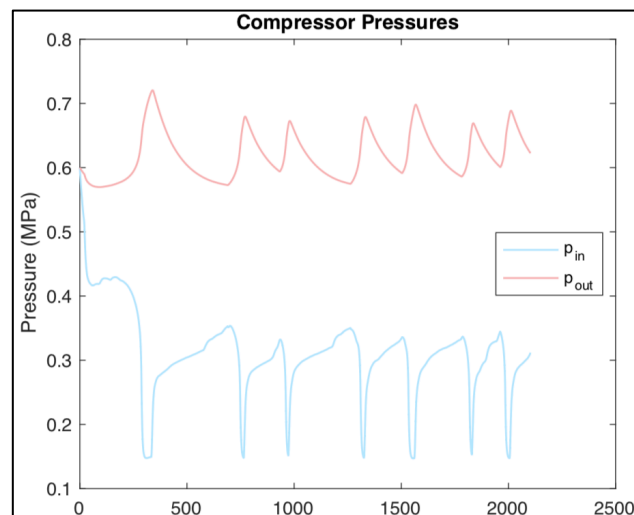


Figure 4.54: Compressor Pressures for US06 Driving Cycle

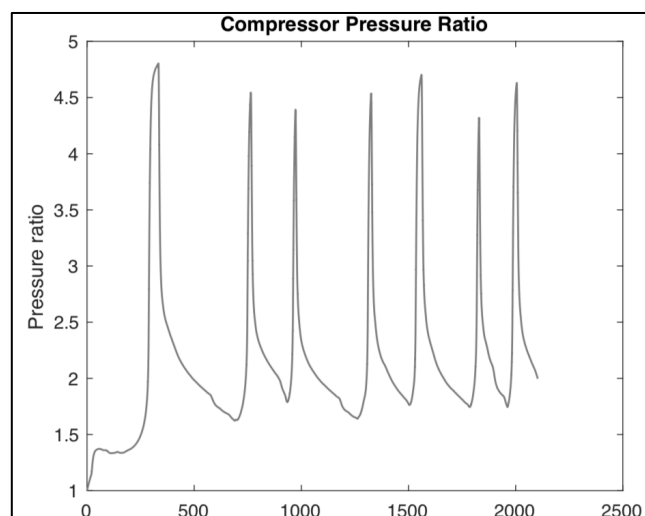


Figure 4.55: Compressor Pressure Ratio for US06 Driving Cycle

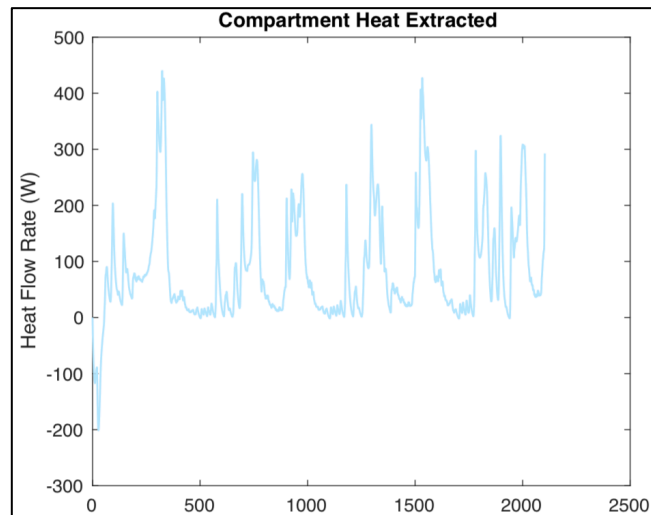


Figure 4.56: Heat Extracted for US06 Driving Cycle

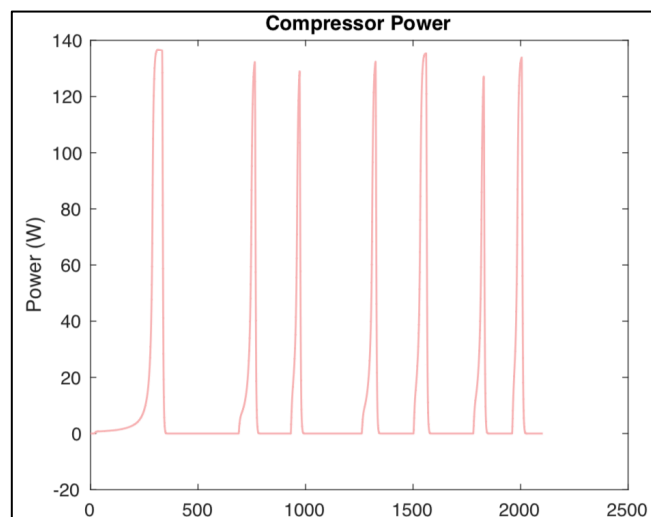


Figure 4.57: Compressor Power for US06 Driving Cycle

Based on Figure 4.54, during the compressor activation period, the compressor inlet pressure bottoms at 0.15 MPa, and the compressor outlet pressure peaks at 0.72 MPa, which produces an average compressor pressure ratio of approximately 4.8 as seen in Figure 4.55.

As the compressor is activated, the heat in the cabin space is extracted, where the peak instantaneous heat extracted is 440 W.

Furthermore, upon inspection of the data in Figure 4.57, it can be seen that during the activation period, the compressor consumes a peak power of approximately 138 W in order to extract the heat supplied to the cabin space.

The parameters for the entire duration simulation are discussed, as the heat generated is significant at every second of this driving cycle. The compartment heat extracted profile loosely matches the heat generation profile, where it can be seen that the heat extracted signal fluctuates at a higher frequency as compared to the previous driving cycles due to the more frequent and greater heat introduced into the compartment by the battery. It is also worth noting that the width of the peaks are wider, suggesting a greater amount of heat extracted at instances corresponding to a more continuous and higher thermal load, as seen in 859 seconds to 1024 seconds, as well as 1717 seconds to 2103 seconds. The peak frequency and value for compressor power is also increased compared to previous driving cycles, inferring that the compressor is activated more frequently and working more aggressively in order to removed the battery thermal load. This phenomenon is corroborated by the data from the compressor inlet and outlet pressure, as well as the compression ratio, where the most of the peaks in the compression ratio graphs exceeds a value of four. Although the compressor parameters are relatively higher, however it is will operating within its normal range of values. Figure 4.58 shows the battery compartment temperature profile for US06 driving cycle.

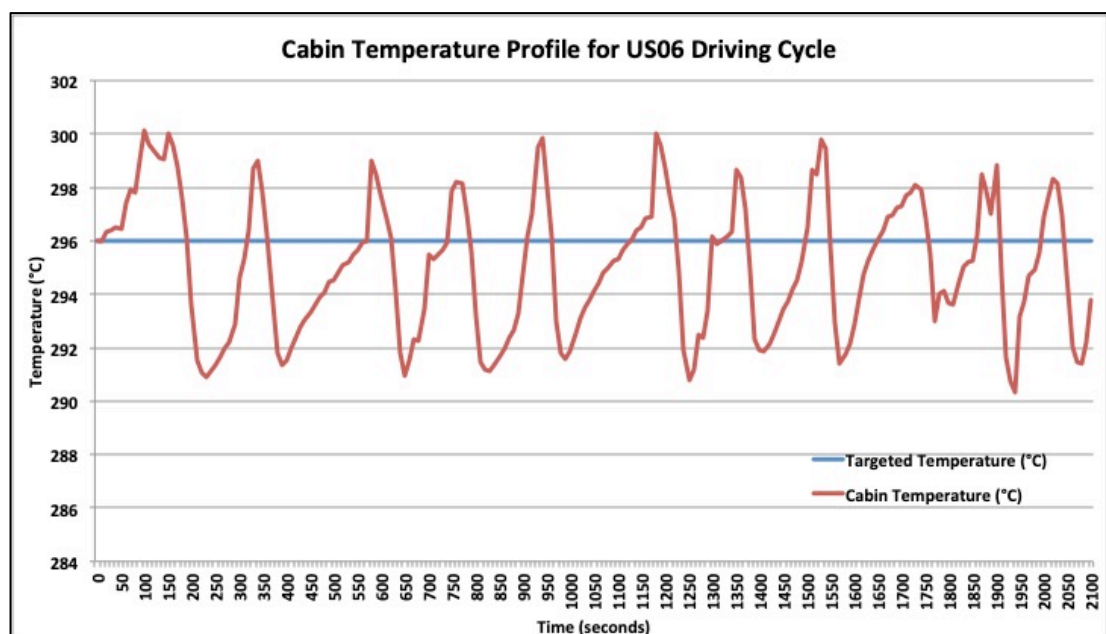


Figure 4.58: Battery Compartment Temperature Profile for US06 Driving Cycle

The actual instantaneous compartment temperature changes more frequently and rapidly as compared to the previous cycles, which can be attributed to the more frequent peaks in the battery thermal load. The maximum of temperature deviation after the system is activated is at 100 seconds with a 1.4 % deviation from targeted temperature. The temperature profile in this case lacks the consistency displayed in the previous driving cycles, due to the more frequent and severe fluctuation in the thermal load. Albeit the increased heat generation in the compartment, the refrigeration circuit still manages to maintain the compartment temperature near the desired temperature during the entire simulation period. Hence, the behaviour of the refrigeration circuit for this case is still within expectation.

In short, the refrigeration circuit's behaviour for the three driving cycles are as expected, with the compressor inlet and outlet pressure, as well as the compression ratio within normal operating range. The compressor power consumption as well and compartment temperature response is also within acceptable ranges. Henceforth, the refrigeration circuit is successful in extracting the heat from the battery compartment, whilst maintaining all its parameters within acceptable limits, suggesting the refrigeration circuit model can be used to approximate the performance of a refrigeration circuit in an EV that is subjected to variation of battery heat generated during battery discharging at different driving cycles.

4.6 Expansion Work on Cabin Temperature-Predicting Algorithm

The thermal load model in Phase 1 can be expanded to predict the cabin temperature. The basis of this algorithm is to predict the cabin temperature based on the amount of solar irradiance subjected on a vehicle, which allows the changes in cabin temperature to be observed with regard to the time domain. In this expansion, the cabin temperature-predicting algorithm will be applied to both Edinburgh and Kuala Lumpur.

4.6.1 Cabin Temperature Predicting in Edinburgh, Scotland

The predicted cabin temperature in Edinburgh, Scotland based on the algorithm is plotted in Figure 4.59, where a simulation has been ran for 3600 seconds with solar irradiance as input.

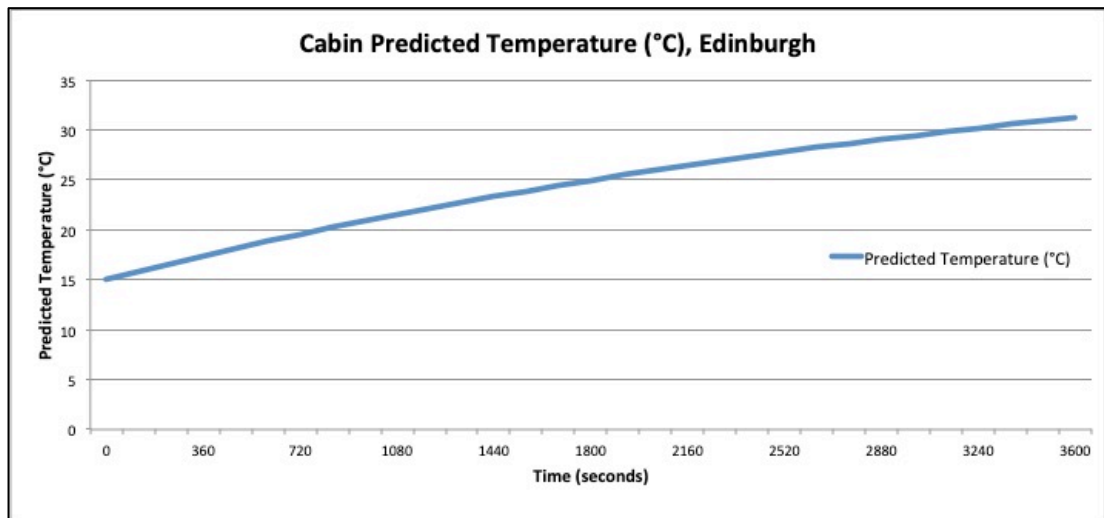


Figure 4.59: Predicted Cabin Temperature in Edinburgh, Scotland

During the process of predicting the cabin temperature at Edinburgh, Scotland, data from the solar irradiance model, constant outside temperature and initial cabin temperature serve as the input. The initial temperature in this case is taken to be 15 °C. The time interval between temperature predictions is set at two minutes or 120 seconds; hence the next iteration of the prediction is 120 seconds after the current one. The data in Figure 4.59 shows that the cabin temperature is trending upwards, which is justified by the continuous solar irradiance on the vehicle. Upon closer look at the raw data, the predicted cabin temperature is actually increasing at an exponential rate, with the slope slightly reducing as the temperature increase, hence suggesting an impending saturation point. A simple calculation reveals that the cabin temperature has risen by 16.23 °C within an hour. A projection of this trend line will show that the cabin temperature will eventually saturate at a specific cabin temperature.

4.6.2 Cabin Temperature Predicting in Kuala Lumpur, Malaysia

The predicted cabin temperature in Kuala Lumpur, Malaysia based on the algorithm is presented in Figure 4.60, which also has a simulation time of 3600 seconds.

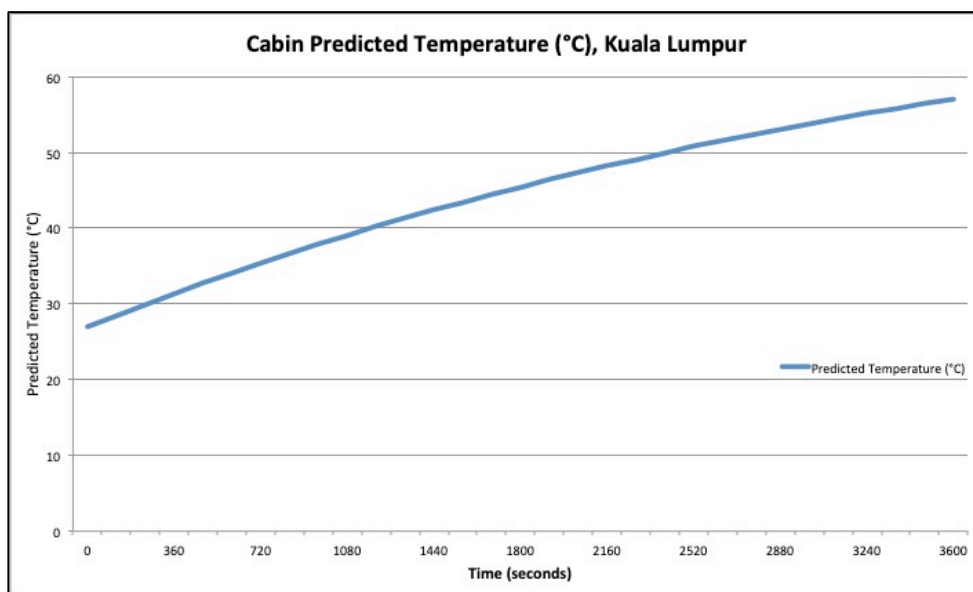


Figure 4.60: Predicted Cabin Temperature in Kuala Lumpur, Malaysia

The type of inputs for this variation of algorithm is the same as the ones in Edinburgh, but the values has been changed to better reflect the climate conditions in Kuala Lumpur. The initial cabin temperature is 27 °C, which is regarded as the average temperature in a tropical climate. The predicted cabin temperature also shows an upward trend, associated to the continuous solar irradiance on the cabin space of the vehicle. However, upon visual inspection, the gradient of the line is steeper than the previous case, supported by a simple calculation, which states that the temperature has risen 30 °C within an hour, a slope that almost doubles the previous one. This is attributed to the solar irradiance, as stated in earlier section is almost double in Kuala Lumpur as compared to Edinburgh. The slope in this case is also exponential, where it is slightly shallower with every temperature rise. Therefore, this observation suggests a saturation point if a projection of the cabin temperature is conducted beyond the time of interest here.

4.7 Supporting Infrastructure on Cabin Cooling

The effects of the implementation of supporting infrastructure on cabin cooling will be discussed, which includes both the passive and active infrastructure. For the passive infrastructure, namely the increment of window glazing from single to triple glazing, its effects of the solar irradiance on the vehicle cabin as well as the cabin space temperature will be discussed. Furthermore, in the case of active infrastructure

that consists of two 21 W extractor fans, the effects of these extractor fans on the cabin space temperature will be studied and elaborated. Lastly, the combined effects of active and passive infrastructure on the changes cabin space temperature will be examined.

4.7.1 Passive Supporting Infrastructure on Cabin Cooling

The passive supporting infrastructure in this case is the triple glazing of the EV windows that effectively reduces the radiation transmittance into the cabin space. This causes a reduction in solar irradiance introduced to the vehicle and a reduction in the cabin temperature. The data on the solar irradiance through triple glazing will be compared along data of single glazing windows in order to provide a good contrast between the data. The comparison of solar irradiance into cabin with single and triple window glazing in Edinburgh and Kuala Lumpur are presented in Figure 4.61 and Figure 4.62 respectively. The comparison of cabin space temperatures with single and triple glazing in Edinburgh and Kuala Lumpur are presented in Figure 4.63 and Figure 4.64 accordingly.

In the case of solar irradiance in Edinburgh, the average solar irradiance on the EV fitted with single glazing windows is 1040.58 W. The average solar irradiance on the EV fitted with triple glazing windows is reduced to 717.03 W, which resulted in a 31.09 % reduction in solar irradiance. Although the magnitude of the solar irradiance is different, the both trend lines still exhibit similar curve. Upon simulation of the refrigeration circuit using this reduced solar thermal load, the power consumption for the case of triple glazing windows is 200 W, and down from 225 W as required by the vehicle with single glazing, therefore this has caused a 12.5 % reduction in power consumption. As seen in Figure 4.63, the cabin temperatures with triple glazed windows still display the same curve as the cabin temperatures with single glazed windows, although they differ in values. Both of the cabin temperatures starts at 15 °C, but the cabin temperature for the earlier case peaks at 31.23 °C, and the temperature for triple glazed windows peaks at 27.01 °C after an hour. It can be shown that the cabin temperature is reduced by 13.51 % if triple glazing windows are used on the EV.

In Kuala Lumpur, the average solar irradiance with single glazing windows is 2334.73 W, whereas the average solar irradiance with triple glazing windows is reduced to 1269.48 W. The use of triple glazing windows has caused a 45.64 %

reduction of solar irradiance transmitted into the cabin space. Although the solar irradiance transmitted into the cabin space has been reduced, the compressor power consumption is the same for both cases after simulation. This is due to the fact that the heat to be extracted is beyond the capacity of the refrigeration circuit for both cases of glazing, therefore the compressor is still working at its maximum capacity, thus the compressor power does not differ between both cases. Besides that, the peak cabin temperature for single glazed windows EV is 57.07 °C and the peak cabin temperature for triple glazing windows EV is 48.14 °C after an hour. The comparison between two peaks suggests that there is a 15.65 % reduction in cabin temperature after an hour if triple-glazing windows is used on a vehicle.

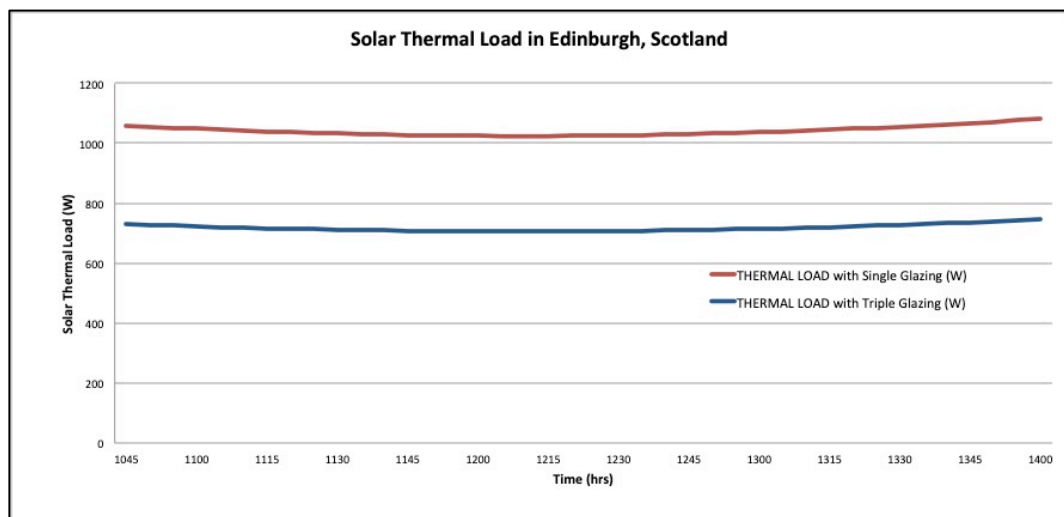


Figure 4.61: Comparison of Solar Thermal Load for Single and Triple Glazing Windows in Edinburgh

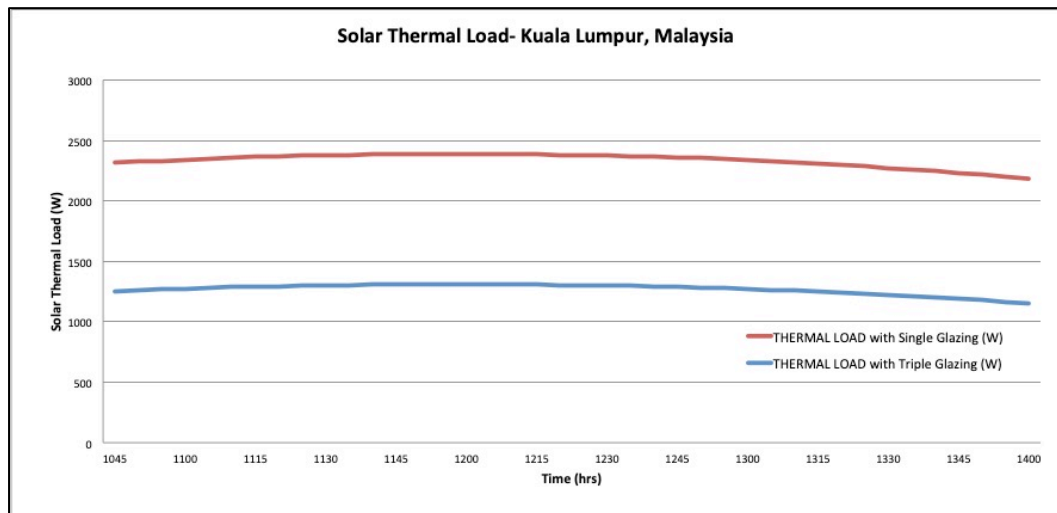


Figure 4.62: Comparison of Solar Thermal Load for Single and Triple Glazing Windows in Kuala Lumpur

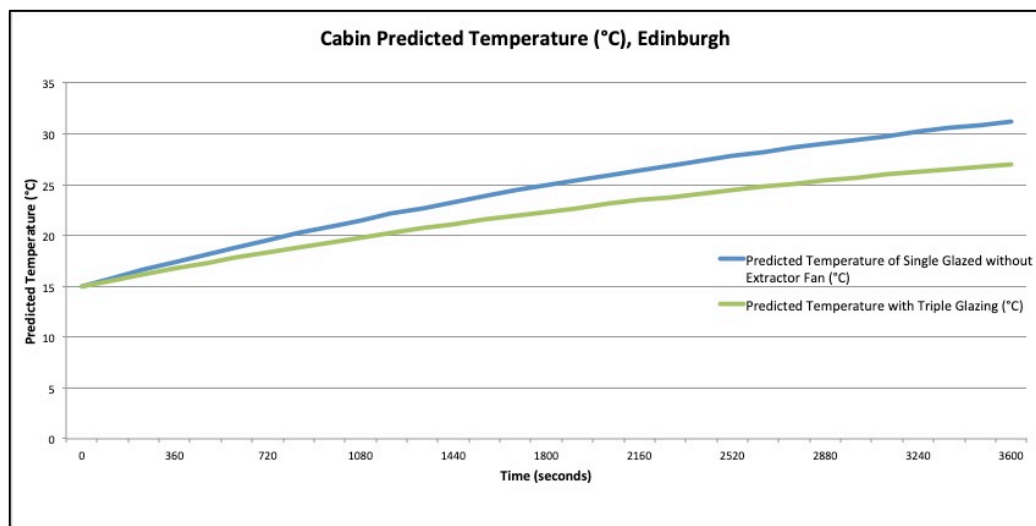


Figure 4.63: Comparison of Cabin Temperature of Single Glazed and Triple Glazed Windows in Edinburgh

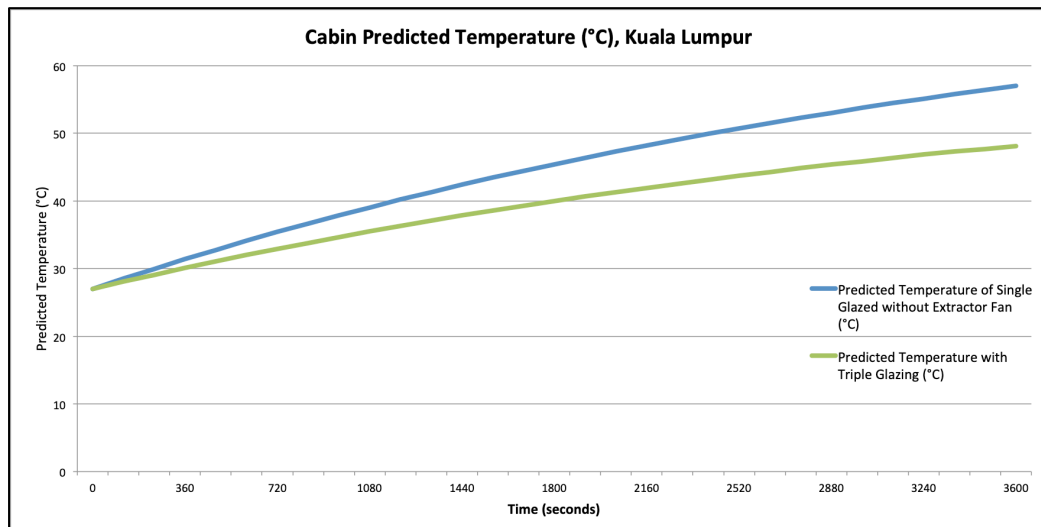


Figure 4.64: Comparison of Cabin Temperature of Single Glazed and Triple Glazed Windows in KL

4.7.2 Active Supporting Infrastructure on Cabin Cooling

The active supporting infrastructure in this case is the two 21 W extractor fan that imparts airflow in the cabin space in order to remove the hot air from the cabin space into the environment. This imposes a cooling load on the cabin space, thus reduces the cabin temperature accordingly. Upon simple calculation, where the initial and peak cabin temperature is 15 °C and 31.23 °C respectively, the cooling capacity of the extractor fans is 130.5 W for the case of Edinburgh. For the case of Kuala Lumpur, the cooling capacity of the fans is 274.3 W, when the initial and peak cabin temperature is 27 °C and 57.07 °C respectively. The different initial and peak cabin temperatures for both cases cause the cooling capacities to be different. The effect of changes in cabin temperature due to this cooling capacity is studied for both Edinburgh and Kuala Lumpur, as presented in Figure 4.65 and Figure 4.66 respectively.

As seen from Figure 4.65, for the case of Edinburgh, it can be implied that the trend of cabin temperature is the same for curve, thus the inclusion of extractor fan does not affect the temperature behaviour. However, the peak cabin temperature when the extractor fan is used decrease from 31.23 °C to 29.06 °C. Therefore, with the use of extractor fan system, the peak cabin temperature only manages to decrease by 6.95 % after an hour. This amount is relatively small as compared to the heat reduction due to triple glazing windows configuration. The cooling load of 130.5 W is added into the thermal load input for simulation, where the total thermal load input

reduces from 1880.14 W to 1749.64 W with only 6.94 % reduction in thermal load. Upon simulation of this result, it is found that the power consumption remains the same, even when the extractor fan is fitted.

According to Figure 4.66, for the case of Kuala Lumpur, it can be seen that the cabin temperature curves are similar to each other, with differing values between them. The peak cabin temperature without the fan system is 57.07 °C, and upon installation of the fan system, the cabin temperature only peaks at 52.49 °C after an hour. This causes a reduction of 8 % with the installation of the extractor fan system, which again is a relatively small value as compared to the triple glazing windows configuration. The cooling load of 273.4 W is added into the thermal load input for simulation, where the total thermal load input reduces from 3136.14 W to 2864.74 W with only 8.72 % reduction in thermal load. Upon simulation of this result, it is found that the power consumption remains the same, even when the extractor fan is fitted.

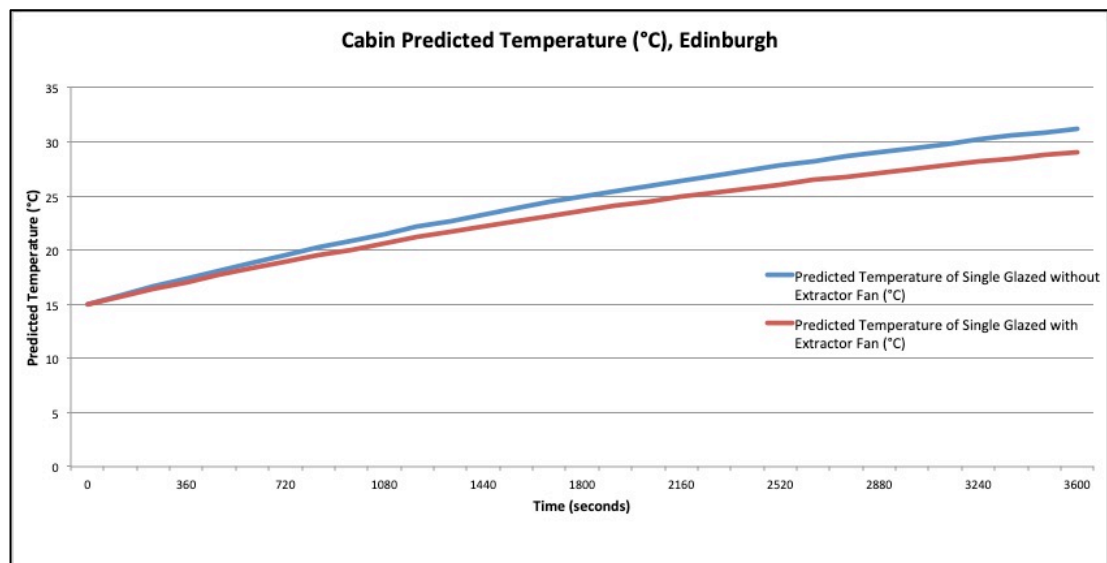


Figure 4.65: Cabin Temperature With and Without Extractor Fan, Edinburgh

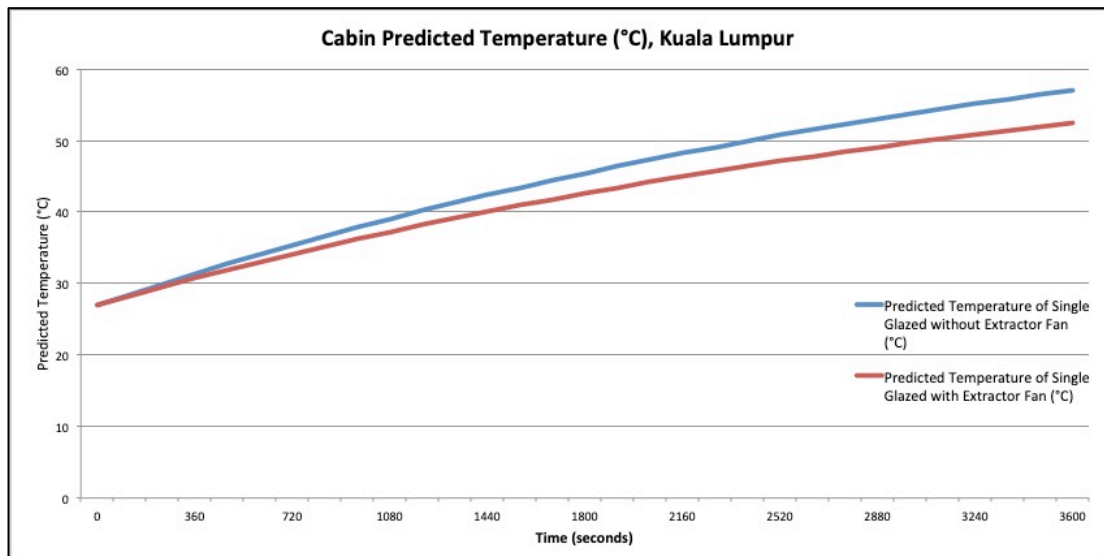


Figure 4.66: Cabin Temperature With and Without Extractor Fan, Kuala Lumpur

4.7.3 Combination of Passive and Active Supporting Infrastructure

A combination of passive and active supporting infrastructure can be included in the same EV in order to further optimise the cabin cooling. In this case, a combination of both triple glazing windows and the extractor fans system may be installed on the same EV. The effects of the cabin temperature changes can be studied for both Edinburgh and Kuala Lumpur cases as shown in Figure 4.67 and Figure 4.68 respectively.

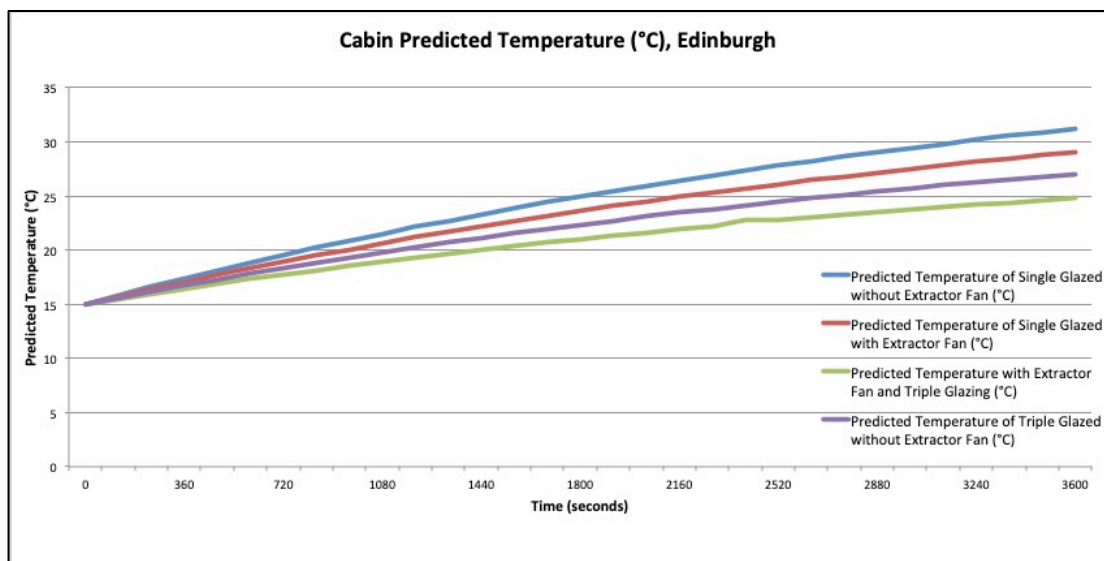


Figure 4.67: Cabin Temperatures for Combination of Infrastructures, Edinburgh

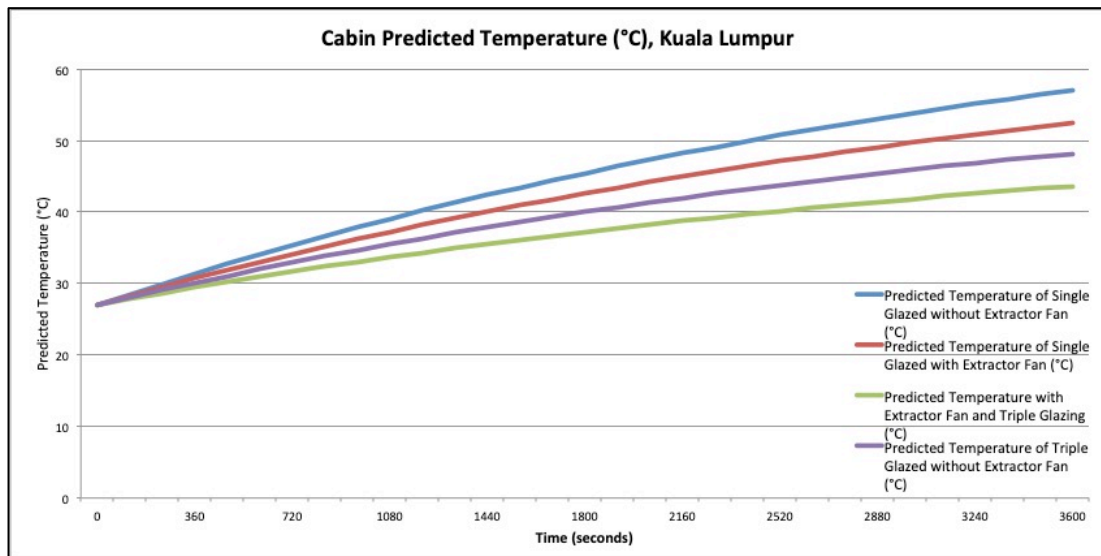


Figure 4.68: Cabin Temperatures for Combination of Infrastructures, Kuala Lumpur

As seen in Figure 4.67, for the combination of triple glazing windows and extractor fans configuration, the peak cabin temperature after one hour is 24.81 °C as compared to 31.32 °C with a single glazing windows and no extractor fans configuration. The cabin temperature has been successfully reduced by 20.5 % after an hour for the case of Edinburgh. The total cooling load of 454.05 W is added into the thermal load input for simulation, where the total thermal load input reduces from 1880.14 W to 1426.09 W with 24.1 % reduction in thermal load.

According to Figure 4.68, using the same combination of configuration, the peak cabin temperature after one hour is 43.64 °C, as opposed to 57.07 °C, which only has single glazing windows and no extractor fans, for the case of Kuala Lumpur. The cabin temperature has been successfully reduced by 23.55 % after an hour. The cooling load of 1338.65 W is added into the thermal load input for simulation, where the total thermal load input reduces from 3136.14 W to 1797.49 W with 42.68 % reduction in thermal load.

4.8 Summary

The Phase 1 thermal load models have been individually discussed, along with two samples of the combined thermal loads model. The validity of the thermal load model is verified by comparison with experimental results obtained by Aisling Doyle. The refrigeration circuit model in Phase 2 performed according to normal operating characteristics and within normal operating range, as well as limits. The results from

the thermal load models have been incorporated into the refrigeration circuit model, and its response is duly discussed and justified. Furthermore, the validity of the refrigeration model is confirmed, as a fairly accurate approximation is obtained after comparison with results from a physical refrigeration circuit. The refrigeration model is then expanded to three different driving cycles, in which it is able to respond to the thermal load involved as well as performed as expected. Additionally, the temperature-predicting model is shown to be able to predict the cabin temperature based on solar irradiance and ambient thermal load. Based on the three types of configuration of supporting infrastructure, namely single glazing without extractor fans, triple glazing without extractor fans, and triple glazing with extractor fans, it is found that the last configuration gives the most optimal control on the cabin cooling, where it is able to produce the greatest reduction in total thermal load, as well as peak cabin temperature after an hour of simulation.

CHAPTER 5

CONCLUSIONS AND RECOMMENDATIONS

5.1 Conclusions

The first objective of numerical modelling for the electric vehicle cabin cooling with consideration of external climate effect using MatLab® Simulink ® has been performed through the thermal load and refrigeration circuit modelling. The second objective of validating the numerical modelling by comparison with experimental data has been achieved through the comparison of the thermal load modelling with experimental data conducted by Aisling Doyle, and also through the comparison of refrigeration circuit model response to the response parameters from the physical G.U.N.T Hamburg ET 400 refrigeration circuit. The third objective of optimising the control of EV's cabin cooling is performed through the study of the supporting infrastructure and their effects on the cabin temperature, combined thermal load and power consumption. Lastly, with the satisfaction of all three objectives, the aim of this dissertation is achieved, where the numerical model for the EV's cabin cooling system is successfully developed.

5.1.1 Thermal Load Modelling

The human metabolic, ambient, ventilation, and battery thermal loads, as well as solar thermal load for Edinburgh and Kuala Lumpur are individually simulated before the combined thermal load is simulated.

Each driver and passenger contributes 163.7 W and 105.9 W respectively, with a maximum metabolic thermal load of 597.3 W for a Renault Zoe EV.

Every increment of 1 °C causes a 40.9 W increase in ambient thermal load, with a minimum value of -253.4 W and maximum of 769.4 W for a cabin with temperature of 23 °C, and ambient range from 15 °C to 40 °C.

Every increment of 1 °C causes a 18.29 W increase in ambient thermal load, with a minimum value of -137.2 W and maximum of 322.5 W for a cabin with temperature of 23 °C, and ambient range from 15 °C to 40 °C. It is worth noting that the negative polarity indicates heat flow from the cabin to ambient environment.

Each battery has 0.1 W penetrating into the cabin, thus for this EV, the maximum battery thermal load is 126 W for a total of 1260 cells.

For the solar thermal load in Edinburgh, Scotland, at 10:45 am to 12:05 pm, the heat declines at 2.19 W for every five minutes, and increases at 2.48 W per five minutes from 12:10 pm to 2 pm. The minimum and maximum solar thermal load is 1023 W at 12:10 pm and 1080 W at 2 pm. The average solar thermal load in this modelling is 1040.58 W, which compared to the experimental result of 971 W conducted by Aisling Doyle, produces an error of 7.17%.

For the solar thermal load in Kuala Lumpur, Malaysia at 10:45 am to 12 noon, the heat increases at 5.29 W for every five minutes, and declines at 8.87 W per five minutes from 12 noon to 2 pm. The minimum and maximum solar thermal load is 2184 W at 2 pm and 2388 W at 12:05 pm.

The sample combined thermal load in Edinburgh and Kuala Lumpur is 1880.14 W and 3136.14 W respectively, where the latter has 40.05 % more thermal heat than the former.

5.1.2 Refrigeration Circuit Modelling

The simulation of refrigeration circuit is conducted for individual thermal loads as mentioned in the previous section.

For the metabolic thermal load input, the compressor inlet and outlet pressures are 0.14 MPa and 0.65 MPa respectively, which gives a compressor pressure ratio of 4.5. The maximum heat extracted is at 600 W and the compressor draws a maximum power of 140 W. The maximum deviation of cabin temperature from the targeted temperature is 1.37 % at time of 4150 seconds.

For the ambient thermal load input, the compressor inlet and outlet pressures are 0.16 MPa and 0.95 MPa respectively, which gives a compressor pressure ratio of 6. The maximum heat extracted is at 650 W and the compressor draws a maximum power of 173 W. The maximum deviation of cabin temperature from the targeted temperature is 4.19 % at time of 3760 seconds.

For the ventilation thermal load input, the compressor inlet and outlet pressures are 0.16 MPa and 0.94 MPa respectively, which gives a compressor pressure ratio of 5.9. The maximum heat extracted is at 400 W and the compressor

draws a maximum power of 160 W. The maximum deviation of cabin temperature from the targeted temperature is 1.08 % at time of 2500 seconds.

For the battery thermal load input, the compressor inlet and outlet pressures are 0.16 MPa and 0.93 MPa respectively, which gives a compressor pressure ratio of 5.8. The maximum heat extracted is at 320 W and the compressor draws a maximum power of 163 W. The maximum deviation of cabin temperature from the targeted temperature is 0.85 % at time of 1230 seconds.

For the solar thermal load input for both locations, the compressor inlet and outlet pressures are 0.17 MPa and 0.8 MPa, which gives a compressor pressure ratio of 5. 1130 W and 2450 W of heat are extracted, where the compressor draws power of 260 W and 470 W for the case of Edinburgh and Kuala Lumpur respectively. The average deviation of cabin temperature from the targeted temperature is 2.11 % in Edinburgh and 1.85 % in the case of Kuala Lumpur.

5.1.3 Validation Experiment

A validation experiment is conducted through the comparison of simulated and physical refrigeration circuit parameter response, which includes compressor inlet and outlet temperatures, compressor inlet and outlet pressure, along with their pressure ratio, as well as the compressor power.

The compressor inlet temperature for simulated model is 7 °C and 5.71 °C for the physical refrigeration circuit, which has a relative error of 22 %.

The compressor outlet temperature for simulated model is 43 °C and 53.42 °C for the physical refrigeration circuit, which has a relative error of 19.5 %.

The compressor inlet pressure for simulated model is 3.65 bar and 3.29 bar for the physical refrigeration circuit, which has a relative error of 10.94 %.

The compressor outlet pressure for simulated model is 10.97 bar and 12 bar for the physical refrigeration circuit, which has a relative error of 13.58 %.

From the information of compressor inlet and outlet pressure, the compressor pressure ratio is found to be 2.84 for the simulated model and 3.65 for the physical refrigeration circuit. When calculated, this gives a relative error of 22.12 %.

The average compressor power drawn for simulated model is 140 W and 139.77 W for the physical refrigeration circuit, which has a relative error of 1.97 %.

5.1.4 Expansion Work on Different Driving Cycles

The refrigeration model is expanded to simulate the refrigeration circuit response to the battery heat generated through three different driving cycles.

In the UDDS driving cycle simulation, the maximum thermal load is 411.93 W at 9786 seconds. The compressor inlet pressure is floored at 0.15 MPa and the outlet pressure peaks at 0.68 MPa, thus giving a peak pressure ratio of 4.6. The maximum heat extracted is 340 W, which required a compressor power of 130 W. The maximum cabin temperature deviation from the targeted temperature is 1.09 % at 8460 seconds.

Besides that, in the HWFET driving cycle simulation, the maximum thermal load is 505.2 W at 4133 seconds. The compressor inlet pressure is floored at 0.15 MPa and the outlet pressure peaks at 0.68 MPa, thus giving a peak pressure ratio of 4.6. The maximum heat extracted is 350 W, which required a compressor power of 130 W. The maximum cabin temperature deviation from the targeted temperature is 0.81 % at 3590 seconds.

In the UDDS driving cycle simulation, the maximum thermal load is 1318.06 W at 2103 seconds. The compressor inlet pressure is floored at 0.15 MPa and the outlet pressure peaks at 0.72 MPa, thus giving a peak pressure ratio of 4.8. The maximum heat extracted is 440 W, which required a compressor power of 138 W. The maximum cabin temperature deviation from the targeted temperature is 1.4 % at 100 seconds.

5.1.5 Cabin Temperature-Predicting Model

For the application of cabin temperature predicting model in Edinburgh, the temperature is seen to have rise from 15 °C to 32.23 °C, which translates into a rise of 16.23 °C in 3600 seconds.

Furthermore, for the application of cabin temperature predicting model in Kuala Lumpur, the temperature is seen to have rise from 27 °C to 50.07 °C, which translates into a rise of 30.07 °C in 3600 seconds.

5.1.6 Supporting Infrastructure on Cabin Cooling

A passive and active supporting infrastructure has been studied, where their effects on the cabin temperature and power consumption will be summarised.

For the case of triple glazing windows in Edinburgh, the solar irradiance is calculated to be 717.03 W, which is a 31.09 % reduction from 1040.58 W for vehicles using only single glazing. Furthermore, the compressor power consumption has from by 12.5 % from 225 W to 200 W after the installation of triple glazing windows. The predicted cabin temperature after 3600 seconds has dropped by 13.51 % from 31.23 °C to 27.01 °C with the use of triple glazing windows.

For the case of triple glazing windows in Kuala Lumpur, the solar irradiance is calculated to be 1269.48 W, which is a 45.64 % reduction from 2334.73 W for vehicles using only single glazing. Furthermore, the compressor power consumption remains the same. The predicted cabin temperature after 3600 seconds has dropped by 15.65 % from 57.07 °C to 48.14 °C with the use of triple glazing windows.

For the case of using two 21 W extractor fans in Edinburgh, powered using solar cell installed on the roof and bonnet of the EV, the total combined thermal load is calculated to be 1749.64 W, which is 6.94 % reduction from 1880.14 W for the EV without the fans. Furthermore, the compressor power consumption remains the same. The predicted cabin temperature after 3600 seconds has dropped by 6.95 % from 31.23 °C to 29.06 °C with the use of the extractor fans configuration.

For the case of using two 21 W extractor fans in Kuala Lumpur, powered using solar cell installed on the roof and bonnet of the EV, the total combined thermal load is calculated to be 2864.74 W, which is 8.72 % reduction from 3136.14 W for the EV without the fans. Furthermore, the compressor power consumption remains the same. The predicted cabin temperature after 3600 seconds has dropped by 8 % from 57.07 °C to 52.49 °C with the use of the extractor fans configuration.

The most optimal configuration of supporting infrastructure for cabin cooling is the combined use of triple glazing windows and the extractor fans, where the total combined thermal load is calculated to be 1426.09 W, which is 24.1 % reduction from 1880.14 W for the EV without the fans and triple glazing, for the case of Edinburgh. The predicted cabin temperature after 3600 seconds has dropped by 20.5 % from 31.23 °C to 24.81 °C with the use of the extractor fans and triple glazing windows configuration

For the optimal configuration in Kuala Lumpur, the total combined thermal load is calculated to be 1797.49 W, which is 42.68 % reduction from 3136.14 W for the EV without the fans and triple glazing. The predicted cabin temperature after

3600 seconds has dropped by 23.55 % from 50.07 °C to 43.64 °C with the use of the extractor fans and triple glazing windows configuration

5.2 Recommendations

This project has its inherent scope, limitation and assumptions, which can be gradually expanded in the future through the removal of limitation and assumptions, as well as broadening of the scope in stages.

Improvements can be implemented on the thermal load model, especially in the solar thermal load model. This project uses a set of general formula for calculating solar geometry that can be applied globally, but sacrifices a small percentage of accuracy. Therefore, the accuracy for solar geometry can be further improved by using formula that are either specific to the Northern or Southern Hemisphere in future works. For a better accuracy of the slope irradiance modelling, the global horizontal irradiation should be measured using a pyrometer that is accurate for the specific time of observation, instead of relying on daily average global horizontal irradiation data archived and published by local meteorological station.

Considerations for the temperature drop at the condenser and evaporator should also be established in future work. Additionally, compressor inefficiencies and actual heat loss can be added into future models in order to achieve a modelling that can better match a physical refrigeration circuit. A more complete numerical modelling of an air conditioning system in an EV can be achieved through the construction and integration of cabin blower and radiator models in the current refrigeration circuit model. This provides a more holistic view and understanding of the energy consumption of the air conditioning system, especially in an EV where the blower and radiator derive their power from the battery.

Finally, improvements can also be incorporated into the method of validating the refrigeration circuit. The current method of validation is by comparing the modelled data with results from a refrigeration circuit test rig. However, it is recommended that an actual test vehicle should be used in order to provide a higher level of realism and accuracy to the real life vehicle air conditioning system.

REFERENCES

- Abdulsalam, O., Santoso, B. & Aries, D., 2015. Cooling Load Calculation and Thermal Modeling for Vehicle by MATLAB. *International Journal of Innovative Research in Science, Engineering and Technology* , 4(5), pp.3052-60.
- Alahmer, A. & Omar, M., 2013. Vehicular Cabins' Thermal Comfort Zones; Fanger and Berkley Modeling. *Vehicle Engineering*, 1(1), pp.19-32.
- Alduchov, O. & Eskridge, R., 1996. *Improved Magnus Form Approximation of Saturation Vapor Pressure*. Asheville: National Climatic Data Center.
- Alexandrov, A., Kudriavtsev, V. & Reggio, M., 2001. Analysis of flow patterns and heat transfer in generic passenger car mini-environment. In *9th Annual Conference of the CFD Society of Canada*. Kitchener, 2001. CFD Society of Canada.
- AL-Ajmi, N., 2015. Coefficient of Performance Enhancement of Refrigeration Cycles. *Int. Journal of Engineering Research and Applications* , 5(3), pp.117-25.
- Anderson, M., 2017. *For Earth Day, here's how Americans view environmental issues*. [Online] Available at: <http://www.pewresearch.org/fact-tank/2017/04/20/for-earth-day-heres-how-americans-view-environmental-issues/> [Accessed 11 June 2018].
- Arici, O. & Yang, S.-l., 1999. Computer Model for Automobile Climate Control System Simulation and Application. *International Journal of Applied Thermodynamics*, 2(2), pp.59-68.
- ASHRAE, 2009. *2009 ASHRAE Handbook Fundamentals*. Atlanta: ASHRAE.
- Bentriac, M., Alshatewi, M. & Hanafy, O., 2017. Developments of vapor-compression systems for vehicle air-conditioning: A review. *Advances in Mechanical Engineering* , 9(8), pp.1-15.
- BP, 2016. *BP*. [Online] Available at: bp.com/statisticalreview [Accessed 11 June 2018].
- Breque, F. & Nemer, M., 2017. Cabin Thermal Needs: Modeling and Assumption Analysis. In *12th International Modelica Conference*. Prague, 2017. International Modelica.
- Brogliola, L., Autefage, G. & Ponchant, M., 2012. Impact of passenger thermal comfort and electric devices temperature on range: a system simulation approach. *World Electric Vehicle Journal* , 5, pp.1082-89.
- Cengel, Y. & Boles, M., 2015. *Thermodynamics: An Engineering Approach*. 5th ed. New York: McGraw-Hill Education.

da Cunha, I., 2010. *Refrigeration Systems Energy Efficiency Reference Guide*. Montreal: CEATI International.

Doyle, A., 2017. *The development of numerical temperature algorithm to predict infor temperature of an electric vehicle cabin's space*. Edinburgh: Edinburgh Napier University Edinburgh Napier University.

Ekici, C., 2013. A review of thermal comfort and method of using Franger's PMV equations. In *5th International Symposium on Measurement, Analysis and Modeling of Human Functions*. Vancouver, 2013. IMEKO.

EPA, 2018. *Source of greenhouse gas emission*. [Online] Available at: <https://www.epa.gov/ghgemissions/sources-greenhouse-gas-emissions> [Accessed 11 June 2018].

Evtimov, I., Ivanov, R. & Sapundjiev, M., 2017. Energy consumption of auxiliary systems of electric cars. In *MATEC Web of Conferences.*, 2017.

Farrington, R., Cuddy, M., Keyser, M. & Rugh, J., 1999. Opportunities to Reduce Air-Conditioning Loads Through Lower Cabin Soak Temperatures. In *16th Electric Vehicle Symposium*. Beijing, 1999. NREL.

Farzaneh, Y. & Tootoonchi, A., 2008. Controlling automobile thermal comfort using optimized fuzzy controller. *Applied Thermal Engineering* , 28, pp.1906-1917.

Fayazbakhsh, M. & Bahrami, M., 2013. *Comprehensive Modeling of Vehicle Air Conditioning Loads Using Heat Balance Method*. Pennsylvania: SAE International.

Fletcher, B. & Saunders, C.J., 1994. Air change rates in stationary and moving motor vehicles. *Journal of Hazardous Materials* , 38, pp.243-256.

Fryar, C.D., Gu, Q., Ogden, C. & Flegal, K.M., 2016. *Anthropometric reference data for children and adults: United States, 2011–2014.*. Hyattsville: National Center for Health Statistics.

Hensen, J., 1990. Literature Review on Thermal Comfort in Transient Conditions. *Building and Environment*, 25(4), pp.309-316.

History.com, 2010. *Model T*. [Online] Available at: <http://www.history.com/topics/model-t> [Accessed 11 June 2018].

Iman, M., Basha, M., Azizzudin, M. & Reddy, K., 2013. Design of air conditioning systems in automobile. *International Journal of Innovative Research in Science, Engineering and Technology* , 2(12), pp.7460-64.

Ingersoll, J., Kalman, T., Maxwell, L. & Niemiec, R., 1993. Automobile Passenger Compartment Thermal Comfort Model- Part II; Human Thermal Comfort Calculation. *SAE Technical Paper*.

ISO, 2004. *Ergonomics of The Thermal Environment- Determination of Metabolic Heat Production*. ISO Standard.

Janotkova, E. & Pavelek, M., 1994. *New Trends in the Field of Automobile Air Conditioning*. Brno: Brno University of Technology.

JPJ, 2015. *Kementerian Pengangkutan Malaysia*. [Online] Available at: <http://www.mot.gov.my/my/Statistik%20Tahunan%20Pengangkutan/Statistik%20Pengangkutan%20Malaysia%202015.pdf> [Accessed 11 June 2018].

Kamar, H., Senawi, M. & Kamsah, N., 2012. Computerized Simulation of Automotive Air-Conditioning System: Development of Mathematical Model and Its Validation. *International Journal of Computer Science* , 9(2), pp.23-34.

Khayyam, H., Kouzani, A. & Hu, E., 2009. Reducing Energy Consumption of Vehicle Air Conditioning System by an Energy Management System. In *2009 IEEE Intelligent Vehicles Symposium*. Xi'an, 2009. IEEE.

Kiss, T. & Chaney, L., 2013. A New Automotive Air Conditioning System Simulation Tool Developed in MATLAB/Simulink. *International Journal of Passenger Car Mechanical System*, 6(2).

Kondo, T., Suetake, H., Katayama, A. & Morishita, M., 2011. Development of Automotive Air-Conditioning Systems by Heat Pump Technology. *Mitsubishi Heavy Industries Technical Review* , 48(2), pp.27-32.

Li, W. et al., 2016. Determining the main factors influencing the energy consumption of electric vehicles in the usage phase. In *23rd CIRP Conference on Life Cycle Engineerin.*, 2016. Elsevier B.V.

Lin, P.-H., 2010. Performance evaluation and analysis of EV air-conditioning system. *World Electric Vehicle Journal* , 4, pp.197-201.

Mebarki, B., Draoui, B. & Rahmani, L., 2013. *Impact of the Air-Conditioning System on the Power Consumption of an Electric Vehicle Powered by Lithium-Ion Battery*. Hindawi Publishing.

Monteith, J. & Unsworth, M., 2013. *Principles of Environmental Physics Plants, Animals, and the Atmosphere*. Oxford: Elsevier Ltd.

Musat, R. & Helerea, E., 2009. *Parameters and Models of the Vehicle Thermal Comfort*. Braşov : University of Braşov.

NEA, 2018. *Singapore's Climate Information & Data*. [Online] Available at: <https://www.nea.gov.sg/weather/overview/singapore's-climate-information-data> [Accessed 20 June 2018].

Neacsu, C., Tabacu, I., Ivanescu, M. & Vieru, I., 2017. The evaluation of the overall thermal comfort inside a vehicle. In *IOP Conference*. Bristol, 2017. IOP Publishing.

Paya, J., Corberan, J.M., Torregrossa-Jaime, B. & Vasile-Muller, C., 2014. *Innovative air-conditioning systems for conventional and electric vehicles S*. Valencia: Universidad Politécnic de Valencia.

Pedersen, C., Fisher, D. & Liesen, R., 1997. Development of a Heat Balance Procedure for Calculating Cooling Loads. *ASHRAE Transactions*, 103(2), pp.459-68.

Phan, M.T., 2017. *Weather and extreme heat in association with mental disorders The case of Hanoi, Vietnam*. UMEÅ: Umea University.

Ritchie, H., 2017. *Our world in data*. [Online] Available at: <https://ourworldindata.org/how-long-before-we-run-out-of-fossil-fuels> [Accessed 11 June 2018].

Simion, M., Socaciu, L. & Unguresan, P., 2015. Factors which influence the thermal comfort inside of vehicles. In *Sustainable Solutions for Energy and Environment*. Bucharest, 2015. EENVIRO.

Song, B., Kwon, J. & Kim, Y., 2015. Air Conditioning System Sizing for Pure Electric Vehicle. *World Electric Vehicle Journal*, 7, pp.407-13.

Singh, A.K., Singh, H., Singh, A.P. & Sawhney, R.L., 2002. Numerical Calculation of Psychrometric Properties on a Calculator. *Building and Environment*, 37(4), pp.415-419.

Spitler, J., 2014. *Load Calculation Applications Manual*. Atlanta: ASHRAE.

Vinofer, D. & Rajakumar, S., 2016. Cooling load calculation and design of air-conditioning systems in automobile. *International Journal of Research in Social Sciences And Humanities*, 6(1), pp.94-103.

WeatherOnline, 2018. *Edinburgh Airport*. [Online] Available at: <https://www.weatheronline.co.uk/weather/maps/city?WMO=03160&CONT=ukuk&LAND=UK&ART=RLF&LEVEL=150> [Accessed July 30 2018].

Xia, Y. et al., 2016. *HVAC system for electric vehicle with driving range extension*. Washington D.C: USPTO USPTO.

Zheng, Y., Mark, B. & Youmans, H., 2011. *A Simple Method to Calculate Vehicle Heat Load*. Pennsylvania: SAE International.

APPENDICES

Appendix 1: Expansion of Ventilation Thermal Load Model Subsystems

